Feshbach Resonances in ^{40}K

Antje Ludewig

Feshbach Resonances in ^{40}K

Academisch Proefschrift

ter verkrijging van de graad van doctor
aan de Universiteit van Amsterdam
op gezag van de Rector Magnificus prof. dr. D.C. van den Boom
ten overstaan van een door het college voor promoties ingestelde
commissie, in het openbaar te verdedigen in de Agnietenkapel
op vrijdag 16 maart 2012, te 12:00 uur

door

Antje Ludewig

geboren te Reutlingen, Duitsland

Promotiecommissie:

Promotor:	prof. dr. J.T.M. Walraven
Overige leden:	prof. dr. M.S. Golden dr. T.W. Hijmans dr. ir. S.J.J.M.F. Kokkelmans prof. dr. H.B. van Linden van den Heuvell prof. dr. G.V. Shlyapnikov prof. dr. C. Zimmermann

Faculteit der Natuurwetenschappen, Wiskunde en Informatica (FNWI)

ISBN: 978-94-6191-188-9

Cover showing loss features around Feshbach resonances in the $d + e$ mixture in the clouds above Noetzie beach, photo by the author, design and implementation by Bodo Ludewig.

The work described in this thesis was carried out in the group "Quantum Gases and Quantum Information" at the Van der Waals–Zeeman Institute of the University of Amsterdam, Science Park 904, 1098 XH Amsterdam, The Netherlands. A limited number of hard copies of this thesis is available there.
A digital version of this thesis including the hyperlinks to the cited articles can be downloaded from
http://www.science.uva.nl/~walraven or http://dare.uva.nl .
This work is part of the research programme of the Foundation for Fundamental Research on Matter (FOM), which is part of the Netherlands Organisation for Scientific Research (NWO).

Contents

1 Introduction **1**
- 1.1 Cold quantum gases . . . 2
- 1.2 This thesis . . . 3
- 1.3 Outline . . . 3

2 Theoretical Background **5**
- 2.1 Fermions . . . 5
- 2.2 Two-body Hamiltonian . . . 6
  - 2.2.1 Internal Hamiltonian . . . 7
  - 2.2.2 Hamiltonian for the relative motion . . . 8
- 2.3 Elastic collisions . . . 9
- 2.4 Spin Exchange and ^{40}K . . . 10
  - 2.4.1 Populated states in the magnetic trap . . . 13
  - 2.4.2 Scattering rate for spin exchange . . . 13
- 2.5 Feshbach resonances . . . 14
- 2.6 Asymptotic bound state model . . . 16
- 2.7 Trapped fermions . . . 17
  - 2.7.1 Fermi degenerate density distribution . . . 18

3 Experimental setup **21**
- 3.1 Introduction . . . 21
- 3.2 Vacuum system . . . 22
- 3.3 Laser system . . . 25
- 3.4 Magneto-optical trapping . . . 28
  - 3.4.1 Two-dimensional MOT for ^{40}K . . . 28
  - 3.4.2 Three-dimensional MOT . . . 30
- 3.5 Optically plugged magnetic trap . . . 31
  - 3.5.1 Magnetic trap . . . 32
  - 3.5.2 Optical plug . . . 34
- 3.6 Optical dipole trap . . . 35
  - 3.6.1 Intensity stabilization of the fibre laser . . . 36
- 3.7 Feshbach coils . . . 38
- 3.8 Imaging systems . . . 41
  - 3.8.1 Cameras and optical setup . . . 41
  - 3.8.2 Fluorescence imaging . . . 43
  - 3.8.3 Absorption imaging . . . 43

3.8.4 High-field imaging . . . 44
3.9 Computer control and analysis . . . 47
3.9.1 Control program and hardware . . . 47
3.9.2 Software . . . 48
3.10 Sources for radio and microwave frequency . . . 48
3.10.1 DDS systems . . . 49
3.10.2 Amplification and switching . . . 49

4 EXPERIMENTAL SEQUENCE **51**
4.1 Atom cooling and trapping . . . 53
4.2 State preparation . . . 55
4.2.1 State cleaning . . . 56
4.2.2 State transfers . . . 57
4.3 Field-dependent loss measurements . . . 58
4.4 Stern-Gerlach imaging . . . 59
4.5 Magnetic field calibration . . . 59
4.6 Measured Feshbach resonances . . . 62
4.6.1 p-wave resonances with special features . . . 63
4.6.2 Width of a Feshbach resonance . . . 64

5 FESHBACH RESONANCES IN ^{40}K **69**
5.1 Introduction . . . 69
5.2 Experiments . . . 71
5.2.1 Experiments in Amsterdam . . . 73
5.2.2 Experiments in Munich . . . 75
5.2.3 Experiments in Zurich . . . 75
5.3 Theoretical models . . . 78
5.3.1 Coupled channels calculations . . . 78
5.3.2 Multichannel quantum defect theory . . . 83
5.3.3 Asymptotic bound state model . . . 83
5.3.4 Comparison of MQDT and ABM . . . 85
5.4 Summary and conclusions . . . 87

A ATOMS IN OPTICAL POTENTIALS **89**
A.1 Optical potential for ^{40}K . . . 89
A.2 Rotating wave approximation . . . 90
A.3 Potential produced by a Gaussian beam . . . 91
A.4 Density distribution . . . 92
A.4.1 Density in a harmonic potential . . . 92
A.4.2 Density in a Gaussian potential . . . 92

B HYPERFINE STRUCTURE **93**
B.1 Hyperfine splitting with an external magnetic field . . . 94
B.2 Limit of high and low magnetic fields . . . 95
B.3 Magnetic trapping potential . . . 96

C OPTICAL TRANSITION PROBABILITIES **99**
C.1 Transition probabilities at zero magnetic field . . . 99

C.2 Transition probabilities at non-zero magnetic field 100

Bibliography **105**

Summary **119**

Samenvatting **121**

Acknowledgements **123**

List of publications **127**

Chapter 1

Introduction

Everyday we encounter the results of discoveries and achievements of quantum mechanics and atomic physics which were made over the last century: be it the laser diode in a DVD player displaying our holiday pictures or measurements of the thickness of the Earth's ozone layer protecting us from UV radiation [Ste11]. In the first experiments in atomic physics the structure of atoms and their unique absorption spectra were deciphered, this is now the basis for thousands of applications from determining the velocity at which the universe expands to measuring the alcohol content in the breath of a speeding driver.

Nowadays, using light and electro-magnetic fields, atoms can be manipulated and cooled to temperatures within a few 100 nK of absolute zero. At such low temperature the behaviour of the atoms is not determined by their external degrees of freedom, but by quantum statistics. Bosons, particles with integer spin, can condense into a single state and form a macroscopic wavefunction extending over the inter-particle distance. More than 70 years after the initial description by Bose and Einstein [Bos24, Ein25], these Bose-Einstein condensates (BEC) were demonstrated in atomic gases [And95, Dav95a] and recently light, the most prominent member in the class of bosons, was condensed [Kla10].

For particles with half-integer spin, fermions, the behaviour at low temperatures is very different from bosons: instead of lumping together they each occupy a state by themselves, keeping their distance. The first degenerate quantum gas of fermionic atoms was produced in ^{40}K [DeM99a]. The quantum statistics of fermions [Fer24, Fer26, Dir26] plays an important role in many areas of physics. In condensed matter Fermi statistics determines electric and transport properties, neutron stars are prevented from collapsing by Fermi pressure and all matter known to us is composed of quarks and electrons which are fermionic elementary particles. For the understanding of superconductivity the pairing of fermions with attractive interactions plays a major role [Che05]. Finding accurate theoretical descriptions for these phenomena and understanding the influence of interactions and the quantum statistics of fermions is still ongoing work.

1.1 Cold quantum gases

In cold quantum gases formed by neutral atoms there are no effects of electric charge and crystal impurities and these systems enable us to observe the quantum nature of particles. Quantum degenerate gases have been used to demonstrate effects known from condensed matter physics, such as the Mott insulator - superfluid transition [Gre02, Jör08], the pairing of fermions [Reg04, Zwi05] and Anderson localization [Bil08, Roa08]. A step further is to use systems of cold atoms as a simulator for other systems in physics which are difficult or impossible to compute classically [Fey82]. This requires the implementation of controllable logic operations and a correlation of the atoms.

Strong correlations in experiments with cold quantum gases can be created either by confining the atoms tightly in optical lattices [Deu98, Gre02] or by tuning the interaction between the atoms in strength and even sign with the help of so-called Feshbach resonances [Fes58, Fes62, Chi10]. In cold atoms Feshbach resonances occur when a bound state within a two-body potential is resonant with the energy of a pair of unbound atoms. When the magnetic moments of the bound state and the unbound pair differs, they can be brought into resonance by applying a magnetic field. At the resonance, the scattering length, a measure for the interaction strength between atoms, diverges and changes sign.

The beauty and importance of Feshbach resonances is that they make it possible to use ultracold atoms as a model system for other areas of physics. Once the interaction between the atoms is strong enough, only a few universal parameters are required to describe the system. Systems with entirely different underlying processes can then be studied and compared to the strongly interacting cold atoms. At strong interactions the description of the cold atoms by mean-field theory breaks down and new methods need to be used. With the bosonic isotope of ^{39}K it has been shown recently that depending on the interaction strength the critical temperature for Bose-Einstein condensation changes [Smi11].

For certain interaction strengths atoms can also form few-body bound states [Kra06] with universal properties described by Efimov [Efi70]. Although these states exist due to two-body interaction, they are not present as two-body states. Efimov states are also relevant in nuclear physics [Ham10].

With a Feshbach resonance the interaction in fermionic quantum gas can be tuned from repulsive to attractive through the so-called BEC-BCS crossover. A bosonic molecule formed by two fermions can then transform into a pair of fermions coupled in momentum space, similar to a Cooper pair in superconducting theory [Gio08, Ing07, Blo08]. With ^{40}K this crossover has been explored [Ste08] and the condensation of the composite bosonic molecules into a BEC has been achieved [Gre03].

The positions and widths of Feshbach resonances of an atomic species in a specific state depend on the interatomic potential, which differs for the different species and the different states. Before Feshbach resonances can be used as a tool to tune the interaction, their positions and properties need to be determined. The atomic species we are working with is ^{40}K. It has been used as a single species [DeM99a, Lof02, Gre03] and others, but also in combination with the fermionic ^{6}Li [Wil08, Tie10b, Nai11, Wu11], and the bosonic ^{87}Rb [Sim03, Ino04, Fer06, Osp06a, Zir08a].

1.2 This thesis

Feshbach resonances occur in a multitude, especially with a element like ^{40}K, where many combinations of hyperfine states are stable. Prior to the results presented in this thesis the position of four Feshbach resonances in mixtures of ^{40}K in the three lowest hyperfine states was determined [Lof02, Reg03a, Reg03c, Reg06, Gae07]. In this thesis we present measurements on mixtures occupying states in the middle of the hyperfine manifold of ^{40}K.

Relying on experiment alone, one can get lost in the large number of loss features as if wandering in the wilderness bearing neither map nor compass. To find ones way in the uncharted area of Feshbach resonances it is necessary to start mapping out the surroundings by starting at a known situation and not just wander off randomly into the terrain. All explorations in experiments have to go hand in hand with the theoretical description of the position and nature of the resonance features.

With detailed knowledge of the interatomic potentials, the positions and properties of Feshbach resonances can be calculated using the coupled channel method (CC). However, this method is computationally intensive and whether all resonances are found depends on the step size in the numerical calculation. To predict the positions of new Feshbach resonances in previously unstudied state mixtures and to locate resonances of special interest we use a simple asymptotic bound state model (ABM). Once experimental data is obtained the initial parameters of the ABM are improved and more precise predictions are calculated. The experimental data obtained is compared with another approximate model, the multi quantum defect theory (MQDT), and the CC calculations.

To reach temperatures cold enough to study the quantum nature and control the interaction of the atoms, we use the techniques of laser cooling and evaporative cooling [Met99, Ket99]. We constructed an apparatus to cool and capture ^{40}K and measure Feshbach resonances at a stable magnetic field. To investigate a Feshbach resonance in a certain channel it is of great importance to prepare the hyperfine state mixtures required in a reliable and reproducible manner, especially in the case of ^{40}K with its rich hyperfine structure. Without this, difficulties arise when assigning experimentally observed loss features. To achieve this we developed a state-dependent detection scheme and a transfer procedure to populate the desired states. For the mapping out of Feshbach resonances we start out with binary mixtures of hyperfine states and measure atom loss depending on the magnetic field. In a second step, the states can be measured individually to rule out p-wave resonances within one hyperfine state.

1.3 Outline

This thesis covers both experimental and theoretical aspects of the study of Feshbach resonances in ^{40}K. **Chapter 2** contains a brief overview of the theoretical concepts required to describe cold trapped fermions. The scattering of cold fermions and the theory of Feshbach resonances are introduced. Here we put emphasis on the specifics of ^{40}K, which offers more options for stable state mixtures than other alkalis. Additionally the simple model which we use to calculate the positions of Feshbach resonances is presented.

The major part of this thesis was to construct an apparatus to produce cold mixtures of ^{6}Li and ^{40}K. In **Chapter 3** this experimental apparatus is described, putting the emphasis on the ^{40}K part and newly added components. Special features of our apparatus include the two-dimensional magneto-optical traps used as sources for the cold atoms, an optically plugged magnetic trap and a transport of the cold atom cloud by means of optical tweezers.

The detailed experimental sequence to produce cold mixtures of specific states in ^{40}K is explained in **Chapter 4**. The calibration of the magnetic field is of importance for the accurate specification of the measured data. How and to what precision we determine the magnetic field is also presented in Chapter 4. In this chapter we also present measurements of Feshbach resonances which show special features. An indication of the width of a Feshbach resonance is determined by evaporating the cold atom cloud at different magnetic fields; in Chapter 4 a model to fit the data is developed.

The main result of this thesis, the measurement of Feshbach resonances in various spin mixtures of ^{40}K, is presented in **Chapter 5**. The measured values are compared with values obtained by our collaborators in coupled channel calculations and the two simple models. Overall we measured the position of 23 Feshbach resonances in eleven different state combinations.

The appendices cover more details about ^{40}K in optical potentials (**Appendix A**), the hyperfine structure of ^{40}K (**Appendix B**) and its optical transition probabilities (**Appendix C**).

Chapter 2

Theoretical Background

In this chapter the theoretical concepts and notations used in this thesis are presented. This chapter gives an overview of scattering theory and Feshbach resonances and their description. We present the simplified model which was used to calculate the positions of Feshbach resonances in ^{40}K. This chapter also presents the assumptions to analyse and model the behaviour of ultracold atoms in external potentials. We put emphasis on the peculiarities of ^{40}K and the nature of fermions.

Cold quantum gases have a density which is in general low enough to describe the interactions as two-body interactions. For low enough temperatures the description of scattering processes by s-wave interaction is sufficient. The field of cold atoms is very active and there are plenty of good textbooks and overview articles dealing with both the theoretical aspects and the experimental techniques involved, for example [Ing07, Met99, Ket99, Chi05].

2.1 Fermions

In the everyday world as we experience it, two identical particles are never truly indistinguishable. For example the movement and the trajectory of two billiard balls which look alike can be followed and backtracked either by eye or with the help of a fast camera. Additionally two otherwise identical billiard balls can be marked with different numbers and made distinguishable.

In quantum mechanics however, identical particles are truly indistinguishable. The particles can be specified by nothing more than a complete set of commuting observables. According to the Heisenberg uncertainty principle it is not possible to obtain an exact measurement of all the observables simultaneously. The particles cannot be labelled and followed individually as in classical mechanics. When measuring a two-particle system of indistinguishable particles in state $|k_a\rangle$ and state $|k_b\rangle$, where the $|k_i\rangle$ represent a collective index for the complete set of observables, all linear combinations of the two particles of the form

$$c_1 |k_a\rangle |k_b\rangle + c_2 |k_b\rangle |k_a\rangle$$

result in identical eigenvalues. The eigenvalues are degenerate with respect to the exchange of the two particles $|k_a\rangle$ and $|k_b\rangle$, so at this level of analysis the linear com-

bination to describe the pair is not uniquely defined yet. This exchange degeneracy is lifted by including the exchange of two particles with the permutation operator P_{12} with

$$P_{12} \left|k_a\right\rangle \left|k_b\right\rangle = \left|k_b\right\rangle \left|k_a\right\rangle .$$

Its eigenvalues are +1 and -1, so the description of a two-body system is either symmetric or antisymmetric. It can be shown that in three dimensions the operator P_{12} is a constant of motion, as it commutes with the Hamiltonian [Sak94]. Being a constant of motion also implies that the symmetric and the antisymmetric solutions cannot be converted into each other. Those two distinct solutions represent two distinct kinds of particles: bosons and fermions. Including the exchange of two particles, the non-degenerate solutions for the two-body wavefunction for two indistinguishable particles a and b at positions $\mathbf{r}_1$ and $\mathbf{r}_2$ in terms of the single-particle wavefunctions $\psi_i(\mathbf{r}_i)$ are:

$$\begin{aligned} \psi_+(\mathbf{r}_1, \mathbf{r}_2) &= C_N \left(\psi_a(\mathbf{r}_1)\psi_b(\mathbf{r}_2) + \psi_b(\mathbf{r}_1)\psi_a(\mathbf{r}_2)\right) \\ \psi_-(\mathbf{r}_1, \mathbf{r}_2) &= C_N \left(\psi_a(\mathbf{r}_1)\psi_b(\mathbf{r}_2) - \psi_b(\mathbf{r}_1)\psi_a(\mathbf{r}_2)\right), \end{aligned} \tag{2.1}$$

with a normalizing factor C_N. Under exchange of the two particles the wavefunction is symmetric for the plus-sign and antisymmetric for the minus-sign. The symmetric wavefunction is applicable for bosons and the antisymmetric version describes fermions. From Eq. 2.1 the Pauli exclusion principle [Pau25] becomes clear: two identical fermions can neither occupy the same state ψ_i nor the same position $\mathbf{r}$. For $\psi_a = \psi_b$ the two-body wavefunction $\psi_-(\mathbf{r}_1, \mathbf{r}_2)$ vanishes, the same happens for $\mathbf{r}_1 = \mathbf{r}_2$. Particles with a half-integer spin, the fermions, obey Fermi-Dirac statistics [Dir26, Fer26], whereas particles with integer spin, the bosons, obey Bose-Einstein statistics [Bos24, Ein25]. For an ensemble of particles, the average number of particles $\bar{n}_i$ per single particle state ϵ_i is given by

$$\bar{n}_i^{\mathrm{BE}} = \frac{1}{e^{(\epsilon_i - \mu)/k_{\mathrm{B}}T} - 1} \tag{2.2}$$

for bosons and

$$\bar{n}_i^{\mathrm{FD}} = \frac{1}{e^{(\epsilon_i - \mu)/k_{\mathrm{B}}T} + 1} \tag{2.3}$$

for fermions. Here μ is the chemical potential. The behaviour of fermions and bosons differs most strikingly at low temperatures. Bosons in a trapping potential as depicted in Fig. 2.1 collect in the ground state of the system and form a Bose-Einstein condensate (BEC), as has been demonstrated for the first time in 1995 by [And95, Dav95a]. Identical fermions on the other hand, fill up the states up to the Fermi-energy E_F with one fermion occupying one state at a time. A Fermi degenerate gas of atoms has been realized for the first time in ^{40}K in 1999 [DeM99a].

2.2 Two-body Hamiltonian

At the densities and temperatures relevant for experiments with ultracold atoms, most of the interactions can be characterized by two-body interactions. Two interacting atoms can be described by the two-body Hamiltonian as:

$$\mathbf{H} = \mathbf{H}_{\mathrm{rel}} + \mathbf{H}_{\mathrm{int}}, \tag{2.4}$$

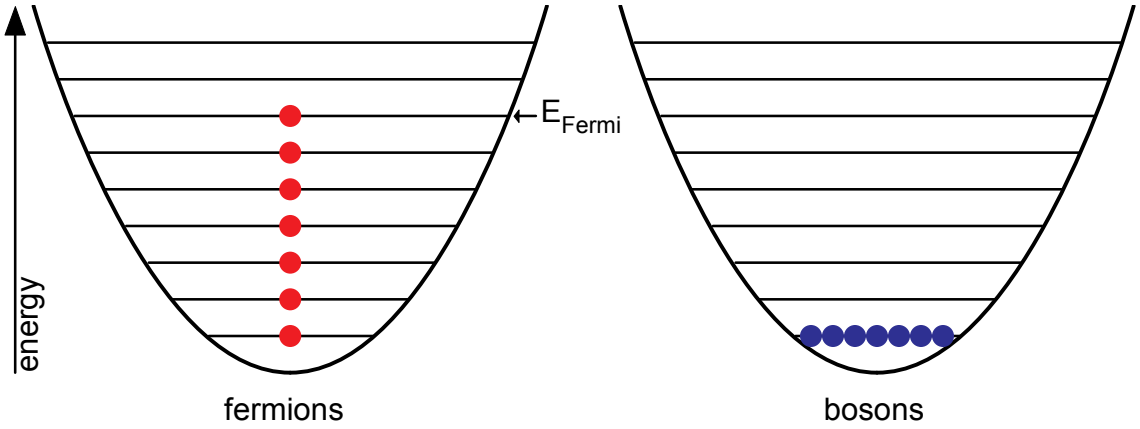

Figure 2.1: The behaviour of trapped fermions and bosons at zero temperature. Identical fermions fill the levels one by one up to the Fermi energy E_F, whereas bosons collect in the ground state to form a Bose-Einstein condensate.

with the Hamiltonian for the relative motion $\mathbf{H}_{\text{rel}}$ of the two atoms and the Hamiltonian describing the internal energy of the two atoms $\mathbf{H}_{\text{int}}$:

$$\mathbf{H}_{\text{rel}} = \frac{\mathbf{p}^2}{2m_{\text{r}}} + \mathbf{V}, \tag{2.5}$$

$$\mathbf{H}_{\text{int}} = \mathbf{H}^B_{\text{hf},\alpha} + \mathbf{H}^B_{\text{hf},\beta} \tag{2.6}$$

The operator $\mathbf{p}^2/2m_{\text{r}}$ describes the relative kinetic energy of two atoms with reduced mass $m_{\text{r}} = m_1 m_2/(m_1+m_2)$ and the potential $\mathbf{V}$ the effective interaction of the atoms. The internal Hamiltonian is presented in the following section.

2.2.1 Internal Hamiltonian

The internal Hamiltonian for two alkali atoms in their electronic ground state is the sum of hyperfine interaction $\mathbf{H}_{\text{hf}}$ and the Zeeman interaction $\mathbf{H}_{\text{Z}}$ for each of the two atoms[†] labelled α and β:

$$\mathbf{H}^B_{\text{hf}} = \mathbf{H}_{\text{hf}} + \mathbf{H}_{\text{Z}} \tag{2.7}$$

$$= \frac{a_{\text{hf}}}{\hbar^2}\mathbf{i}\cdot\mathbf{j} + \frac{\mu_{\text{B}}}{\hbar}(g_J\mathbf{j} + g_I\mathbf{i})\cdot\mathbf{B}, \tag{2.8}$$

where a_{hf} is the hyperfine constant for the fine structure level under consideration, g_J the total Landé g-factor of the electron, g_I the gyromagnetic factor of the nucleus, μ_{B} the Bohr magneton, $\hbar$ the reduced Planck constant $h/2\pi$ and $\mathbf{B}$ is the magnetic field. We use the convention $\boldsymbol{\mu}_I = -g_I\mu_{\text{B}}\mathbf{I}/\hbar$. The operators $\mathbf{i}$ and $\mathbf{j}$ are the nuclear spin and angular momentum operators with corresponding quantum numbers m_i and m_j[‡]. ^{40}K has the electronic ground state $4\,^2S_{1/2}$, so $\mathbf{J}$ equals to the spin operator $\mathbf{S}$ and $S = 1/2$.

[†]Eq. 2.8 applies for the atoms in the ground state, for excited atoms see Appendix B

[‡]To avoid confusion in this section, we label the operators $\mathbf{I}$, $\mathbf{S}$, $\mathbf{J}$ and $\mathbf{F}$ in capital letters when only one atom is concerned and for the coupled operators of the two atoms. For systems of two atoms, the individual operators and quantum numbers are labelled in lower case letters.

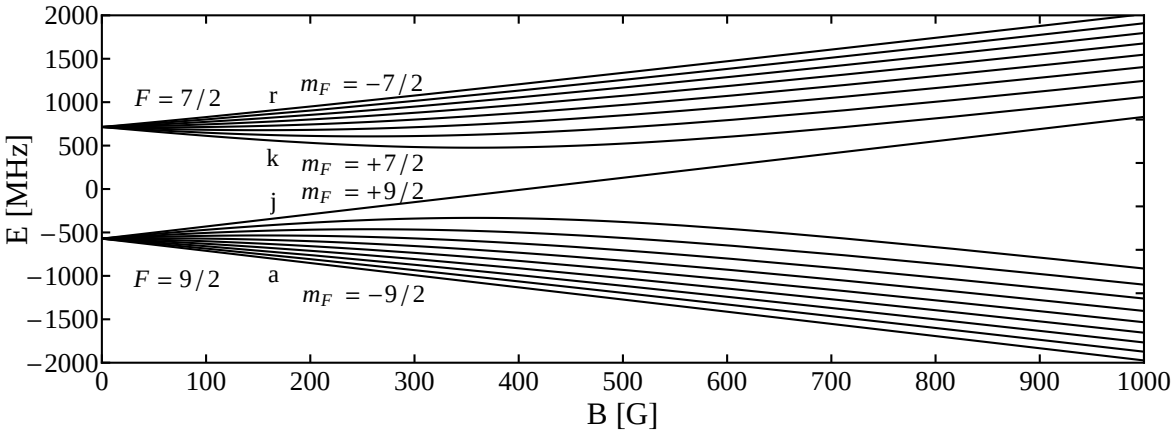

Figure 2.2: Hyperfine structure of ^{40}K in the ground state $|4\,^2S_{1/2}\rangle$. The states are labelled a to r with rising energy and in the low-field basis $|F, m_F\rangle$. In the lower hyperfine manifold, where $F = 9/2$, the states f to j are low-field seeking at low magnetic field. In the upper hyperfine manifold ($F = 7/2$) the states o to r are low-field seeking. The hyperfine structure is inverted unlike in most other alkalis. For more details see Appendix B.

The nuclear spin of ^{40}K is $I = 4$. The energy eigenvalues of the internal Hamiltonian of a ^{40}K atom are shown in Fig. 2.2. The states are labelled with the low-field basis $|F, m_F\rangle$ quantum numbers, where $\mathbf{F} = \mathbf{I} + \mathbf{J}$ and alphabetically with rising energy.

The hyperfine constant of ^{40}K is $a_{\mathrm{hf}} = h \times -285.7308(24)\,\mathrm{MHz}$, resulting in a hyperfine splitting $\Delta E_{\mathrm{hf}} = h \times 1285.79\,\mathrm{MHz}$ of the two hyperfine manifolds. Note that the hyperfine structure is inverted unlike in most other alkalis [Zac42]. In Appendix B the hyperfine structure of ^{40}K is described in more detail and values for all relevant constants are given.

The internal Hamiltonian in Eq. 2.6 can be separated into a term which conserves the total electron spin $\mathbf{H}^+_{\mathrm{int}}$ and a term $\mathbf{H}^-_{\mathrm{int}}$ which couples the different spins. This is done for indistinguishable particles with $j = s = 1/2$ in the symmetrized basis $|SM_SIM_I\rangle$ with $\mathbf{I} = \mathbf{i}_\alpha + \mathbf{i}_\beta$, $\mathbf{S} = \mathbf{s}_\alpha + \mathbf{s}_\beta$ and equal a_{hf}, g_J and g_I.

$$\mathbf{H}^+_{\mathrm{int}} = \frac{a_{\mathrm{hf}}}{2\hbar^2}\mathbf{I}\cdot\mathbf{S} + \frac{\mu_{\mathrm{B}}}{\hbar}(g_J\mathbf{S} + g_I\mathbf{I})\cdot\mathbf{B} \tag{2.9}$$

$$\mathbf{H}^-_{\mathrm{int}} = \frac{a_{\mathrm{hf}}}{2\hbar^2}(\mathbf{i}_\alpha - \mathbf{i}_\beta)\cdot(\mathbf{s}_\alpha - \mathbf{s}_\beta) \tag{2.10}$$

2.2.2 Hamiltonian for the relative motion

The effective interaction $\mathbf{V}$ in the Hamiltonian of the relative motion in Eq. 2.5 can be expressed as the (central) Coulomb interaction $V^{\mathrm{C}}(r)$ of the two atoms with internuclear distance r and total spin $\mathbf{S} = \mathbf{s}_\alpha + \mathbf{s}_\beta$.

$$V^{\mathrm{C}}(r) = \sum_S |S\rangle\, V_S(r)\, \langle S| = \mathcal{P}_s V_s + \mathcal{P}_t V_t. \tag{2.11}$$

Depending on the coupling of the individual spins, the interaction potential $V_S(r)$ has for $s = 1/2$ atoms a singlet (S=0) or a triplet (S=1) character with the respective

singlet and triplet potentials $V_s(r)$ and $V_t(r)$. The operators $\mathcal{P}_s$ and $\mathcal{P}_t$ project out the singlet and triplet components of the wave function respectively. The interaction in Eq. 2.11 can then be rewritten into a sum of a direct V_D and a exchange interaction $J(r)$[Pet02] including the eigenvalues of $\mathcal{P}_s$ and $\mathcal{P}_t$:

$$V^\mathrm{C}(r) = V_\mathrm{D} + J(r)\mathbf{s}_\alpha \cdot \mathbf{s}_\beta \tag{2.12}$$

$$= \frac{V_s(r) - 3V_t(r)}{4} + \left[V_t(r) - V_s(r)\right]\mathbf{s}_\alpha \cdot \mathbf{s}_\beta \tag{2.13}$$

$$= \frac{V_s(r) - 3V_t(r)}{4} + \left[V_t(r) - V_s(r)\right]\left(\frac{1}{2}\mathbf{S}^2 - \frac{3}{4}\right). \tag{2.14}$$

In the asymptote the direct interaction V_D corresponds to the van der Waals potential

$$V_\mathrm{D} = -\frac{C_6}{r^6} - \frac{C_8}{r^8} - \frac{C_{10}}{r^{10}} - \cdots \tag{2.15}$$

$$\approx -\frac{C_6}{r^6}, \tag{2.16}$$

with the van der Waals range

$$r_0 = \frac{1}{2}\left(\frac{2m_\mathrm{r}C_6}{\hbar^2}\right)^{1/4} \tag{2.17}$$

as the characteristic length of the potential [Gri93, Fla99].

In the description of the two-body Hamiltonian in Eq. 2.4, we have not included dipole-dipole coupling. Neglecting dipole-dipole interaction, the two-body Hamiltonian can be separated into a radial and a spin part. The relative Hamiltonian $\mathbf{H}_\mathrm{rel}$ acts only on the radial part of the atoms wavefunction and the internal Hamiltonian $\mathbf{H}_\mathrm{int}$ acts only on the spin part.

2.3 Elastic collisions

The scattering of particles by a potential has been treated extensively in the literature (for example in [Sak94, CT77]); here we present the main results important for the experiments with ^{40}K. The Pauli exclusion principle limits the types of two-body wavefunctions for fermions. When considering the scattering between two fermions the two-body wavefunction needs to be symmetrized properly. In systems of identical fermions s-wave collisions are forbidden due to the Pauli exclusion principle. To obtain the elastic scattering properties the time-independent radial wave equation needs to be solved for given values of l and s [Fli91]:

$$ER_l(r) = \left[\frac{\hbar^2}{2m_\mathrm{r}}\left(\frac{\partial^2}{\partial r^2} + \frac{2}{r}\frac{\partial}{\partial r}\right) + \frac{\hbar^2 l(l+1)}{2m_\mathrm{r}r^2} + V_S(r)\right]R_l(r). \tag{2.18}$$

For $l = 0$ the influence of the scattering potential on the scattered wavefunction in the asymptotic case ($r \to \infty$) can be expressed by the s-wave phase shift η_0. It is:

$$a = -\lim_{k\to 0}\frac{\tan\eta_0}{k} \tag{2.19}$$

The singlet V_s and triplet potentials V_t result in a singlet part a_s and a triplet part a_t of the s-wave scattering length a.
The asymptotic solutions to Eq. 2.18 can be described as a partial wave expansion [Sak94]:

$$\langle \mathbf{X}|\Psi\rangle \overset{\text{large } r}{\longrightarrow} \frac{1}{(2\pi)^{3/2}} \sum_l (2l+1) \frac{P_l(\cos\theta)}{2ik} \left[[1+2ikf_l(k)] \frac{e^{ikr}}{r} - \frac{e^{-i(kr-l\pi)}}{r} \right], \tag{2.20}$$

where $P_l(\cos\theta)$ are Legendre polynomials for the scattering angle θ and $f_l(k)$ is the lth partial wave amplitude. The solution is expressed as a spherically incoming wave $e^{-i(kr-l\pi)}/r$ and an outgoing spherical wave e^{ikr}/r. The scattering event changes the coefficient of the outgoing wave. The partial wave amplitude is connected to a phase shift η_l [Sak94]:

$$f_l(k) = \frac{1}{k\cot\eta_l - ik}. \tag{2.21}$$

For partial waves with $l = 1$ (p-wave) and a van der Waals potential as in Eq. 2.15, the phase shift is related to the p-wave scattering length a_1 [Gau10] as:

$$a_1^3 = -\lim_{k\to 0} \frac{\tan\eta_1}{k^3}. \tag{2.22}$$

Collisions at low energies for partial waves with $l > 0$ are in general suppressed, because a centrifugal barrier forms a threshold with the effective potential

$$V_{\text{th}}(l) = -\frac{C_6}{r^6} + \frac{\hbar^2}{2m_{\text{r}}} \frac{l(l+1)}{r^2}. \tag{2.23}$$

The maximum threshold energy E_{th} can be approximated to

$$E_{\text{th}}(l) = -\frac{C_6}{r_{\text{max}}^6} + \frac{\hbar^2}{2m_{\text{r}}} \frac{l(l+1)}{r_{\text{max}}^2} \tag{2.24}$$

using the local maximum of the effective potential at

$$r_{\text{max}}^4 = \frac{6C_6 m_{\text{r}}}{\hbar^2 l(l+1)}.$$

In the case of ^{40}K the threshold is 100 µK for p-wave ($l = 1$) and 510 µK for d-wave ($l = 2$) partial wave collisions. In the magneto-optical trap we have temperatures up to 190 µK, in the magnetic trap and the optical trap they are in the range of a few 10µK. In the latter traps the main scattering channel will be s-wave.

2.4 Spin Exchange and ^{40}K

Spin exchanging collisions are inelastic. Due to the Zeeman interaction (see Fig. 2.2) the different hyperfine states have different energies depending on the magnetic field. When spin exchange occurs, the energy difference of the total energy between final and initial states $E_f - E_i$ can be negative or positive, leading to exothermic and endothermic collisions respectively. For a positive difference in energy, this is the activation energy

Property	Symbol	Value	unit	Ref.
singlet scattering length	a_s	104.41(9)	a_0	[Fal08]
triplet scattering length	a_t	169.67(24)	a_0	[Fal08]
van der Waals range	r_0	65.02	a_0	
van der Waals coefficient	C_6	3925.9	$E_\mathrm{H} a_0^6$	[Fal08]
van der Waals coefficient	C_8	4.224×10^5	$E_\mathrm{H} a_0^8$	[Fal08]
van der Waals coefficient	C_{10}	4.938×10^7	$E_\mathrm{H} a_0^{10}$	[Fal08]

Table 2.1: Scattering properties of ^{40}K in units of the Bohr radius $a_0 = 5.2917720859 \times 10^{-11}$ m and the Hartree energy $E_\mathrm{H} = 4.35974394 \times 10^{-18}$ J [NIS10].

E_act needed to make spin exchanging collisions happen. In collisions described by the Hamiltonian in Eq. 2.4 the total spin $M_T = m_F + m'_F$ of two colliding atoms in the hyperfine states with quantum numbers m_F and m'_F is conserved. Furthermore in the case of fermions the two-body wave function obeys Fermi-Dirac statistics enforcing an antisymmetric total wavefunction for atoms in identical states. Therefore all spin exchanging s-wave collisions between atoms in the same hyperfine state $m_F = m'_F$ are forbidden. We only consider s-wave collisions between atoms in the electronic ground state $|2S_{1/2}\rangle$ of ^{40}K in this section. Dipolar relaxation, where the atoms enter in a s-wave channel and leave in a d-wave channel, only plays a minor role (away from Feshbach resonances), as the temperature of the cold atoms is far below the d-wave threshold.

In the case of collisions between atoms in the *two hyperfine manifolds* $F = 9/2$ and $F = 7/2$, the collision is exothermic. The energy difference is of the order of the hyperfine splitting $\Delta E_\mathrm{hf} = h \times 1285.79\,\mathrm{MHz}$, corresponding to a temperature of 60 mK. This is much higher than all the trapping potentials employed in this experiment. Atoms in different hyperfine manifolds which undergo spin exchanging collisions will be lost from the trap. In our experiment spin exchange between atoms in the two hyperfine manifolds can play a role during a state preparation step, which will be described in detail in Sec. 4.2.

The case of collisions between ^{40}K atoms *within the lower hyperfine manifold* ($F = 9/2$) needs to be considered for trapped cold clouds and when preparing atoms in specific binary mixtures to measure Feshbach resonances as will be described in Sec. 4.2. When considering binary state mixtures in the lower hyperfine manifold of ^{40}K, there are several combinations of states which are stable or can be made stable against spin exchange. There are in general two possibilities for the final state combination when exchanging one quantum of angular momentum. For neighbouring states one of these combinations is excluded as it is identical to the initial states:

$$|(m_F+1), m_F\rangle \rightarrow |(m_F+2), (m_F-1)\rangle \quad \text{(a)}$$
$$\nrightarrow |(m_F), (m_F+1)\rangle\,. \quad \text{(b)}$$

For states where $\Delta m_F = 2$, one combination is excluded due to the Pauli exclusion

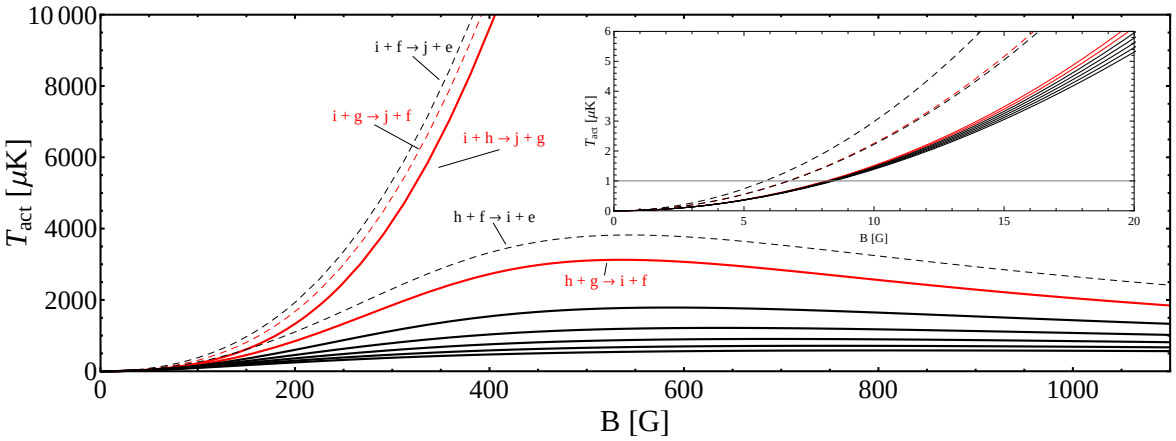

Figure 2.3: Activation temperature T_{act} necessary for spin exchange between atoms in the lower hyperfine manifold, depending on the magnetic field B. The curves are for spin exchanging processes where one unit of angular momentum is exchanged. The solid lines show spin exchange between atoms in neighbouring states $(h+i,\ ...,\ b+c)$. The dashed lines show the non-adjacent spin exchange channels which are present in the f, g, h, i, j mixture. For the channels shown in red the reversed (exothermic) process is possible in the f, g, h, i, j mixture. The inset shows the magnetic field range relevant for the state preparation described in Sec. 4.2.

principle:

$$|(m_F+2), m_F\rangle \rightarrow |(m_F+3), (m_F-1)\rangle \qquad \text{(a)}$$
$$\nrightarrow |(m_F+1), (m_F+1)\rangle\,. \qquad \text{(b)}$$

This can be understood as a time-reversed collision of identical fermions. In general the spin exchange channels for the exchange of one quantum of angular momentum are:

$$|(m_F+i), m_F\rangle \rightarrow |(m_F+i+1), (m_F-1)\rangle \qquad \text{(a)}$$
$$\rightarrow |(m_F+i-1), (m_F+1)\rangle\,. \qquad \text{(b)}$$

The hyperfine structure of ^{40}K is inverted (see Fig. 2.2), so the energy of the state $|m_F+1\rangle$ is always higher than of the state $|m_F\rangle$. The channels labelled as (a) above are therefore endothermic channels, requiring activation energy E_{act} to drive spin exchange. The channels labelled (b) above are exothermic, releasing energy when spin exchange takes place. The activation temperature

$$T_{\mathrm{act}} = E_{\mathrm{act}}/k_{\mathrm{B}} = (E_f - E_i)/k_{\mathrm{B}} \qquad (2.25)$$

corresponds to the temperature at which the activation energy is provided by the thermal energy of the atom cloud. The difference in energy between final and initial states $E_f - E_i$ depends on the magnetic field and results in an activation temperature T_{act} as shown in Fig. 2.3.

For binary mixtures consisting of neighbouring states or states with $\Delta m_F = 2$ it is always possible to stabilize the mixture by increasing the magnetic field or lowering the temperature of the cold atom cloud. The activation temperature necessary T_{act} to drive spin exchange in mixtures of neighbouring states in the lower hyperfine manifold is shown as solid lines in Fig. 2.3. The activation temperature T_{act} for states with $\Delta m_F = 2$ is even higher. As mixtures of neighbouring states and of states with $\Delta m_F = 2$ can be made stable, also mixtures of atoms in three adjacent states can be stabilized. The fact that ^{40}K is fermionic and has an inverted hyperfine structure allows for the realization of a multitude of stable state combinations, exceeding the possibilities in other alkalis.

2.4.1 Populated states in the magnetic trap

The cold atoms in the magnetic trap (and in the optical dipole trap) are in the states f, g, h, i, j (labelled as in Fig. 2.2). The combination $|9/2 + 7/2\rangle$ $(j + i)$ is stable against spin exchanging collisions as there is no other combination with $M_T = 8$. The binary mixture $|9/2 + 5/2\rangle$ $(j + h)$ is stable against spin exchanging collisions as the only possible final state combination is excluded due to the Pauli exclusion principle[§]. The mixture f, g, h, i, j has in total nine channels, where spin exchanging s-wave collisions can exchange one unit of angular momentum between two atoms. Of those nine channels six are endothermic, the three remaining channels are exothermic and correspond to the reversed processes of endothermic channels.

Of the six endothermic channels, five involve neighbouring states or states with $\Delta m_F = 2$. The dashed lines in Fig. 2.3 show the spin exchange channels present in the f, g, h, i, j mixture for non-adjacent states. The red lines correspond to the reverse of the three exothermic spin exchanging channels possible for atoms in the mixture. The energy release from the exothermic spin exchanging processes leads to loss from the trap or – for low magnetic fields – a heating of the cold atom cloud.

2.4.2 Scattering rate for spin exchange

Apart from the existence of decay channels, in an experiment the actual loss rate and with that the stability of a mixture of two states is determined by the scattering rate. The two-body scattering rate K_2, depends on the density of the involved states, the spatial overlap of the states and the difference between singlet and triplet scattering length [Pet02]:

$$K_2 = 4\pi(a_s - a_t)^2 v'_{\mathrm{rel}} \left| \langle F'_\alpha \, m'_{F,\alpha} \, F'_\beta \, m'_{F,\beta} | \mathbf{s}_\alpha \cdot \mathbf{s}_\beta | F_\alpha \, m_{F,\alpha} \, F_\beta \, m_{F,\beta} \rangle \right|^2 , \tag{2.26}$$

where $|F'_\alpha \, m'_{F,\alpha} \, F'_\beta \, m'_{F,\beta}\rangle$ and $|F_\alpha \, m_{F,\alpha} \, F_\beta \, m_{F,\beta}\rangle$ denote the final and initial hyperfine states and v'_{rel} is the relative velocity of the atoms in the final state. It is

$$v'_{\mathrm{rel}} = \sqrt{\frac{2}{m_{\mathrm{r}}}(E_{\mathrm{kin}} + E_\alpha^{\mathrm{HF}} + E_\beta^{\mathrm{HF}} - E_\alpha^{\mathrm{HF}'} - E_\beta^{\mathrm{HF}'})}, \tag{2.27}$$

[§]The same arguments hold for the combinations $|-9/2 + -7/2\rangle$ $(a{+}b)$ and $|-9/2 + -5/2\rangle$ $(a{+}c)$.

with the reduced mass $m_\mathrm{r} = (m_\alpha m_\beta)/(m_\alpha + m_\beta)$ and the kinetic energy E_kin of the initial states. The energies E_i^HF and $E_i^{\mathrm{HF}'}$ denote the hyperfine energies of the initial and final states. To calculate the spin exchange rate between atoms of the same atomic species, the hyperfine basis $|F_\alpha\, m_{F,\alpha}\, F_\beta\, m_{F,\beta}\rangle$ is transformed to the total spin basis $|S\, M_S\, I\, M_I\rangle$.

From the factor $(a_s - a_t)^2$ in Eq. 2.26 follows, that the two-body inelastic loss rate K_2 is expected to be low, when the singlet and triplet scattering lengths are similar. This effect can also be understood as an interference effect as has been shown for ^{87}Rb [Kok97, Bur97]. In the group at JILA [DeM01] an upper limit for the the non-resonant spin exchange rate in ^{40}K was determined to be $K_2 < 2 \times 10^{-14}\,\mathrm{cm}^3/\mathrm{s}$. Compared to other alkali atoms where $K_2 \approx 10^{-11}\,\mathrm{cm}^3/\mathrm{s}$ [Pet02], this is rather low.

2.5 Feshbach resonances

So far we have covered the scattering properties for scattering from a central potential (Sec. 2.3). The potential determines the value of the scattering length a at low temperatures. A form of resonant scattering are Feshbach resonances; they are an important tool to control the interaction between ultracold atoms, as they allow to widely tune the scattering length of the atoms.

In the asymptotic case ($r \to \infty$) the hyperfine energy of the two colliding atoms with distance r determines the total energy of the atom pair. The total energy of the unbound pair forms the so-called open channel, as (s-wave) collisions are always possible even when $T \to 0$. Feshbach resonances occur when in addition to the open channel there is also a two-body bound potential, a so-called closed channel, present. All scattering potentials which have a higher asymptotic energy than the open channel are referred to as closed channels (see Fig. 2.4). Due to resonant coupling to a bound state with binding energy E_b within a closed channel the scattering length a can diverge.

The divergence of the scattering length occurs when the bound state in the closed channel shifts into resonance with the energy of the open channel. Due to the difference in magnetic field dependence of the open and closed channel, the closed channel can be moved relative to the energy of the open channel by applying an external magnetic field. The bound state in the closed channel is resonant at a certain magnetic field B_0, when there is a coupling between the open and the closed channel. At the resonance at magnetic field B_0 the scattering length diverges as shown in Fig. 2.5.

The theory of Feshbach resonances [Fes58, Fes62] was originally developed for nuclear physics, where the resonances do not depend on an external magnetic field but on the energy of the scatterers. The application of Feshbach resonances to alter the sign and the strength of the interaction in ultracold atoms by changing an external field was proposed by [Tie92, Tie93]. The first experimental observation of this effect in ultracold atoms were made in ^{23}Na [Ino98] and in ^{85}Rb [Cou98]. A detailed review of Feshbach resonances in ultracold atoms is given in [Chi10].

If only one closed channel is present the scattering length can be expressed as the sum of a resonant part a_res and the background scattering length a_bg originating from the open channel:

$$a(B) = a_\mathrm{bg} + a_\mathrm{res}(B).$$

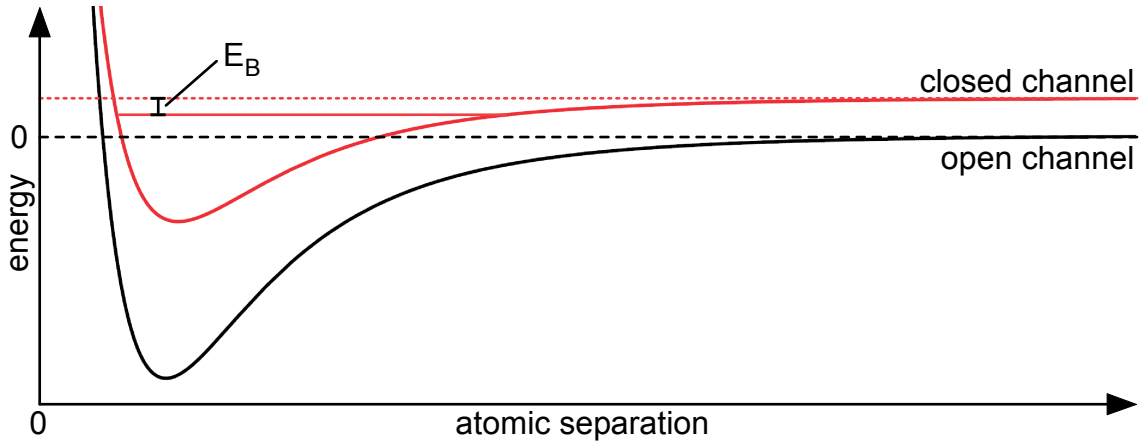

Figure 2.4: Two-channel model for a Feshbach resonance. When two atoms collide at energy E in the open (entrance) channel (black curve), they can couple resonantly to a bound state with binding energy E_b within a molecular potential (closed channel) (red curve). The coupling leads to a diverging scattering length. If there is a difference in magnetic moment of the open and the closed channel, the energy of the bound state in the closed channel can be tuned to cross the energy threshold of the two atoms by changing the magnetic field.

The s-wave scattering in absence of inelastic two-body channels is described by [Moe95]

$$a(B) = a_{\mathrm{bg}}\left(1 - \frac{\Delta B}{B - B_0}\right), \tag{2.28}$$

with the off-resonant background value of the scattering length a_{bg}, the Feshbach resonance position B_0 and its width ΔB. The width is defined via the position of the zero-crossing of the Feshbach resonance $B(a = 0) = B_0 + \Delta B$. The behaviour of the scattering length around a Feshbach resonance is shown in Fig. 2.5. The scattering cross section is given by:

$$\sigma = g\frac{4\pi a^2}{1 + k^2a^2} = g\frac{4\pi a_{\mathrm{bg}}^2\left(1 - \frac{\Delta B}{B-B_0}\right)^2}{1 + k^2a_{\mathrm{bg}}^2\left(1 - \frac{\Delta B}{B-B_0}\right)^2}, \tag{2.29}$$

where k is the momentum and g is a symmetry factor. It is $g = 1$, except for the case of two identical atoms (same species and same state) in a Maxwellian gas [Chi10]. The difference in magnetic moment between the open and the closed channel $\Delta\mu = \mu_0 - \mu_c = -\partial E_b/\partial B$ describes the coupling strength C between the open and the closed channel.

$$C \equiv a_{\mathrm{bg}}\Delta B\Delta\mu.$$

Further useful expressions to describe a Feshbach resonance are the length scale [Pet04]

$$R^* \equiv \frac{\hbar^2}{2m_{\mathrm{r}}a_{\mathrm{bg}}\Delta B\Delta\mu},$$

the width

$$\Gamma \equiv \frac{\hbar^2 k}{m_{\mathrm{r}}R^*} = 2Ck$$

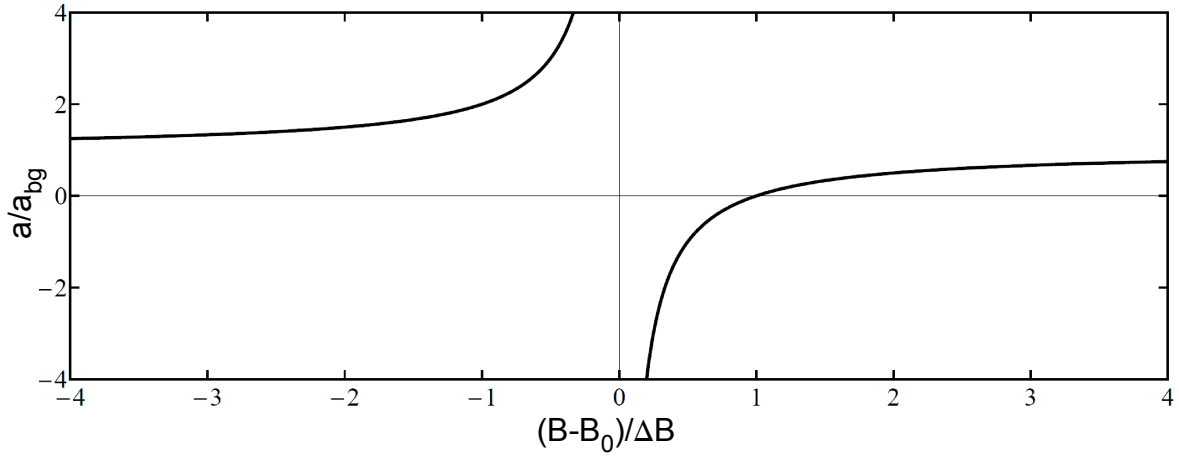

Figure 2.5: Divergence of the s-wave scattering length a around a Feshbach resonance at the magnetic field B_0.

and the resonance strength which can be described by a dimensionless parameter [Chi10]:

$$s_{\mathrm{res}} = \frac{R^*}{r_0}$$

For large positive values of a there is a molecular state with binding energy

$$E_b = \frac{\hbar^2}{2m_{\mathrm{r}}a^2}. \tag{2.30}$$

Further away from the resonance and for positive values of a the energy is proportional to the magnetic field B, with a slope depending on the difference of the magnetic moments of the open and closed channel. The quadratic dependence close to the Feshbach resonance is caused by the coupling between open and closed channel.

To calculate the exact position and widths of Feshbach resonances the potentials of the involved channels are needed and their coupling has to be computed. In general this requires the (numerical) solving of a large number of coupled equations using coupled channel calculations (CC). Simple models like the asymptotic bound state model (ABM) and the multichannel quantum defect theory (MQDT) are useful to assign resonances and allow for the calculation of approximate resonance positions with less computational effort than needed for CC. In the experiments presented in this thesis we used the ABM to assign and locate Feshbach resonances. The following section gives a brief introduction to this model.

2.6 Asymptotic bound state model

The asymptotic bound state model (ABM) was initially developed (see [Tie10b] and references therein) to assign features observed in experiments with ^{6}Li - ^{40}K [Wil08] to the bound states and closed channels causing the Feshbach resonances. The main idea is that the two-body Hamiltonian in Eq. 2.4 is diagonalized and the energy of the bound molecular states is varied to fit known resonances. The input parameters are the singlet a_s and the triplet scattering length a_t and the C_6 coefficient to describe the

van der Waals tail of the interatomic potential. It is not necessary to solve the radial Schrödinger equation.

The model is called asymptotic because it is assumed that the detailed behaviour of the potential at small interatomic distances can be neglected as the main contribution to the position of Feshbach resonances stems from the asymptotic behaviour of the atoms. In the course of diagonalizing the Hamiltonian, the overlap between the wavefunction in the singlet V_s and the triplet potential V_t needs to be computed. This overlap is ≈ 1. For a first calculation of the position of Feshbach resonances there are thus only three input parameters necessary. The calculation can be improved by optimizing the overlap and the bound state energies of the molecular bound states to fit data determined in experiments. With the improved assumptions for the energies and the overlap, the position of other Feshbach resonances can be determined. The ABM has the advantage that all possible resonances, however narrow, will be predicted with relatively little computational effort. These results can then be used as input for the exact coupled channel calculations. The assignment of s- and p-wave is also immediately clear with ABM.

The ABM has been applied to mixtures of ^{6}Li - ^{40}K [Wil08, Tie10c], ^{85}Rb - ^{87}Rb, ^{6}Li - ^{87}Rb [Li08], ^{6}Li - ^{85}Rb [Deh10], ^{40}K - ^{87}Rb [Tie10c], ^{3}He* - ^{4}He* [Goo10] and to ^{23}Na [Kno11]. The original ABM has been extended to also include dipole-dipole interactions and overlapping resonances [Goo10], and radio-frequency induced resonances [Tsc10]. The ABM is also used to calculate the widths of resonances [Tie10c]. This involves rewriting the Hamiltonian in terms of the closed and open channel contributions and extracting the coupling between them. For the individual mixtures and species some adaptations have to be made, it turns out that for ^{6}Li - ^{40}K one bound state is sufficient. In ^{40}K two bound states play a role as well as the large background scattering length (see Sec. 5.3.3).

In our experiment we used the ABM together with values of the four resonances known at that time as well as the input parameters a_s, a_t and C_6 from molecule spectroscopy [Fal08] to get initial predictions for Feshbach resonances in the hyperfine state mixtures of ^{40}K. Once new measurements were obtained, the overlap and binding energies were optimised (see Sec. 5.3.3) and further predictions for other hyperfine state mixtures were calculated.

2.7 Trapped fermions

We use magnetic and optical traps to confine the ^{40}K. These trapping potentials are described in detail in the appendices A and B. The potential has an effect on the density of states and with that on the Fermi energy E_F. As depicted in Fig. 2.1, the Fermi energy E_F is defined as the energy of the highest state in a potential occupied at $T = 0$. The Fermi temperature is defined accordingly as $T_F = E_F/k_\mathrm{B}$. For an ideal gas in a trapping potential $U(\mathbf{r})$, the density of states is

$$g(\epsilon) = \frac{1}{h^3} \int \delta \left(\epsilon - \left[\frac{\mathbf{p}^2}{2m} + U(\mathbf{r}) \right] \right) d\mathbf{p} d\mathbf{r}. \tag{2.31}$$

From the definition of the Fermi energy follows the total number of atoms N:

$$N \equiv \int_0^{E_\mathrm{F}} g(\epsilon)\, d\epsilon. \tag{2.32}$$

With Eq. 2.31 and 2.32 and a known potential the Fermi energy E_F can be calculated. The optical dipole trap used in our experiment, can be approximated at low temperatures by a harmonic potential[¶], with

$$U_\mathrm{ODT}(x,y,z) = \frac{m}{2}(\omega_r^2 x^2 + \omega_r^2 y^2 + A\omega_r^2 z^2)$$

this results in the density of states [But97]

$$g_\mathrm{ODT}(\epsilon) = \frac{\epsilon^2}{2A(\hbar\omega_r)^3} \tag{2.33}$$

and

$$E_\mathrm{F} = \hbar\omega_r (6AN)^{1/3}, \tag{2.34}$$

where $A = \omega_z/\omega_r$ is the aspect ratio of the optical dipole trap, and the trapping frequencies are determined by the mass of the atoms and the laser detuning as described in Appendix A. For the linear magnetic trap as employed in the experiment (see Sec. 3.5.1 and B.3) with a potential of the form

$$U_\mathrm{MT}(x,y,z) = \frac{U_0}{2}\sqrt{x^2+y^2+4z^2},$$

the density of states is given by [Bag87]:

$$g_\mathrm{MT}(\epsilon) = \frac{16\sqrt{2}}{105\pi}\left(\frac{2\sqrt{m}}{\hbar U_0}\right)^3 \epsilon^{7/2}. \tag{2.35}$$

The Fermi energy in this case is

$$E_\mathrm{F} \approx 1.5962 N^{2/9}\left(\frac{\hbar U_0}{\sqrt{m}}\right)^{2/3}. \tag{2.36}$$

2.7.1 Fermi degenerate density distribution

For an ideal gas below the Fermi temperature T_F the distribution is a Fermi-Dirac distribution

$$f_\mathrm{FD}(\epsilon) = \frac{1}{\frac{1}{\zeta}e^{\epsilon/k_\mathrm{B}T}+1}, \tag{2.37}$$

with the fugacity $\zeta \equiv \exp(\mu/k_\mathrm{B}T)$ depending on the chemical potential μ.

To calculate the density distribution of a degenerate gas in a potential, a semi-classical approximation can be used as long as the thermal energy of the gas $k_\mathrm{B}T$ is

[¶]The atoms in the optical dipole trap are in a Gaussian potential, which can be approximated harmonically for low atom temperatures. The density distribution for thermal atoms in a Gaussian potential is described in Appendix A.

much larger than the spacing $\hbar\omega$ of the (quantum mechanical) levels of the trapping potential $U(\mathbf{r})$. In this case the density distribution is given by:

$$n_{\mathrm{FD}}(\mathbf{r}) = \frac{1}{h^3}\int \frac{1}{e^{(\mathbf{H}(\mathbf{p},\mathbf{r})-\mu)/k_{\mathrm{B}}T}+1}\, d\mathbf{p}. \tag{2.38}$$

Integration over all possible momenta $\mathbf{p}$ results in the density distribution of a degenerate cloud of fermions at finite temperatures $0 < T < T_F$:

$$n_{\mathrm{FD}}(\mathbf{r}) = -\left(\frac{2\pi m k_{\mathrm{B}}T}{h}\right)^{3/2} \mathrm{Li}_{3/2}(-\zeta e^{-U(\mathbf{r})/k_{\mathrm{B}}T}), \tag{2.39}$$

with the polylogarithm function (Jonquière's function) $\mathrm{Li}_n(x) \equiv \sum_{k=1}^{\infty} x^k/k^n$. The number of atoms for a harmonic confinement is obtained by integrating Eq. 2.39 over $\mathbf{r}$:

$$N = -\frac{1}{A}\left(\frac{k_{\mathrm{B}}T}{\hbar\omega_r}\right)^3 \mathrm{Li}_3(-\zeta). \tag{2.40}$$

Combining this result with the Fermi energy $k_{\mathrm{B}}T_{\mathrm{F}}$ in a harmonic trap Eq. 2.34 the fugacity depends only on T/T_{F}:

$$\frac{T}{T_{\mathrm{F}}} = (-6\,\mathrm{Li}_3(-\zeta))^{-1/3} \tag{2.41}$$

In the experiments we determine the density distribution by means of absorption imaging (see 3.8.3) along the axial direction of the dipole trap. This results in a projection of the atom density on a two-dimensional optical density profile, which we can calculate for a harmonic potential by integrating Eq. 2.34 over y[‖].
The imaging is usually done after releasing the atoms from the trap and some expansion of the cloud in time-of-flight. In the case of a harmonic trap it has been shown [Bru00], that the description of an ideal Fermi gas after free expansion only requires a rescaling of the spatial coordinates x_i in the density distribution Eq. 2.39, similar to the bosonic case [Cas96, Kag96]. The rescaled coordinates $x_i'(t)$ are given by

$$x_i'(t) = \frac{x_i(0)}{\sqrt{1+\omega_i^2 t^2}}, \tag{2.42}$$

when the harmonic trapping potential with trapping frequencies ω_i is switched off at $t = 0$. For a harmonic trap the cloud maintains the aspect ratio and shape it had in the trap after free expansion. This shape invariance only holds for harmonic potentials and simplifies the analysis of the absorption images tremendously. From the absorption images the number of atoms and the temperature of the cloud can be determined using the rescaled density profiles [But97, DeM01].

[‖]The axial (z-) direction of the dipole trap corresponds to the y-axis in the coordinate system of the experiment as depicted in Fig. 3.2.

Chapter 3

Experimental setup

3.1 Introduction

In this chapter the experimental setup is described. The experiments are done using the apparatus designed and developed for mixtures of ultracold ^{6}Li and ^{40}K. At the time this apparatus was devised there were no other experiments on this specific mixture. Additionally, the scattering properties between the atomic species were not yet known, so the design had to make allowances for possible slow thermalization between the species. Recently the groups in Munich, in Innsbruck, at the MIT and in Paris have also built experiments for ^{6}Li and ^{40}K. The group in Munich [Tag06] included ^{87}Rb as a third atomic species in their setup to ensure efficient cooling. ^{87}Rb had been brought to degeneracy previously together with both ^{40}K [Roa02, Ino04] and ^{6}Li [Sil05], after the interspecies scattering lengths had been determined [Fer02, Sil05]. In the group in Innsbruck an all-optical approach was chosen, resulting in large numbers of ^{6}Li and low numbers of ^{40}K. In that experiment efficient thermalization of the sample is ensured by evaporating on the high-field side of a Feshbach resonance in lithium at 834 G [Wil08, Spi09]. The potassium is kept in the lowest hyperfine state and is sympathetically cooled by the lithium. In the group at the MIT the bosonic isotope ^{41}K is used as a coolant [Wu11]. The group in Paris chose an approach similar to ours [Rid11b, Rid11a], relying on the thermalization between ^{6}Li and ^{40}K.

We decided on a setup which combines magnetic and optical trapping. A magnetic trap can be efficiently loaded from a magneto-optical trap (MOT) and provides large atom numbers [Ono00, Sta07]. An optical dipole trap has the advantage that all hyperfine states can be trapped and the trapping potential is identical for all states of one atomic species. Loading the dipole trap from a magnetic trap requires less optical power and a smaller trapping volume than loading it directly from a MOT. Two aspects of the design make the cold atoms easily (optically) accessible: firstly we use an optically plugged magnetic trap [Dav95a] instead of a more commonly used Ioffe-Pritchard type trap [Pri83]. Secondly the optical dipole trap is employed as optical tweezers to transport the atoms [Gus01] to a science cell where the experiments are done. In many cold atom experiments magnetic transport is employed instead, in which a cascade of coils or moving coils are used to transfer the atoms [Gre01]. The science cell is a quartz cell offering good optical access with a small working distance for the

optics.

Producing samples of ultracold atoms requires a vacuum system, lasers tuned close to the transition frequencies of the atoms, a magnetic trap, an off-resonant optical dipole trap or a combination of both to cool the gas close to degeneracy.

Much of the experimental setup has already been described in detail in the thesis of T.G. Tiecke [Tie09a]. The present chapter summarizes the experimental setup putting emphasis on added components and the parts essential for the experiments described in this thesis. In section 3.2 the vacuum system is described, the laser system is covered in section 3.3 and the magneto-optical trap in section 3.4. In section 3.5 the optically plugged magnetic trap is explained including its fast switching electronics. Our optical dipole trap and the feedback circuit with large dynamic range used to stabilize its intensity are presented in section 3.6. The coils used to produce homogeneous and stable magnetic fields for Feshbach measurements are covered in section 3.7. The experimental sequence, the preparation and detection of the Zeeman states and the calibration of the Feshbach coils are described in Chapter 4.

3.2 Vacuum system

The vacuum system is shown in Fig. 3.1 and Fig. 3.2. It consists of four parts: a stainless steel chamber (labelled (c) in Fig. 3.1) where the initial cooling and trapping is done, a two-dimensional MOT (2D-MOT) source for lithium (h), a 2D-MOT source for potassium (a) and a small quartz cell as a science cell (d).

The stainless steel chamber (Kimball Physics Inc., MCF800-SO2000800-A) in the middle is used for the MOT, magnetic trapping, evaporation and the loading of the optical trap. The chamber is cylindrical and has eight CF40 ports on the mantle (labelled 1–8 in Fig. 3.1) and CF160 ports on top and bottom. Two of the CF40 ports (numbered 1 and 5) are taken up by the 2D-MOTs. Another four (numbered 2,4,6 and 8) are used for MOT beams. Of the remaining two, one (7) is used as an input port for the dipole trap, the plug beam and the horizontal imaging light. The last port (3) hosts the science cell. All vacuum windows are uncoated and of optical quality. In the big ports on the top and bottom of the chamber uncoated quartz windows with a diameter of 113 mm protrude bucket-like into the steel chamber. The windows are connected to CF150 re-entry flanges with a non-magnetic glass-to-metal seal (Vacom). The coils employed for the magneto-optical trap (MOT) and the magnetic trap are placed close to the windows. The re-entry flanges were chosen to ensure a small distance between the coil centres (see Fig. 3.7). The two MOT beams for the vertical direction enter the chamber through the hollow core of the coils.

Connected to the main vacuum chamber via a four-way cross is a titanium sublimation pump (Leybold, V150) and via a 60 cm long tube of diameter 2 1/2 inch (labelled (e) in Fig. 3.1) a 55 l/s ion pump (Varian, Vacion Plus 55 Starcell). The current reading of the ion pump controller (Varian, Midivac) is below the detection limit (1×10^{-7} A), corresponding to a pressure $P < 6 \times 10^{-10}$ mbar. As an indicator of the vacuum quality we use the lifetime of the atoms in the optical dipole trap (≈ 40 s). A T-piece just before the ion pump allows the connection of a turbo pump through an all-metal valve (Varian, 951-5027).

Probably due to residual argon in the system the ion pump needs an occasional

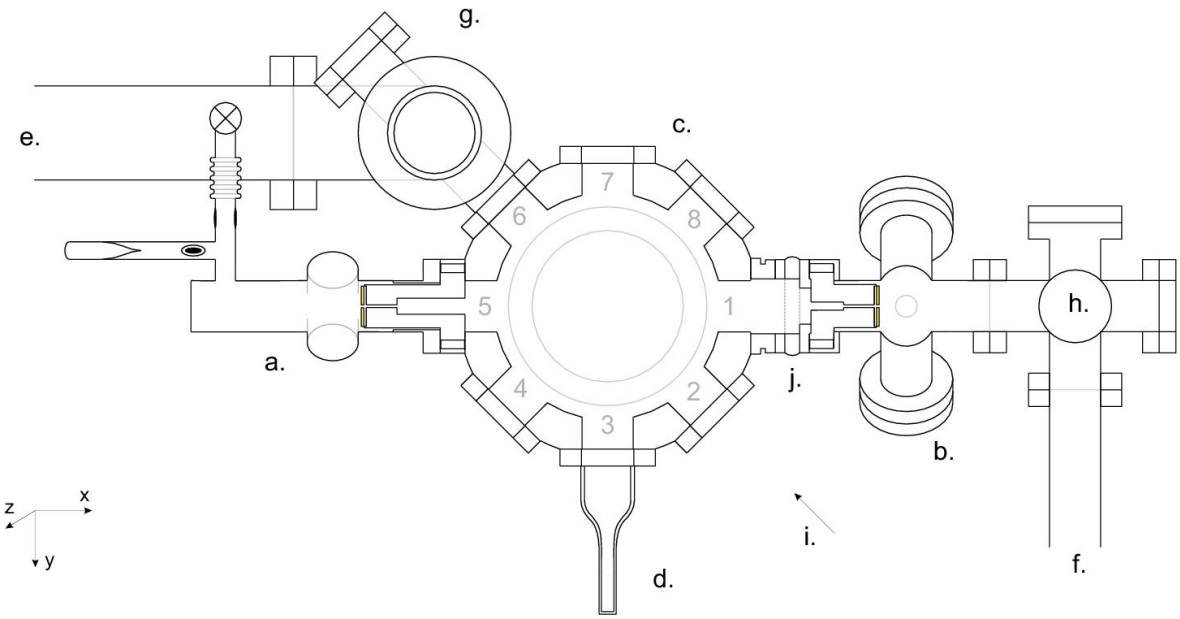

Figure 3.1: The vacuum system as seen from above schematically: (a) potassium 2D-MOT source, (b) lithium 2D-MOT source, (c) main vacuum chamber, (d) science cell, (e) CF63 tube to the main 55 l/s ion pump, (f) CF40 tube leading to the 40 l/s ion pump (g) and (h) titanium sublimation pumps (mounted vertically), (i) direction of view in Fig. 3.7 and (j) gate valve between lithium 2D-MOT and main chamber. This figure is taken from [Tie09a].

bake-out. The argon saturates the ion pump and reduces the ultimate vacuum. In the experiment it is then noticeable that the lifetime of the atoms in the optical dipole trap shortens to $\approx 15\,\mathrm{s}$. A bake-out of the ion pump was necessary every 6 – 9 months. Argon was introduced into the system during the first bake-out of the vacuum system [Tie09a] and has since then been pumped by the ion pump through the differential pumping section connecting the ^{40}K 2D-MOT to the main chamber. When a bake-out of the ion pump is necessary, it is heated to just below 400 °C for several hours while a turbo-molecular pump disposes of the gas load. As the ion pump is cooling down, the titanium sublimation pump connected to the main chamber is run for about one minute at 50 A, after degassing it at 25 A.

The lithium 2D-MOT is pumped by a 40 l/s ion pump (Varian, Vacion Plus 40 Starcell) and another titanium sublimation pump (Leybold, V150)(h). This titanium pump was never used since the initial bake-out and the ion pump shows no load when the lithium oven is heated. This confirms the reputation of alkalis as efficient getters in high-vacuum applications. The lithium 2D-MOT can be separated from the rest of the vacuum system with a gate valve (Leybold, UHV 28699).

Attached to the main chamber via a glass-to-metal transition is the quartz science cell with a length of 42 mm and a 12.7 mm^2 cross-sectional area produced by Techglass Inc. (in Aurora, Colorado, USA). The science cell allows for excellent optical access. Coils designed to produce a highly homogeneous magnetic field to measure Feshbach resonances are built around the science cell (see section 3.7).

The potassium 2D-MOT cell is custom-made of glass by Techglass. A four-way cross with optical quality windows (diameter 30 mm) provides access for the four 2D-

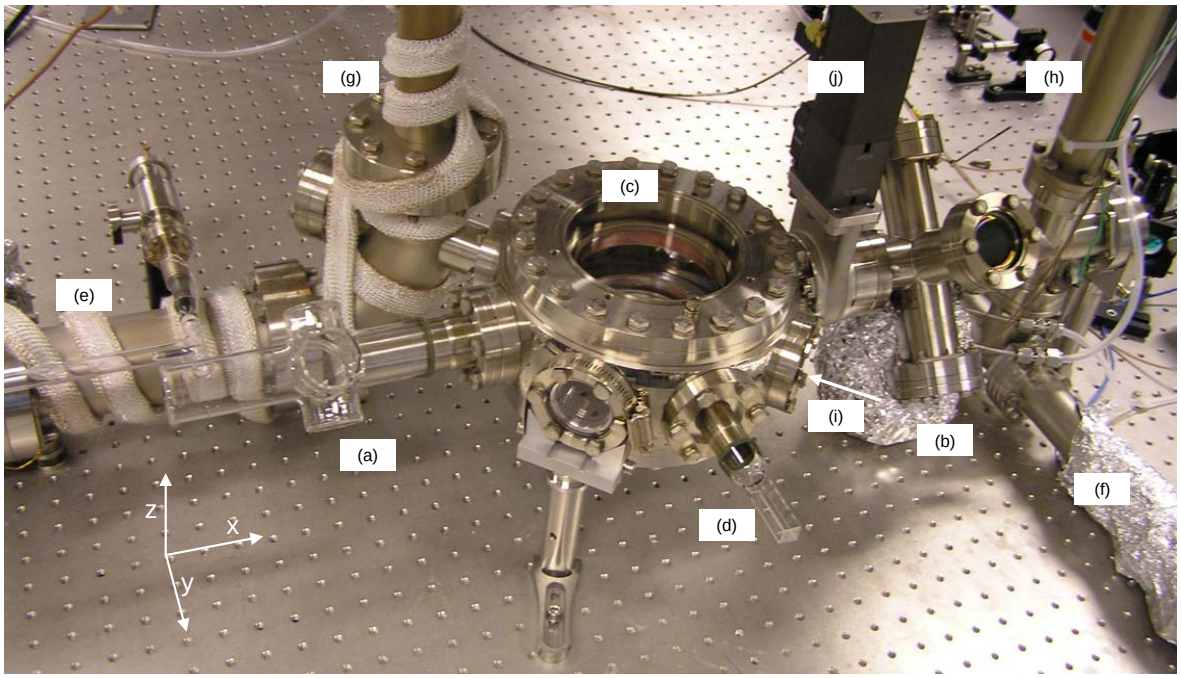

Figure 3.2: Photograph of the vacuum system. The parts are labelled (a) to (j) as in Fig. 3.1.

MOT beams cooling the atoms in radial direction (see Fig. 3.5 and Fig. 3.6). The cell is connected via a glass-to-metal transition to a CF40 flange. A differential pumping section of 23 mm length and 2 mm diameter connects the 2D-MOT to the the main chamber. Mounted in front of the differential pumping tube is a gold mirror with a 2 mm hole in its centre. A distance of 2 mm between the back of the mirror and the differential pumping tube ensures efficient pumping between the two surfaces. The gold mirror can be used to reflect a probe beam or a one-dimensional optical molasses beam. Opposing the mirror on the other end of the 2D-MOT cell is a fifth optical quality window which is used for probe, cooling and push beams along the axis of the 2D-MOT.

Connected to the side of the 2D-MOT cell is a glass tube of 13 mm diameter leading via a T-piece to a break-seal ampule containing ^{40}K-enriched potassium. The glass tube ends via a glass-to-metal transition and bellows in a CF16 flange. The flange was initially intended to pump the 2D-MOT cell but was never used during the baking and remains sealed with a valve [Tie09a]. As a source for the ^{40}K we us KCl enriched to an abundance of 6% ^{40}K (Trace Science International). The distillation into the break-seal ampule was done by Techglass. To achieve the necessary vapour pressure in the 2D-MOT, the entire cell is heated with heater tape and insulated with aluminium foil.

To complete the description of the vacuum system, it is mentioned that we have built the first realisation of a 2D-MOT for lithium. It is fed by an effusive oven and results in an output flux up to $3 \times 10^9/\,\mathrm{s}$. Lithium reacts with glass, therefore we chose a stainless steel chamber for the lithium 2D-MOT. The windows admitting the MOT light are under a 45° angle to the main axis of the lithium beam emitted from the oven, so the lithium cannot reach the windows under normal operation. The lithium

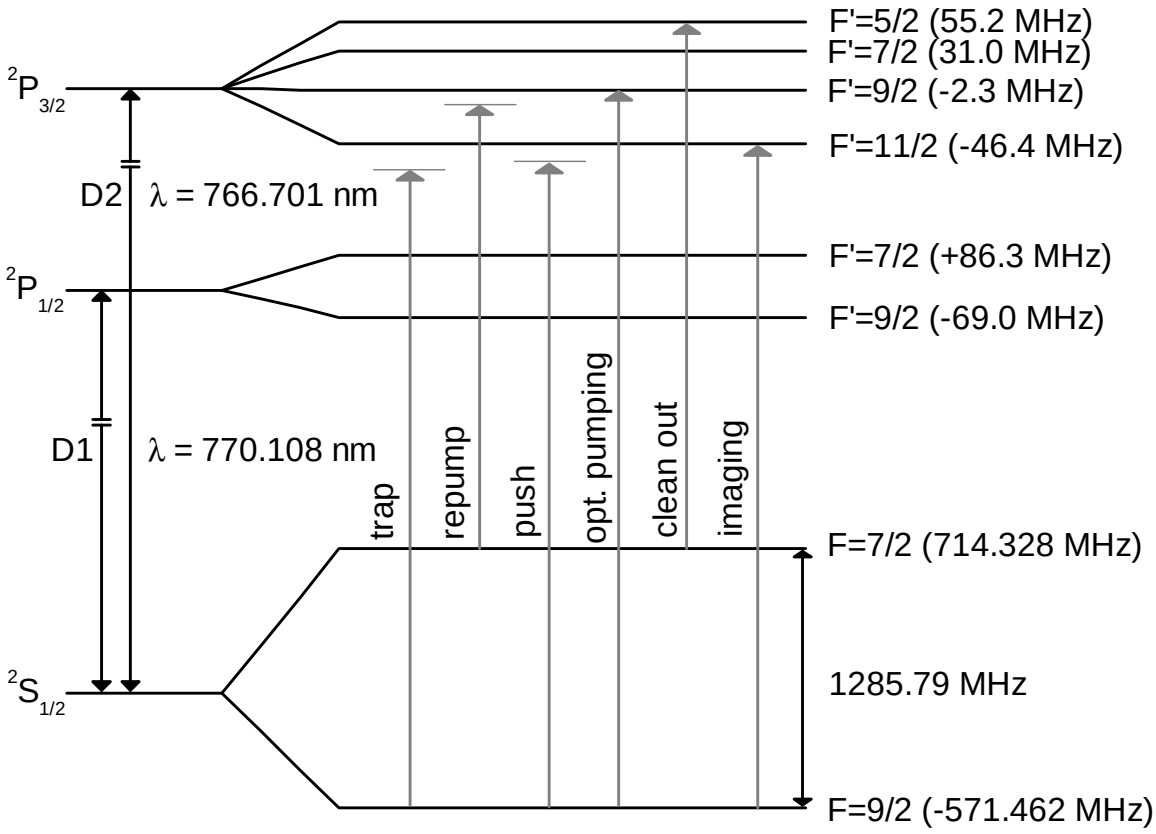

Figure 3.3: Optical spectrum of ^{40}K with D1 and D2 lines. The transitions used for cooling, trapping and imaging are indicated. The numerical values originate from [Ari77] and [Fal06]. Unlike in other isotopes of potassium, the hyperfine structure is inverted in ^{40}K.

2D-MOT is also connected to the main chamber via a differential pumping tube with a gold mirror in front (identical to the potassium 2D-MOT). The principle is described in detail and predicted to work also for other light atomic species in [Tie09b] and [Tie09a].

3.3 Laser system

All manipulation of ^{40}K with light is done on the D2 line, where we call the transition $|^2S_{1/2}, F = 9/2\rangle \rightarrow |^2P_{3/2}, F = 11/2\rangle$ the *trap transition* and the $|^2S_{1/2}, F = 7/2\rangle \rightarrow |^2P_{3/2}, F = 9/2\rangle$ is referred to as the *repump transition* (see Fig. 3.3). Light with frequencies tuned close to those transitions we refer to as trap and repump light respectively. In contrast to many other alkali isotopes, ^{40}K has a sufficiently small hyperfine splitting in the ground state (ΔE_{hf}=1285.79 MHz) to allow for the use of an acousto-optical modulator (AOM) to bridge the frequency difference.

One master laser (Toptica DLX110) is stabilized in frequency. The output power (350 mW) is split into several beams, which are shifted by AOMs to the proper frequencies for the beams to trap, repump and image the atoms. To have sufficient power, the trap and repump light is amplified by tapered amplifiers. In Fig. 3.4 the simpli-

fied optical setup is shown omitting beam-shaping optics and mirrors. The repump frequency is generated by shifting the master frequency by 1143 MHz with an AOM from Brimrose (GPF-1240-200-766). All other frequencies used to manipulate the ^{40}K are obtained using AOMs by Isomet.

The DLX110 laser is stabilized to a polarization Zeeman spectroscopy. We lock the laser to the unresolved $|^2S_{1/2}, F = 1\rangle \rightarrow |^2P_{3/2}\rangle$ transition in ^{39}K. Light from the master laser is brought via a polarization-maintaining fibre to a separate optical table and its frequency is shifted by -260 MHz with an AOM by Crystal Technologies. The linearly polarized light ($\approx$ 200 µW) passes through a heated vapour cell ($\approx$ 40 °C) filled with potassium in natural abundance. A partial reflector ($R = 10\%$) reduces the power in the retro-reflected beam such that the two beams form a pump-probe setup of a Doppler-free saturation spectroscopy [Lev74, Bir74]. The vapour cell is placed in a homogeneous magnetic field of a few Gauss. The field is parallel to the light, resulting in σ^+ and σ^- transitions ($\Delta m_F = \pm 1$), being the allowed optical transitions. The σ^+ and σ^- transitions are shifted in frequency due to the Zeeman shift and differ in strength due to different Clebsch-Gordon coefficients. By placing a quarter waveplate and a polarizing cube in the path of the probe beam as shown in Fig. 3.4, the two circular polarizations can be split and detected seperately by photodiodes (OPT101P-ND). By electronically subtracting the two photodiode signals a dispersive signal to lock the laser is retrieved. Two different stages stabilize the laser: one fast loop (bandwidth $\approx$ 4 kHz) feeds back to the diode current of the master laser and one slower loop (bandwidth $\approx$ 1 Hz) feeds back to the piezo-electric actuator controlling the grating position in the DLX110. The slow loop compensates for thermal drifts whereas the current feedback ensures short term stability.

The light for the trap and the repump beams is amplified by tapered amplifiers (Eagleyard, EYP-TPA-0765-01500-3006-CMT03-0000). The amplifier chips are mounted in a home-built aluminium housing, which we designed to ensure that thermal effects do not alter the position and consequently the injection of the amplifier. The main feature is that the chip is mounted such that any thermal expansion results in a minute rotation around the optical axis rather than a displacement. This rotation preserves the injection of the laser beam in the amplifier chip and ensures constant power output. The temperature of the chip mount is stabilized with two thermo-electric Peltier elements (Eureca Meßtechnik, TEC 1H-30-30-44/80-BS). The chip mount is electrically insulated from the aluminium housing by studs made from PEEK (polyether ether ketone), a plastic with high tensile strength and small mechanical relaxation. The collimation lenses on both sides of the chip are also mounted on holders made from PEEK. The threads on the lens holders are tightly fitted into the aluminium housing; for collimation the holder is simply wound in or out using a wrench. The design of the mount and its thermal behaviour is described in some detail in [Koo07].

The tapered amplifier for the repump light is injected with 8 mW and emits 200 mW. The temperature is stabilized to 31 °C by a temperature controller (Thorlabs, TED 200C). The current through the chip (1.7 A) is supplied by a home-built power supply. The tapered amplifier for the trap light has both temperature and current (2 A) stabilized by a laser controller (Sacher, Pilot 2000). It runs at 25 °C, is injected with 47 mW and emits 767 mW. Both tapered amplifiers only required re-adjustment of the injection when the optical path before the amplifiers changed. The collimation has stayed stable. The coupling efficiency into optical fibres is about 50%.

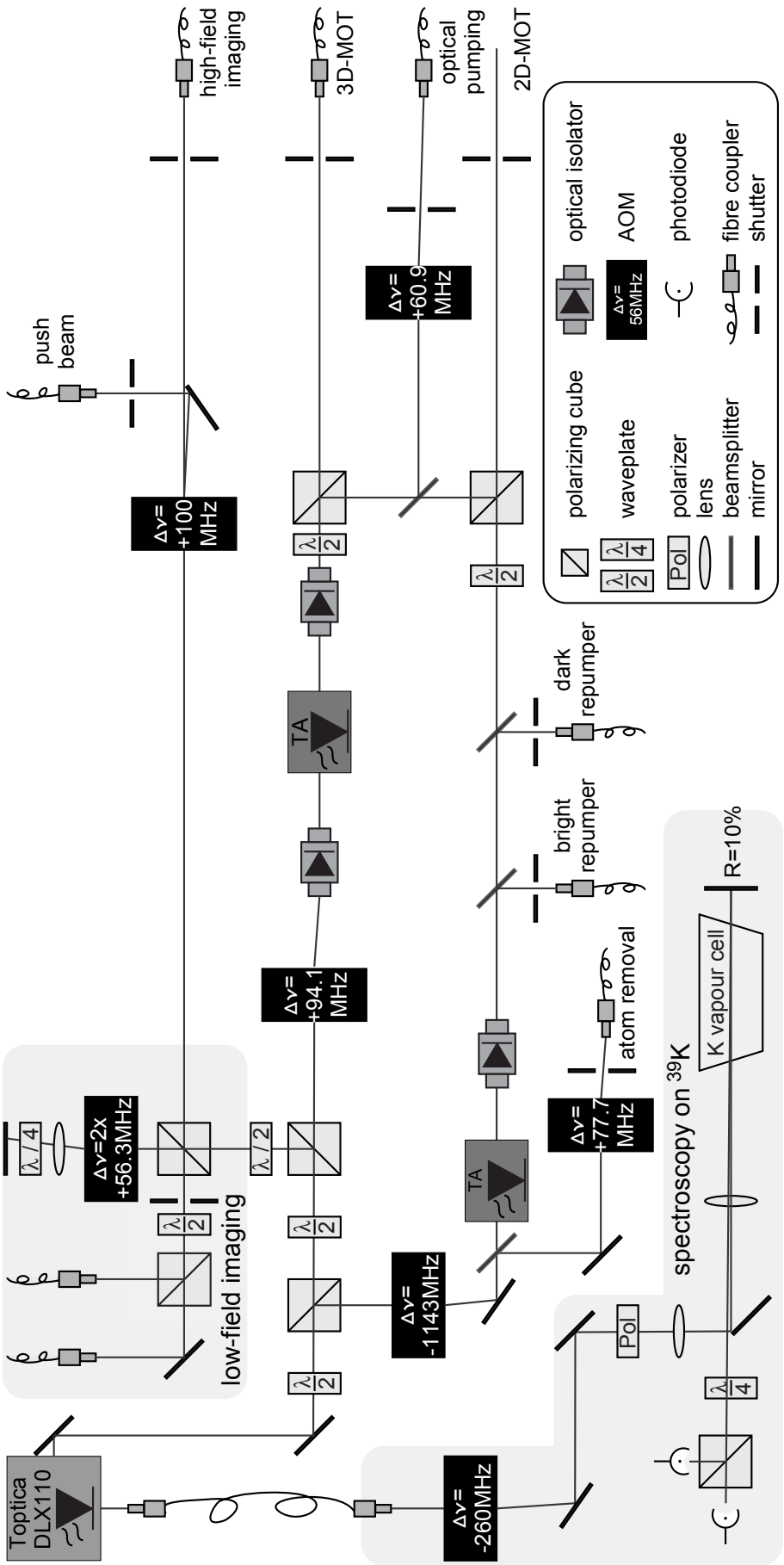

Figure 3.4: Optical setup of the laser system for ^{40}K. The Toptica DLX110 serves as the master laser. Light for the trap and repump transitions is amplified by tapered amplifiers (TA). The spectroscopy setup is located on a separate table. Beam shaping and folding optics have been omitted from this schematic.

3.4 Magneto-optical trapping

In a magneto-optical trap (MOT) neutral atoms are cooled by the absorption and re-emission of light and trapped in a steep magnetic gradient. The cooling mechanism works due to radiation pressure from three orthogonal pairs of counter-propagating beams [Raa87, Met07]. Depending on the number of levels in the atomic spectrum and the lifetimes and transition probabilities of the excited states, several optical transitions need to be driven by light. Successive absorption of light on a so-called cycle transition, enables the cooling. To achieve this in alkalis, two frequencies are needed: a trap (or cool) and a repump frequency. An atom moving towards the light beam is in resonance due to the Doppler effect when the laser frequency is red detuned by several linewidths Γ. Additionally the magnetic field gradient causes a spatially varying Zeeman shift of the transition frequencies and restricts the allowed optical transitions. If the counter-propagating beams have σ^+ and σ^- polarization, a moving atom will always be closer to being resonant with the light beam pushing the atom to the centre of the trap. Effectively the atoms are pushed to the centre of the trap where the magnetic field vanishes [Met99].

For the magneto-optical trapping of ^{40}K the trap laser is red detuned by $6\,\Gamma$ from the $|^2S_{1/2}, F = 9/2\rangle \longrightarrow |^2P_{3/2}, F = 11/2\rangle$ transition. The repump light is detuned by $2\,\Gamma$ from the $|^2S_{1/2}, F = 7/2\rangle \longrightarrow |^2P_{3/2}, F = 9/2\rangle$ transition. The detuning is chosen to be identical for the two- and the three-dimensional MOT (3D-MOT).

3.4.1 Two-dimensional MOT for ^{40}K

As sources for cold atoms, we employ a two-dimensional magneto-optical trap (2D-MOT). A great variety of sources for cold atoms have been developed over the years. For potassium custom-made dispensers are used alone [WI97, DeM99b], or in combination with light-induced atomic desorption (LIAD) [Goz93], as demonstrated in [Kle06] using UV light. The resulting short vacuum lifetimes of using dispensers can be somewhat improved [Moo05, Gri05] but the shortest loading times and highest atom numbers so far have been achieved with beam-loaded MOTs. The highest loading rates for different atomic species have been achieved with a Zeeman slower [Lis99, Slo05, Sta05]. However, the design of a Zeeman slower requires substantial engineering, especially when recycling schemes or multiple species are used.

Compared to a Zeeman slower a 2D-MOT has the advantages that it is a compact setup, it does not allow hot atoms into the main chamber and it makes most efficient use of the atoms. Furthermore there are no stray magnetic fields close to the main MOT. Especially in the case of potassium the high price of enriched potassium is an argument to use a 2D-MOT. The 2D-MOT is a two-dimensional realisation of a MOT. The circularly polarized light beams are applied from four (not six) directions in space and the magnetic gradient is also two-dimensional as shown in Fig. 3.5. The two-dimensional quadrupole field is zero along the symmetry axis. The MOT beams drive cold atoms towards this axis. Along the axial direction there is no confinement by magnetic fields. A push beam is used to push the atoms through the differential pumping tube into the capture region of the 3D-MOT in the centre of the main chamber (see section 3.2). Some designs for 2D-MOTs employ an additional cooling beam

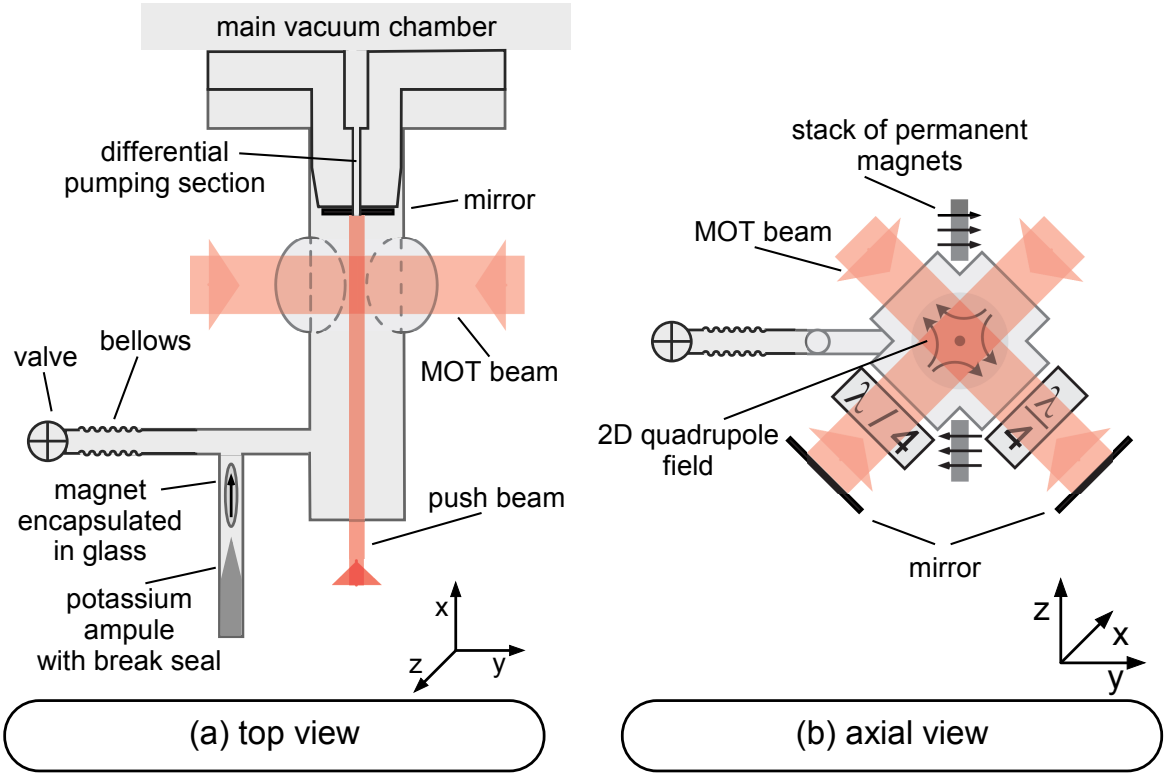

Figure 3.5: Schematics of the 2D-MOT for ^{40}K. The beams are retro-reflected and the magnetic field is formed by stacks of permanent magnets.

opposing the push beam creating a one-dimensional optical molasses [Die98, Cha06, Rid11b]; others are purely two-dimensional [Sch02]. For potassium 2D-MOTs are used in Hamburg [Osp06b], Florence [Cat06] and Paris [Rid11b].

As described in section 3.2 we use two separate 2D-MOTs for the two species, the one for lithium is described in detail in [Tie09b]. Our source for the potassium is a break-seal ampule, which was opened with a glass-encapsulated magnet also included in the glass cell (see Fig. 3.6, Fig. 3.5 and Sec. 3.2). The glass cell of the 2D-MOT is heated to about 50 °C to increase the vapour pressure. Two sets of permanent magnets provide the magnetic quadrupole field. The magnets are made of $Nd_2Fe_{14}B$ (Eclipse magnets, N750-RB) and their magnetisation has been measured to be $8.8(1) \times 10^5$ A/m [Koo07]. Each set consists of two magnets separated by 12 mm. A single magnet has the dimensions $25 \times 10 \times 3$ mm. Effectively the two magnets then form a 62 mm long magnetic dipole. The two magnet sets are each placed 35 mm away from the axis of the cell and together form a radial gradient of 20 G/cm. We use 120 mW trap light and 40 mW repump light per beam. The beams are retro-reflected (see Fig. 3.5) and have a $1/e$-diameter of 18 mm. For an improved loading of the 3D-MOT we employ a push beam, which is aligned along the axis of the 2D-MOT. The push beam consists of 2.6 mW of trap light detuned only by $2\,\Gamma$ from the trap transition. With this 2D-MOT we achieve loading rates in the 3D-MOT of 3×10^8/s. This is over an order of magnitude more than reported from Hamburg [OS06]. Recently the group in Paris [Rid11b] achieved 3D-MOT loading rates of 1.4×10^9/s using larger and more intense 2D-MOT and 3D-MOT beams, and an additional molasses beam in the symmetry axis.

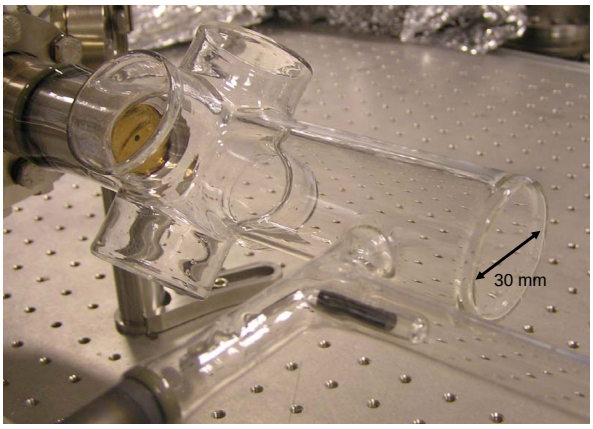

Figure 3.6: The 2D-MOT chamber for ^{40}K is a custom-made glass cell. A side arm leads to the potassium reservoir and a valve. In the foreground the glass-encapsulated magnet, which was used to break the potassium ampule, is visible.

3.4.2 Three-dimensional MOT

The three-dimensional magneto-optical trap (3D-MOT) was designed and optimized as a dual system for lithium and potassium. All waveplates, polarization cubes and mirrors are therefore dichroic. The six 3D-MOT beams, three orthogonal pairs of counter-propagating beams, are all derived from a single beam, which consists of trap and repump light. The beam is split into six using $\lambda/2$ waveplates and polarizing cubes. To produce circular polarization we use quarter waveplates custom-made by Casix for the wavelengths 670 nm and 767 nm. They have a diameter of 18 mm, which is about the $1/e$ diameter of the MOT beams. The trap light has $P = 10$ mW per beam, corresponding to an intensity of $I = 2.3I_s$, where I_s is the saturation intensity (see Appendix A). Although the polarizing cubes are suitable for both the lithium and the potassium wavelengths, the reflection angle differs slightly for the two. When aligning the MOT optics, care has to be taken to minimise the impact of this effect.

For the loading of the MOT we make use of a dark spot MOT [Ket93]. This results in high atom numbers and a high density. For the dark spot MOT the repump light in all the MOT beams is switched off and a separate beam is used. This separate beam of repump light (3.4 mW) is sent through a plate with a dark spot in the middle. The beam is then split into two counter-propagating beams and imaged onto the centre of the MOT. At the center of the MOT the intensity of the repump light is reduced to 2% compared to the intensity in the surrounding area. The image of the dark spot has a diameter of ≈ 3 mm at the center of the MOT. The dark spot is also favourable for the suppression of light-induced collisions between the lithium and potassium when performing experiments on the mixture [Tie09a].

The magnetic quadrupole field for the MOT is produced by the same coils as used for the magnetic trap (for a more detailed description see Sec. 3.5.1), and has a gradient of 14 G/cm. The push beam from the 2D-MOT is directed at the center of trap produced by these coils. This impedes the loading of the 3D-MOT and pushes on the atom cloud. To prevent this and optimize the loading, shim coils produce another few Gauss to shift the atom cloud away from the path of the push beam. The shim coils consist each of several loops of ribbon cable wound around the main vacuum chamber. The

individual wires of the cable are connected in series resulting in 80 windings per coil. There are four shim coils in total: two coils to shift the MOT up or down, positioned around the top MOT coil, and two coils positioned orthogonal to the MOT coils and orthogonal to each other. The shim coils can produce up to 10 G. They are powered by Delta Elektronika (ES030-5) power supplies. The current can be switched quickly to dummy loads using MOSFETs. In 16 s we load up to a total of 2×10^9 atoms in the 3D-MOT. For large atom numbers the temperature of the MOT is $T = 190\,\mu\text{K}$. Sub-Doppler MOT temperatures were reached with ^{40}K by [Cat98, Mod99], but these results concern lower MOT densities.

After the MOT loading the MOT parameters are modified briefly to increase the phase-space density before loading into the magnetic trap. In 10 ms the magnetic field gradient is ramped up to 44 G/cm and the shim coils shift the MOT to optimize the magnetic trap loading. Following this compression stage, the atoms are optically pumped into low-field seeking states. Optical pumping light resonant with the $|^2S_{1/2}, F = 9/2\rangle \longrightarrow |^2P_{3/2}, F = 9/2\rangle$ transition is applied to the atoms for 60 µs at an intensity of about $1.4I_s$. During the optical pumping step, repump light from all six directions prevents population of the $|^2S_{1/2}, F = 7/2\rangle$ manifold. The bright repump light has $P = 1.5\,\text{mW}$ per beam, corresponding to an intensity of $I = 0.3I_s$ and is not attenuated by a dark spot in the centre.

An offset field of 3.6 G along the direction of the optical pumping beam is provided by one of the shim coils. The optical pumping has been optimized to achieve a mixture of atoms in the $F = 9/2, m_F = 9/2, 7/2$ and $5/2$ states. About 60% of the atoms in the MOT are then recaptured in the magnetic trap. A higher efficiency can be achieved [Tie09a], but this yields much more atoms in the fully-streched state $m_F = 9/2$. However, to achieve thermalization in the magnetic trap, a mixture of atoms in different spin states is necessary.

3.5 Optically plugged magnetic trap

For the magnetic trapping we employ an optically plugged magnetic trap. It is a combination of a magnetic field supplied by two coils and a blue-detuned laser focused in the center of the magnetic trap as an optical plug. The coils create a linear quadrupole trap with zero magnetic field at the centre. Near the zero crossing of the magnetic field the atoms can undergo spin-flips to untrapped states and be lost from the trap. These so-called Majorana losses [Maj32] become more pronounced the colder and therefore closer to the trap centre the atoms get. The dipole force exerted by the blue detuned laser repels the atoms from the centre of the trap and prevents Majorana losses. This method has been used to produce the first Bose-Einstein condensate at MIT in 1995 [Dav95a]. The idea of the optical plug was later abandoned in favour of magnetic traps with an offset field. The advantage of the optically plugged trap is that it allows to make use of a linear trap with its favourable evaporation properties and it saves space, which would be needed for an additional coil or Ioffe bars to produce the offset field. When evaporating in a linear trap the volume decreases faster than in a harmonic trap, thus increasing the phase space density faster [Bag87, Dav95b]. Only recently other groups have started again employing an optically plugged trap to produce large Bose-Einstein condensates [Nai05, Heo11] or ultracold Fermi clouds [Wu11].

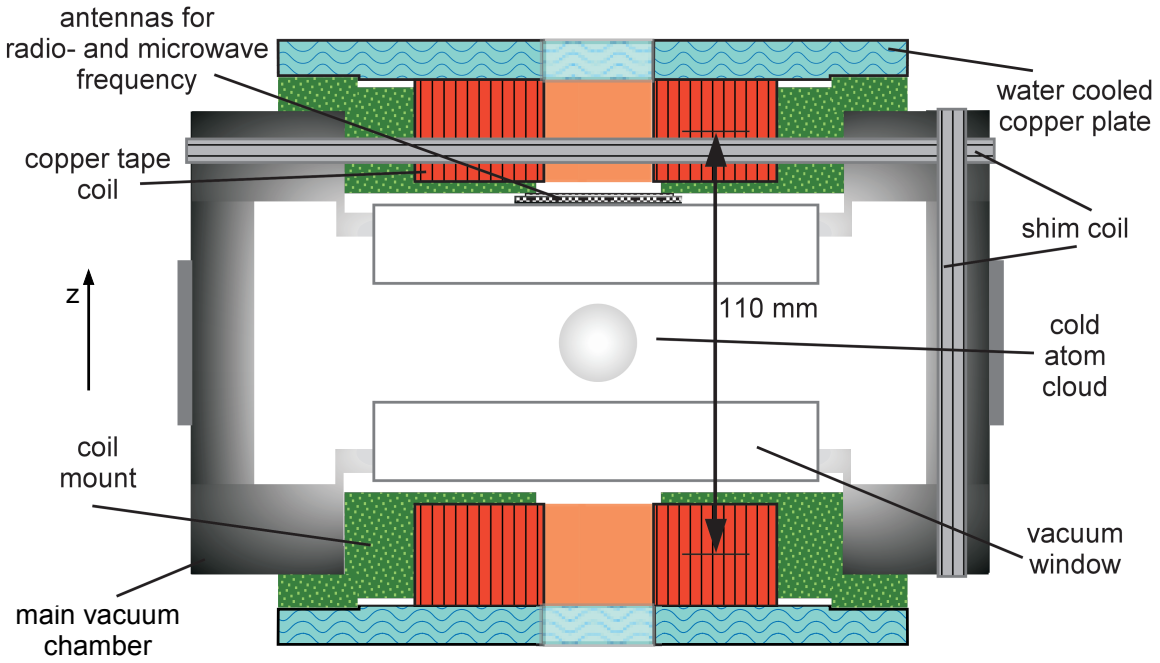

Figure 3.7: Schematic of the cut through the vacuum chamber showing the MOT coils and the water-cooling. The shim coils are wound around the main chamber and are used as trim coils for the MOT loading and optical pumping. Only two of the four shim coils are shown in the schematic. The antennas consist of simple wire loops.

3.5.1 Magnetic trap

The magnetic trap is formed by the two MOT coils with their centres separated by about 110 mm. The coils are developed for the use in loudspeakers and fabricated out of a Kapton insulated copper tape (Canatron, CT 7419). The copper tape has a 25×0.25 mm cross-section and Kapton insulation on both sides. Each coil has 76 windings resulting in a coil with 45 mm outer radius and 17.5 mm inner radius. The coils are glued to slit copper plates, which are water-cooled. The copper tape ensures a high current density. With a current of 100 A a magnetic gradient of $B' = 176\,\mathrm{G/cm}$ along the z-direction is created. The absolute value of the magnetic field is $B(x, y, z) = (B'/2)\sqrt{x^2 + y^2 + 4z^2}$. The symmetry axis is in z-direction as indicated in Figs. 3.7 and 3.2. The inductance of the coils is 365 µH. Each coil is mounted close to the CF150 windows protruding into the main chamber.

The magnetic field has to be switched off entirely by the time an image of the atoms is taken. Residual fields would shift the resonance frequency of the atoms and distort the number of detected atoms. According to Faraday's law fast switching of magnetic fields induces a high voltage, which can drive an induced current creating a magnetic field opposing the initial one. To prevent this a special switch is employed. The switch was constructed following the example of [Aub05], described in detail in [Stu04]. In one switch box several features are included: four IGBT switches (Semikron, SKM100GB123D) disconnect the coils from the power supply within 600 ns. The induced voltage spike is absorbed by stacks of transient voltage suppressor diodes (TVS, ST SM15T39A). A current of 100 A then switches off within 100 µs.

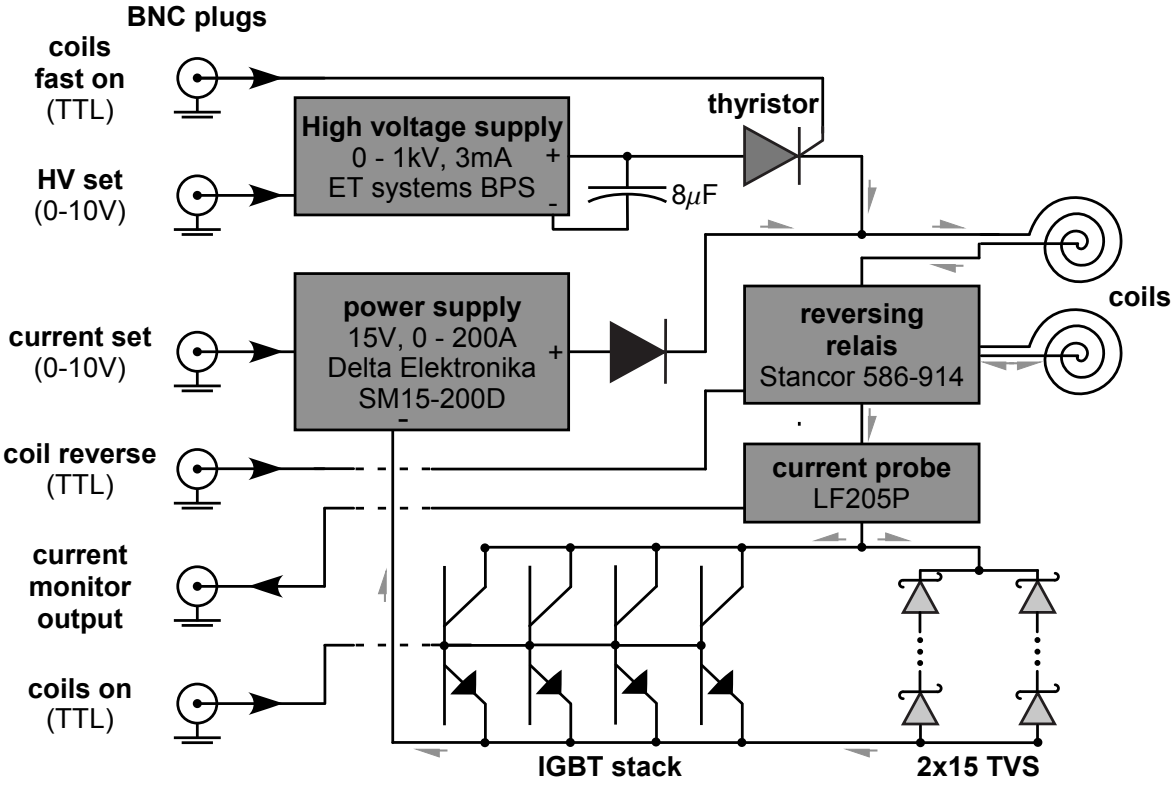

Figure 3.8: Simplified circuit diagram of the MOT coil switch. The grey arrows indicate the direction of the current. Analogue and TTL signals control the various functions of the switch. Apart from optical decouplers, insulators and other means to protect the involved parts, also the filters to prevent ringing of the current after switch on have been omitted in this schematic.

For a fast switch-on to a high current a pre-charged capacitor (8 µF) is switched into the circuit with a thyristor (CS35/1200). The switch-on time is limited by a filter to 50 A/µs to protect the thyristor. The switch box also includes two relays (Stancor, 586-914), which allow to change between a gradient and a homogeneous field. All operations of the switch box are controlled by analogue signals (0-10 V) and TTL pulses. The steering signals are decoupled by insulation amplifiers from the control circuit to protect the computer control from high voltages. For a simplified schematic see Fig. 3.8.

However using tape to make a coil has two major flaws: a thermal gradient within the coil, with the thereby caused magnetic inhomogeneities and instabilities, and eddy currents within the tape. The coil is only cooled from one side, resulting in a thermal gradient from top to bottom. This gradient gives rise to a gradient in resistance and therefore in current density in each winding. The stability of the magnetic field in strength and position is limited by the thermalization of the coils. In particular the position of the magnetic field zero with respect to the position of the optical plug depends on an identical rate of thermalization for both coils, which cannot be assumed. It is difficult to achieve optimal thermal contact between coil and cooling plate. The Kapton insulation of the tape is not coated onto the copper but attached in the form of a 50 µm thick adhesive tape. The Kapton tape protrudes on the top and bottom

of the coil. We have improved this by milling off the Kapton and placing 0.2 mm thick electric insulation pads between cooling plate and the coils. The thick pads were necessary because the contact surface is not entirely flat. However, the insulation limits the thermal conductance between the coils and cooling plates.

The heating of the MOT coils results in a decreased atom number if the coils run for longer than usual (for example when measuring the lifetime in the magnetic trap). For a normal experimental cycle where the atoms are transferred from the magnetic trap to the dipole trap after 23 s and a new measurement starts about every minute, the temperature varies about 8 °C. When running 100 A through the coils, they heat up by about 35 °C within 2 minutes. In addition the tape coils have the disadvantage that the switching-off induces eddy currents within the copper tape of the coils, which can persist for a couple of milliseconds. The current only produces a small field, orthogonal to the dipole created by the coil itself. In practice a shift of the resonance frequency for the imaging is not noticeable any longer after 2 ms time-of-flight. We do not recommend the use of copper tape with a large aspect ratio for coils in a magnetic trap.

3.5.2 Optical plug

The coils create a linear quadrupole trap with zero magnetic field at the centre. To prevent Majorana losses at the zero-crossing we focus 9 W of 532 nm laser light as an optical plug in the centre of the trap. It is essential that the beam profile of the plug laser is a Gaussian transverse electro-magnetic mode (TEM_{00}). Dust on the optics or thermal lensing in an AOM can lead to a doughnut shaped mode (TEM_{01}), which makes the optical plug less efficient. To avoid this problem we have replaced the AOM, which was initially used to switch off the plug, by a high power shutter (nmLaser Products Inc., LST4WBK2-D123). The shutter does not close sufficiently fast to be able to image the cloud in the main chamber after release from the magnetic trap. For alignment purposes it is best to leave the plug switched-on during time of flight. The imaging of the atoms then allows for qualitative measurements. All quantitative measurements are done releasing the atoms from the optical dipole trap with the optical plug switched off.

As illustrated in Fig. 3.9 the beam mode and focus shape is monitored with a CCD camera placed in the focus of the reflection from the beamsplitter which combines the optical plug and the optical dipole trap just in front of the vacuum chamber. The passage through the beamsplitter introduces astigmatism to the plug beam profile, displacing the two foci by about 2.2 mm. The average waist of the beam is $w = 16\,\mu m$. The light for this optical plug is provided by a 10 W Verdi (Coherent).

When running a high current through the MOT coils for times longer than 30 s, for instance when measuring the vacuum lifetime in the main chamber, the coils heat up noticeably and this affects the number of trapped atoms. This can be attributed to the thermalization of the coils. When heating up, the position of the magnetic field zero changes such that the alignment of the optical plug is not optimal any more and Majorana losses are not sufficiently suppressed. The alignment of the plug beam itself is stable, we only have to adjust it every 4–6 weeks during normal operation.

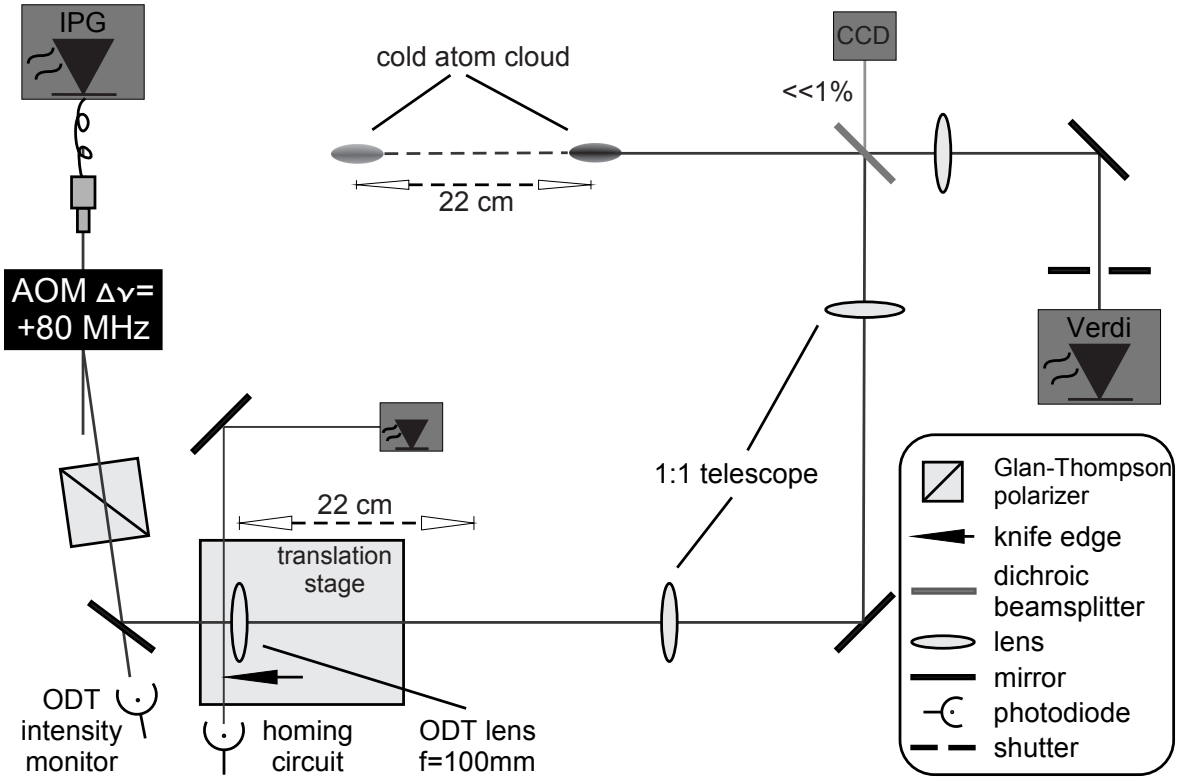

Figure 3.9: A dichroic beamsplitter combines the optical plug and optical trap beams. A small percentage of the plug light is reflected on a CCD camera to detect the beam quality and the focal size. The position of the translation stage is controlled using an additional laser. The polarization of the light is normal to the plane of this figure.

3.6 Optical dipole trap

The cold atom cloud is loaded into an optical dipole trap (ODT) and transported into the science cell by moving the focus of the trap. The cold atoms are transferred from the magnetic trap after the evaporation (see Sec. 4.1 for more details). In an optical dipole trap (ODT) the dipole force exerted by the laser light on the atoms is directed to regions of high intensity if the light is red-detuned to the atomic transitions [Ash70, Chu86]. The dipole force depends on the intensity and detuning as described in Appendix A and is identical for all hyperfine states.

The light for the ODT is provided by a 1065 nm fibre laser (YLD-5-LP, IPG Photonics). The intensity noise $\Delta I/I$ of the fibre laser is at its lowest when the laser is set to high output powers (5 W). Therefore we do not control the trap depth via the output power of the fibre laser but with a high-power AOM (Crystal Technology, 3080-197) set to 80 MHz. The AOM shows no signs of drift or heating. The ODT is formed by focussing up to 1.62 W of laser light[†] to a waist of $w_0 = 20\,\mu\text{m}$. The resulting trapping potential has, according to the expression A.9 in Appendix A, a maximum depth of 345 µK for ^{40}K. At full beam power the harmonic trapping frequencies are, according to Eq. A.12, $\omega_r = 2\pi \times 4.27$ kHz in the radial and $\omega_a = 2\pi \times 51$ Hz in the axial direction.

[†]The power of the beam is 1.9 W before passing four more optical elements. Assuming 4 % loss at each surface results in 1.62 W laser power in the chamber.

As illustrated in Fig. 3.9, we transport the cold non-degenerate cloud of atoms by means of optical tweezers to the science cell. This method has first been used by [Gus01]. A $f = 100\,\mathrm{mm}$ lens, producing the focus for the ODT, is mounted on a linear air-borne translation stage (Leuven Air Bearings, LAB-LS). The translation stage is moved by a geared DC motor (Maxon Motor, 118751) via a grooved belt. The motor is steered by a motion controller (Maxon Epos 24/5) that gets its commands from an encoder (HEDL5540). The focussing lens ($f = 100\,\mathrm{mm}$) can be moved over 22 cm with the translation stage. A 1:1 telescope installed behind the focussing lens images the focus to its position in the vacuum chamber. The telescope preserves both the numerical aperture and the focus shape during the transport to ensure constant trapping frequencies.

The starting position of the translation stage is kept constant by a feedback loop using the power level on a photodiode as input. A laser beam is aligned on a knife edge positioned on the translation stage. The power of the light passing the knife edge is measured using the photodiode. As soon as the stage reaches its homing position, the motor is stopped. The reproducibility of the focus position after the transport is $\sigma_r = 1\,\mu\mathrm{m}$ in the radial and $\sigma_a = 40\,\mu\mathrm{m}$ in the axial direction [Tie09a]. Both deviations are much smaller than the typical diameter of the cloud in radial ($d_r \approx 10\,\mu\mathrm{m}$) and axial ($d_a \approx 1\,\mathrm{mm}$) direction. When transporting the cold atom cloud to the science cell and back, the atom number is not reduced within the experimental error for the typical vacuum lifetime of 40 s. We transport a thermal cloud in the 345 µK deep ODT and do not detect significant heating due to the transport.

Just before entering the main chamber the dipole trap beam is overlapped with the optical plug beam using a dichroic beamsplitter (CVI laser, BSR-15-1940) as shown in Fig. 3.9. The dipole trap beam is reflected by the beamsplitter, so the focus is not influenced by the beamsplitter contrary to the optical plug. This ensures a uniform trapping frequency in the radial direction. To increase the trap depth allowing for higher atom numbers we plan to include another laser to form a crossed-dipole trap in the science cell.

3.6.1 Intensity stabilization of the fibre laser

Intensity fluctuations of the ODT laser lead to heating and loss of trapped atoms [Sav97]. The heating and subsequent atom loss is most severe when reaching low trap depths [Geh98]. When evaporating the cold atom cloud by lowering the trap depth, high atomic densities can not be reached reproducibly if the intensity of the dipole trap is fluctuating. When evaporating from the optical trap (see Sec. 4.1), we lower the power typically down to 5% of the full power. An intensity stabilization for the dipole trap has to have a large enough dynamic range to be still effective at low intensities. Additionally, an AOM has non-linear deflection efficiency. The deflected optical power increases logarithmically with the driving radio-frequency. When optimizing evaporation ramps, a linear response of the output power to the control signal is convenient.

At full laser power the noise spectrum of the fibre laser shows peaks of 10 dBm at 100 Hz and 300 Hz, we detected no other noise peaks up to the detector limit of 3.5 GHz. To realize an intensity stabilization with a feedback loop we detect light of the fibre laser leaking through a mirror in its path (see Fig. 3.9). This mirror has to be chosen

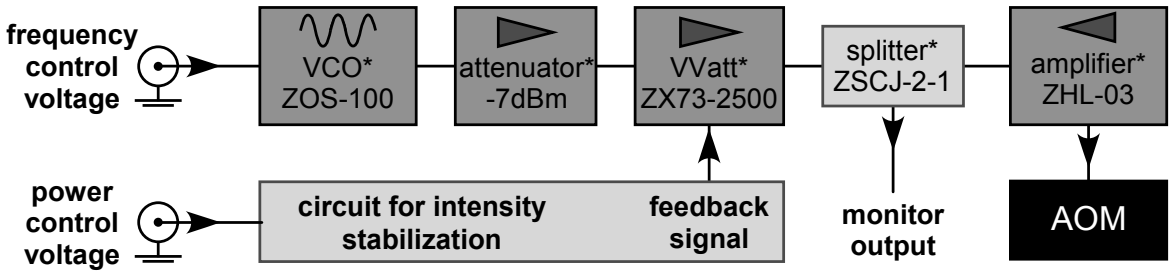

Figure 3.10: Schematic of the components used to control the diffraction power and frequency of the AOM for the ODT. The circuit for the intensity stabilization is shown in Fig. 3.11. All parts marked with * are manufactured by Mini-Circuits.

with care: the main polarization leaking through the mirror has to match the desired polarization of the dipole trap, otherwise the feedback will even increase intensity noise as it stabilizes on the minority polarization. The polarization leaking through a mirror depends on its orientation relative to the beam and its polarization [Hec90]. Although the light from the fibre laser is linearly polarized, the AOM and mirrors (not all shown in Fig. 3.9) modify the polarizations of the beam [Ekl75]. A Glan-Thompson polarizer (Thorlabs, GTH10/M) with a high extinction ratio (10^5:1) in the beam path after the AOM filters out the minority polarization. The light leaking through the sampling mirror is detected with a high speed photodiode (Thorlabs, DET110) with 20 ns rise time. The signal of the photodiode is compared to a reference voltage (*power control voltage* in Figs. 3.10 and 3.11) with a differential amplifier. The difference signal is integrated, rectified and amplified with a logarithmic amplifier as depicted in Fig. 3.11.[‡] The circuit contains several potentiometers and fixed value resistors, which need to be set depending on the specific rf-amplifier and AOM used. These resistors ensure the linear response of the optical power deflected by the AOM to the power control voltage supplied by the main experiment control.

As illustrated in Fig. 3.10, the frequency for the AOM is set by a voltage controlled oscillator (VCO) (Mini-Circuits, ZOS-100) attenuated by 7 dB. We use the AOM at a fixed frequency of 80 MHz. The rf-amplification circuit for the AOM was set up using a ZX73-2500 (Mini-Circuits) voltage variable attenuator (VVatt). The output of the VVatt is split into two (Mini-Circuits, ZSCJ2-2-1), one half of the signal is used as a monitor output and the other is amplified by a ZHL-03 (Mini-Circuits) amplifier and sent to the AOM. The output power of the VVatt is controlled by the feedback signal generated by the intensity stabilization circuit.

In the intensity stabilization circuit in Fig. 3.11 the analogue and manual switches and an additional amplification of the power control voltage allow for an operation of the AOM without the stabilization. The analogue switches (AD7512DIJ) are controlled by triggers from the main experiment control (see Sec. 3.9). Monitor outputs give out the photodiode signal, the error signal and the feedback signal controlling the radio frequency power going to the AOM. Followers (not shown in Fig. 3.11) built with LF353 amplifiers provide buffered output for the monitor signals. All other amplifiers used for the circuit are of the type AD844AN. The whole circuit has been constructed such that ground loops and radio frequency noise from other equipment have minimal influence.

[‡]We acknowledge support from the group of I. Bloch for details of the electronics design.

To protect the radio frequency amplifier from damage a load detector (not shown in 3.11) allows an output to the amplifier only when an AOM is connected.

To test the intensity stabilization we modulated the output power of a test laser diode at different frequencies and measured the attenuation of the modulation of the optical output power due to the lock. Up to 300 Hz the modulation is attenuated by 25 dB. That is sufficient to reduce the intensity noise of the fibre laser. When testing the lock with the fibre laser, we do not detect any noise peaks. The white noise of the fibre laser is reduced by 10 dB by the lock.

3.7 Feshbach coils

In the field of cold atoms Feshbach resonances have proven to be a powerful tool to manipulate atoms and vary their interaction strength. To make use of Feshbach resonances the magnetic field has to be set to values where the resonances occur. The position and widths of the Feshbach resonances differ for the different atomic species used, so the requirements on stability, homogeneity and strength of the magnetic field are different for each system. For the ^{6}Li- ^{40}K case, first experiments and calculations [Wil08, Tie10b] showed that many of the Feshbach resonances are located below 500 G and are narrower than 1 G. High precision, stability and homogeneity of the magnetic field over the whole sample of cold atoms is thus required to be able to make use of these Feshbach resonances.

To achieve high homogeneity, the coils for the Feshbach field are arranged in Helmholtz configuration. Both coils are wound on a mount manufactured from a single piece of brass to ensure and maintain the correct distance of the coils. The outer diameter of the coils is 158 mm. The brass housing is slit to prevent eddy currents. The slit itself has been refilled using glass-fibre. The brass mount is water-cooled and its overall volume is minimised to prevent eddy currents and provide good optical access. To ensure high field homogeneity and thermal stability we chose to employ many windings per coil and relatively little current. Each coil has 126 windings and is made of copper wire (Romal bv) with a rectangular (3×2 mm) cross-section. The different layers of the coil are then easier to position during the winding procedure. The rectangular cross-section also increases the overall current density j and homogeneity compared to a wire with circular cross-section. The two coils are identical except for the helicity of corresponding layers.

Around the origin of the two coils, where the cold atoms are located, the overall current density is then antisymmetric:

$$\vec{j}(\vec{r}) = -\vec{j}(-\vec{r})$$

Deviations from perfect homogeneity around the origin due to finite size effects, the changing of layers of the wire and the leads to the coils cancel each other in all odd orders. The windings of the coil proceed around the mount as a true helix. The transitions between layers do not occur stepwise but continuously over a whole winding. Spacers made from glass-fibre ensure the correct positioning of the individual windings and the coil is glued with epoxy (Stycast, 1266). The design and construction of the Feshbach coils is described in more detail in [Tie09a].

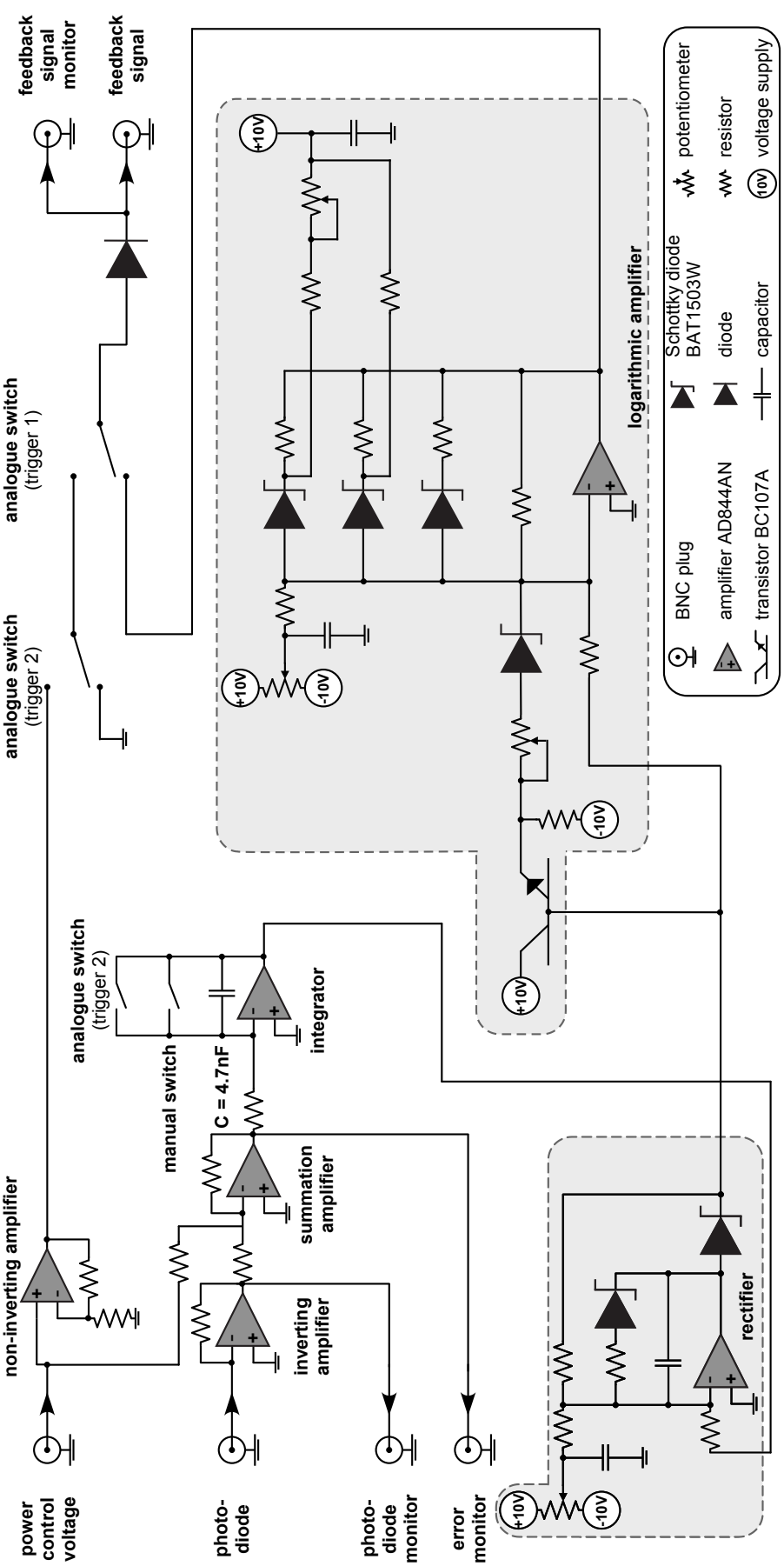

Figure 3.11: Simplified schematic of the circuit for the stabilization of the ODT intensity. Not shown are the load detector, the stabilized power supplies, followers for the output signals and various filters. The potentiometers and in certain circumstances other resistors need to be adapted to the specific combination of the rf-amplifier used for the AOM and the AOM to ensure an overall linear response.

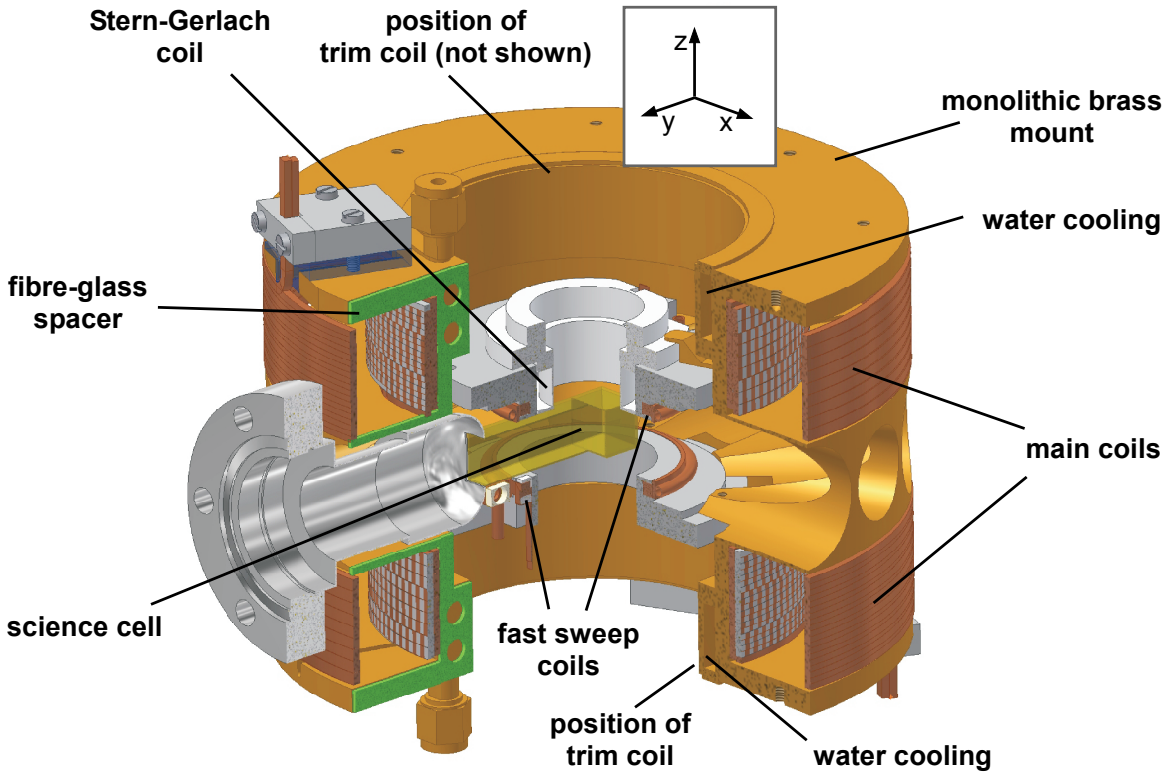

Figure 3.12: Schematic of the Feshbach coils and the additional coils for fast sweeps and Stern-Gerlach experiments. The position of the trim coils is indicated, the coils are omitted from the schematic. The mount is made of a single piece of brass and is water-cooled. Holes drilled in the mount offer good optical access to the science cell in the middle.

Mounted inside the Feshbach coils are coils to allow for fast sweeps, coils to trim residual field curvatures and a coil to apply a gradient for Stern-Gerlach experiments. The fast sweep coils have a diameter of 21 mm, and 10 windings. The used copper foil (Alphacore, Laminax B-series) has a 3.175×0.254 mm cross-section and a 25.4 µm thick Kapton insulation coated onto one side. The fast sweep coils are mounted in Helmholtz configuration around the science cell. Like the Feshbach coils these coils are set up in an antisymmetric way. The trim coils have a diameter of 74 mm, 15 windings, and they are glued 50 mm from the centre (see Fig. 3.12). The copper wire has a diameter of 1 mm. The coil for the Stern-Gerlach experiments (see 4.4) is located about 1 cm away from the centre of the science cell, has 56 windings, a radius of 15.5 mm and a wire diameter of 0.5 mm. The Stern-Gerlach coil is glued with epoxy (Stycast, 1266) and has a 10 kΩ temperature resistor (RS, 484-0149) attached to it.

The magnetic field homogeneity was determined using a XEN-1200 field probe with a resolution of 3.5 mG up to 100 G. The remaining inhomogeneities were fitted to a polynomial expansion in the z-direction (for more details see [Tie09a]). The main coils have an inhomogeneity in the first order of $B'/B_0 = 1.5 \times 10^{-6}$/mm, the relative overall homogeneity is better than 10^{-5}. The fast sweep coils are in first order less homogeneous ($B'/B_0 = 4 \times 10^{-4}$/mm) than the big coils. However, considering the low fields in the sweep coils, the absolute homogeneity of the two coils is comparable.

The thermal stability of the Feshbach coils has been simulated and the maximum temperature of the coils has been measured to fluctuate less than 0.1 °C within two hours [Tie09a]. The fluctuation is determined by the drift of the cooling water temperature in the laboratory.

Apart from a high field stability and homogeneity the Feshbach coils also have to allow for fast sweeping and switching of the field to be able to manipulate the atoms. The main Feshbach coils are powered by a Danfysik (Model 858) power supply. The power supply is specified to a stability of ±1 ppm for 30 min. It delivers up to 25 A. The programming via RS232 is limited to 2 A/s (≈ 35 G/s). To shorten the time the field in the Feshbach coils takes for switch-on and -off, we employ a switch and a dummy resistor. At the beginning of each experimental cycle (described in detail in Chapter 4), the current is programmed to the desired value and switched to run through a resistive load, matched to the resistance of the Feshbach coils. The ≈ 50 s, which elapse during the experimental cycle until the Feshbach coils are needed, are sufficient to stabilize the current running through the dummy load. At the beginning of the Feshbach experiment two MOSFETs (BUZ 344) switch from the dummy load to the Feshbach coils. The current through the coils then reaches its set value within a few hundred milliseconds (see Sec. 4.3). For a fast switch-off, the MOSFETs switch back to the dummy load while transient voltage suppressors absorb the induced voltage spike. Once the current is running through the dummy load again, the power supply is programmed to zero current output.

The fast sweep coils are powered by a Delta Elektronika (ES075-2) supply. Combined with a homebuilt transistor regulation, linear sweeps up to 40 G/ms with a field stability of less than 10^{-5} can be achieved.

3.8 Imaging systems

The means to detect the number of atoms and their temperature and distribution is imaging. We employ three different methods: fluorescence imaging at low field and absorption imaging in low and high field. The imaging is done by detecting the (near) resonant light on a CCD camera.

3.8.1 Cameras and optical setup

As shown in Fig. 3.13 four cameras in total are used for the imaging. Two of these (Sony, SX90) are used for the separate imaging of lithium and potassium and can image on the horizontal axis both in the science cell and in the main chamber. The lenses for the two horizontal imaging paths are on flippable mounts to switch between the two imaging positions. The other two cameras provide images in the vertical direction in the main chamber (Sony, X710) and the science cell (Apogee, U13). The effective pixel size at the location of the atomic sample has been calibrated for all cameras as described in [Tie09a]. The effective pixel sizes at the sample of the Sony (SX90) cameras including the telescopes are 3.60 µm when imaging in the science cell and 3.67 µm when imaging in the main chamber. The time elapsing between taking the absorption and the reference image is limited by the readout time. For the Sony cameras this takes 500 ms. The Apogee has an effective pixel size of 3.94 µm when using a ×4 microscope

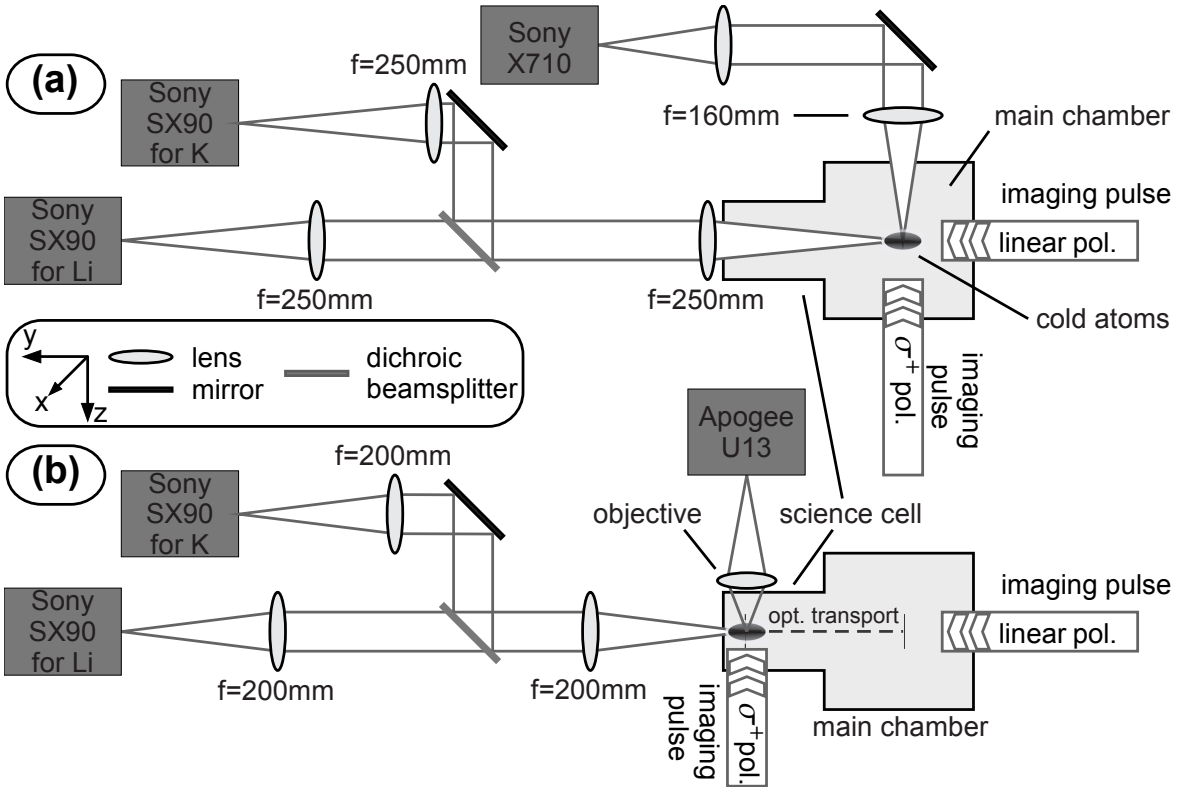

Figure 3.13: Schematic of the imaging systems in (a) the main chamber and (b) the science cell. The lenses with f=200 and 250 mm can be flipped in and out of the optical path. For the vertical imaging with the Apogee camera in the science cell a $\times 4$ microscope objective is used.

objective (Edmund Optics, NT36-131). The Apogee camera is used in fast kinetics mode achieving time delays between taking two images down to 3 ms.

In the science cell the vertical imaging offers excellent optical access and can reach a high resolution. In a test setup it has been shown [Tie09a] that we can achieve a high resolution for the vertical imaging in the science cell. The upper limit for the imaging resolution is $\approx 3\,\mu$m for a single point source. However the optical density is always highest when imaging along the axis of the optical dipole trap. Most of the experimental data presented in this thesis was obtained using images of the cold atom cloud taken along the horizontal axis. The vertical imaging in the main chamber is mostly used for alignment and to optimize the dipole trap loading.

The resonant imaging light is derived from the master laser by a double-pass through an AOM (see Fig. 3.4) and split into two beams which are each coupled into polarization maintaining fibres (Schäfter + Kirchhoff, PMC-630-4.5NA011-3-APC). With dichroic beamsplitters the imaging light for lithium is combined with the light for potassium (not shown in Fig. 3.4). The output of the first fibre is used for the imaging in horizontal direction. The light is linearly polarized. The second fibre can be connected either to a collimator at the science cell or at the main chamber. This light is used for the imaging in vertical direction and is σ^+ polarized by a waveplate. The circular polarized light can be used for imaging both in low and high magnetic field. The linear polarization is only used for low field imaging.

3.8.2 Fluorescence imaging

For florescence imaging in the main chamber we irradiate the atoms with near resonant light using the MOT beams and the light scatters in all directions. The MOT beams are under an angle to the imaging path, so only scattered photons and no photons of the MOT beams are detected by the CCD camera. A trapped atom in the MOT can scatter many photons without being lost from the trap. This allows for long exposure times of the camera and thus a good signal to noise ratio. This imaging method is used to characterise the MOT, the magnetic trap and to optimize the magnetic trap capture efficiency. We only used it for relative measurements, which do not require calibration of the signal. The characterization of the lithium 2D-MOT-source in [Tie09b] was also done using fluorescence imaging.

3.8.3 Absorption imaging

For absorption imaging a low intensity resonant light pulse passes through the cloud of atoms onto the camera. In areas where there are atoms, the light is absorbed and the image shows a shadow of the atomic sample. In this thesis all absorption images were taken after release of the atoms from a trap after variable times of expansion. In ballistic expansion only a few photons can be scattered per atom as atomic motion and photon recoil can blur the image. In addition to the resonant light a pulse of repump light is switched on when imaging to prevent a population of dark states. In the main chamber the repump light is part of the MOT beams, therefore under a 45° angle to the imaging beam and in two counter-propagating beams. In the science cell the repump light is back reflected and under an angle of $\approx 30°$ to the imaging path. During the imaging pulse the atoms absorb photons from the imaging beam and re-scatter them in all directions. For a resonant light pulse of duration Δt with low intensity, i.e. the saturation parameter $s_0 = I/I_s \ll 1$, the number of photons N_p scattered is given by $N_p = \frac{1}{2} s_0 \Gamma \Delta t$, with Γ being the natural linewidth of the optical transition [Met99]. The recoil from the absorbed photons shifts the atoms out of resonance due to the Doppler effect. The frequency shift is given by $\omega_D = v_{\mathrm{rec}} k N_p$, with the wavevector k of the light and the recoil velocity $v_{\mathrm{rec}} = \hbar k/m$. The re-emission moves the atoms in random directions resulting in a blurring of the cloud's image. The atoms are then on average displaced in the transverse direction by $r_{\mathrm{rms}} = v_{\mathrm{rec}} \Delta t \sqrt{N_p/3}$ [Jof93]. For potassium we use intensities for the imaging pulses with saturation parameter $s_0 = 0.4$ and a pulse length of $\Delta t = 100\,\mu\mathrm{s}$, resulting in a displacement by $r_{\mathrm{rms}} = 9\,\mu\mathrm{m}$ and a frequency shift of $\omega_D = 0.4\Gamma$.

To obtain a signal from the CCD camera three images need to be recorded. After every absorption image taken with intensity I_{abs}, two images of the optical field are taken. One as a reference with imaging light I_{ref} and one without imaging light with intensity I_{bg} as background. The signal is then: $I(x,y)/I_0(x,y) = (I_{\mathrm{abs}} - I_{\mathrm{bg}})/(I_{\mathrm{ref}} - I_{\mathrm{bg}})$. For the Sony cameras we found that the background image I_{bg} can be neglected, and it is not used in the analysis of the data. The intensity distribution is used to calculate the column density of the atomic distribution using the Lambert-Beer law:

$$\frac{I(x,y)}{I_0(x,y)} = \exp(-OD) = \exp(-\sigma n(x,y)),$$

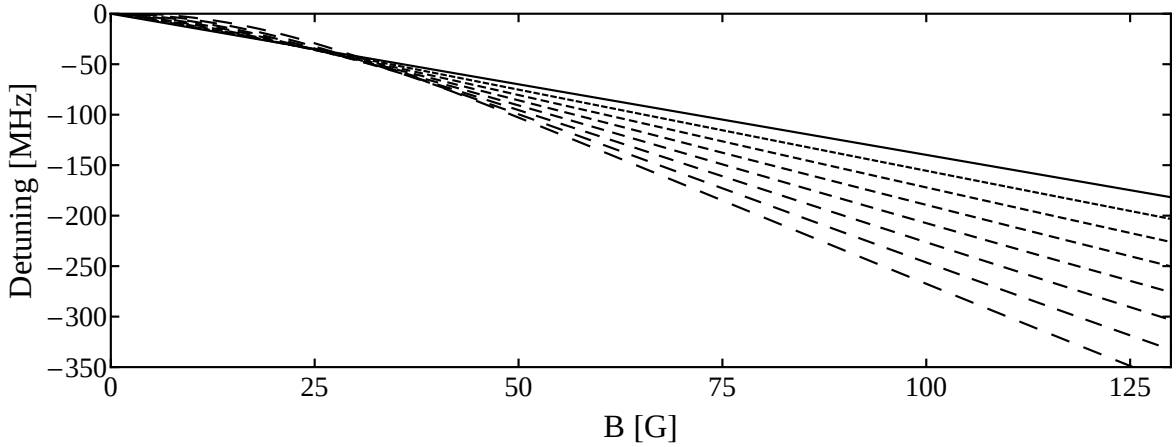

Figure 3.14: With rising magnetic field the detuning from the zero field imaging transition $|^2S_{1/2}, F = 9/2\rangle \rightarrow |^2P_{3/2}, F = 11/2\rangle$ changes. Shown are the frequencies for σ^- transitions $m_F = -9/2 \rightarrow m'_F = -11/2$ (full line) to $m_F = 5/2 \rightarrow m'_F = 3/2$ (long dashes). For magnetic fields higher than 55 G, the different transitions are separated by more than the linewidth Γ and the m_F states can be imaged individually.

with the optical density OD, the column density along the imaging beam axis $n(x, y) = \int dz n(x, y, z)$ and the atomic absorption cross-section of the atoms

$$\sigma = \kappa \frac{3\lambda^2}{2\pi} \frac{1}{1 + (2\delta/\Gamma)^2}.$$

Here δ is the detuning from the atomic resonance and κ a transition dependent coefficient. For the transition $|^2S_{1/2}, F = 9/2\rangle \longrightarrow |^2P_{3/2}, F = 11/2\rangle$ and linear polarized light $\kappa = 2/5$, for circular polarized it is $\kappa = 1$ [Tie09a].

3.8.4 High-field imaging

The ability to image in high field is vital if switching-off times of the magnetic fields are slower than the dynamics of the cold atom cloud. Atoms can be lost from the cloud or become invisible to the imaging light under conditions where molecules are formed as a result of sweeping through a Feshbach resonance during the switch-off. In non-zero magnetic field the different Zeeman states are not described by just one set of quantum numbers but by a combination of different sets. Transitions which are closed transitions at zero field cease to be closed at higher magnetic fields. In addition, the transition probabilities change with magnetic field. The imaging transitions have to be chosen carefully depending on the specific magnetic field and the state which has to be imaged. The transition probabilities of ^{40}K in dependence of the magnetic field are described in more detail in C.2. For atoms in the states $|^2S_{1/2}, F = 9/2, m_F = -9/2, \cdots, 5/2\rangle$ σ^- transitions to the states $|^2P_{3/2}, F' = 11/2, m'_F = -11/2, \cdots, 3/2\rangle$[§] are allowed. As shown in Fig. 3.14 with rising magnetic field the atomic transition frequencies change by a considerable amount.

[§]For convenience the low-field labelling of the states is used.

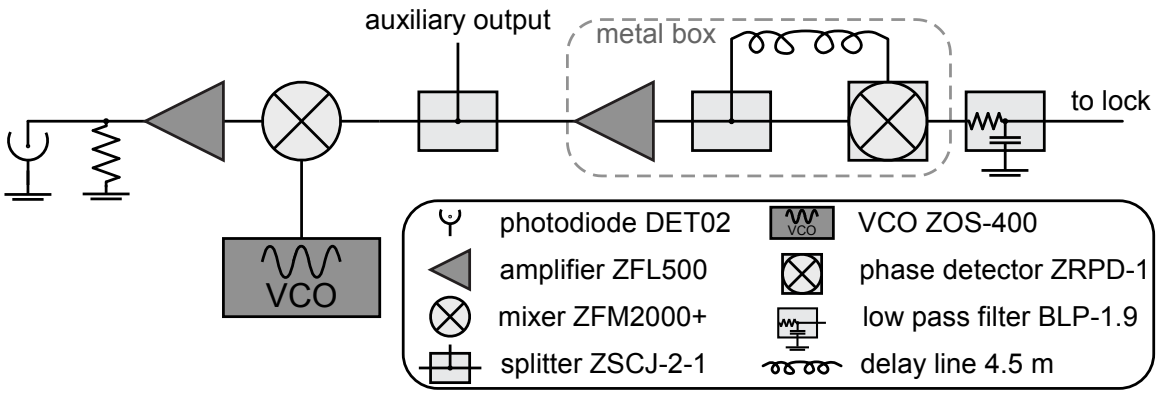

Figure 3.15: The signal for the beat lock is obtained by mixing the beat signal of the two lasers with a reference frequency and detecting the phase between that signal and its delayed part. The last amplifier, the delay line and the phase detector are placed in a metal box to minimize noise.

To be able to adapt to these changes, we stabilize the frequency of the high-field imaging laser with a frequency offset lock. The lock is based on the fact that a beat signal of two laser frequencies accumulates a frequency-dependent phase-shift when propagating through coaxial cable. The time delay introduced by the cable is frequency independent, so the phase shift is only proportional to the beat frequency and a feedback signal to stabilize a laser can be derived [Sch99]. The high-field imaging laser itself is a grating stabilized external cavity diode laser (ECDL), built after a scheme by [Ric95]. The diode used is a anti-reflection coated diode (Eagleyard, EYP-RWE-0790-04000-0750-SOTO1) and the grating is a holographic grating (Thorlabs, GH13-18U) optimized for the ultra-violet to prevent a high power density within the cavity.

Reference light with frequency ν_{ref} is superimposed with the light of the high-field imaging laser with frequency ν_{hfi}. Both beams are matched in power (about 95 µW in each beam) and polarization and coupled into a single mode polarization maintaining fibre. The resulting beat note $\Delta\nu = \nu_{\mathrm{ref}} - \nu_{\mathrm{hi}} = 266\,\mathrm{MHz}$ of the two beams is detected by a fibre coupled fast photodiode (Thorlabs, DET02AFC) with a bandwidth of 1.2 GHz.

In Fig. 3.15 it is shown how the beat signal is processed electronically to obtain a lock signal. To retrieve a feedback signal for the stabilization of the high-field imaging laser, the signal of the photodiode (level $\approx -32\,\mathrm{dBm}$) is first amplified by 20 dB (Mini-Circuits, ZFL-500). In a second step the signal is mixed (Mini-Circuits, ZFM2000+) with the reference frequency $\nu_{\mathrm{vco}} = 320\,\mathrm{MHz}$ from a voltage controlled oscillator (Mini-Circuits, ZOS400). The signal now contains the frequency components $\nu_{\mathrm{vco}} - \Delta\nu$, $\nu_{\mathrm{vco}} + \Delta\nu$, ν_{vco}, $\Delta\nu$ and also higher orders and combinations of those frequencies (see Fig. 3.16).

The signal is split into two, one part is for control purposes, the other part is amplified once more by 20 dB and then divided by another splitter (Mini-Circuits, ZSCJ-2-1). One part is delayed by $l = 4.5\,\mathrm{m}$ of coaxial radio-frequency cable, resulting in a time delay of $\tau = l/c_g \approx 22.5\,\mathrm{ns}$ where the group velocity c_g of the signal is about 2/3 of the speed of light. Both signals are recombined on a phase detector (Mini-Circuits, ZRPD-1). The output voltage U_{err} of the phase detector varies with the cosine of the phase shift ϕ acquired in the coax cable. The phase shift depends

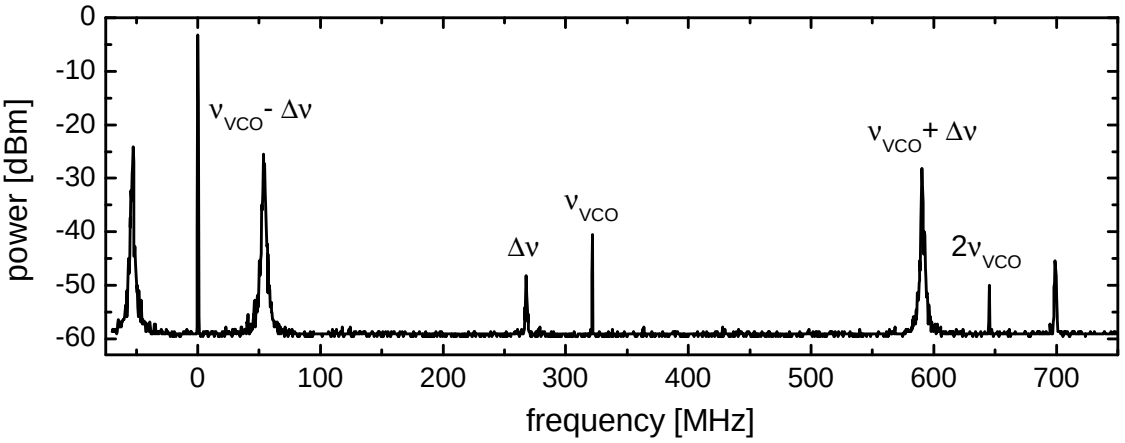

Figure 3.16: Spectrum of the mixed beat signal showing the signal used for locking at $\nu_{\mathrm{vco}} - \Delta\nu$, the beat frequency of the two lasers $\Delta\nu$, the frequency of the voltage controlled oscillator ν_{vco} and higher orders and other combinations of those frequencies.

only on the mixed signal and the time delay between the paths: $\phi = 2\pi(\nu_{\mathrm{vco}} - \Delta\nu)\tau$. One of the zero crossings of the output signal U_{err} is used as a locking point for the feedback for the high-field imaging laser. The spacing of the zero crossings depends on $1/\tau$ and the position can be set with the frequency ν_{vco}. For a wider capture range and a higher locking stability a shorter coax cable can be used. The length of the coax calble was chosen to achieve a high resolution and a narrow laser bandwidth.

The output of the phase detector is sent through a low pass filter (Mini-Circuits, BLP1.9) with cut-off frequency at 1.9 MHz. The error signal U_{err} then feeds back into two separate servo loops: a slow loop ($\leq$ 1 kHz) feeding back to the piezo-electric actuator (Thorlabs, AE0505D08F) setting the length of the cavity of the high-field imaging ECDL and a fast control (bandwidth $\approx$ 1 MHz) to feed back to the current running through the laser diode.

The linewidth of the stabilized high-field imaging laser is estimated by recording the beat signal $\Delta\nu$ of the two lasers. The output of the photodiode is fed into a spectrum analyser. The data of the spectrum analyser is read out to an oscilloscope using the x-y-outputs, averaged 4 times and rescaled to dBm as read from the spectrum analyser. The read-out via the oscilloscope adds electronic noise so a direct conversion to a linear scale introduces big errors. The data is thus first smoothed before rescaling and fitting. The video filter setting of 1 MHz contributes to the linewidth. The data, converted to a linear scale, is shown in Fig. 3.17.

The beat signal of two lasers can be described as the convolution of two Lorentz functions – if no broadening due to e.g. electronic noise occurs. Electronic noise is certainly added to the beat-signal by the spectrum analyser. The locking circuit might also contribute noise. Assuming a Gaussian distribution of the noise, the measured beat-signal is a convolution of Lorentz and Gauss functions, which is a Voigt function. The fit with a Voigt function results in a width of 1.2 MHz for the Gauss part and 0.45 MHz for the Lorentz part of the function. The widths w_i of two Gaussian distributions convolute to $(w_1^2 + w_2^2)^{1/2}$, for a Lorentz distribution it is $w_1 + w_2$. Without exact knowledge of the sources of broadening of the signal 1 MHz is an upper estimate

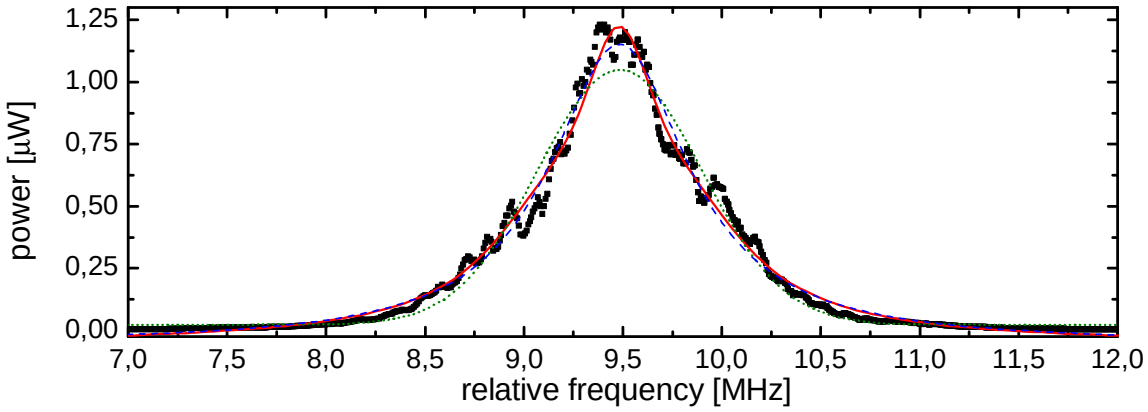

Figure 3.17: The black squares show the recorded and linearised beat signal of the high-field imaging and the reference laser. The red solid line is a Voigt fit to the data. For comparison the Gauss fit (green dots) and the Lorentz fit (blue dashes) are also displayed.

for the width of the high-field imaging laser.

The possible offset frequencies for the lock are limited to 400 MHz by the VCO, for an even bigger range of frequencies a direct digital synthesis chip (DDS) as is used for the evaporation can be employed.

3.9 Computer control and analysis

The whole experiment is controlled by one desktop computer running on the operating system Windows XP. This computer addresses all analogue and digital outputs and accesses the cameras. A laptop computer, also running on Windows XP, is used to control the stepper motor for the optical transport as described in Sec. 3.6. The laptop is also used to view and analyse the data from the CCD camera monitoring the focus size and shape of the dipole trap and the plug beam.

The main computer reads out the cameras and saves the images to the network. The analysis of the measurements is done on a computer running on Linux (Fedora Core 6). For the analysis we use open-source software. We made this choice because most drivers for cards and cameras are more easily available for Windows and our control program was developed for Windows (see 3.9.1). Using open-source software makes the analysis more portable and compatible. With a Linux operation system it is also comparatively easy to make use of remote processing or use and write bash scripts.

3.9.1 Control program and hardware

The hardware for the computer control was chosen to accommodate the laboratory control system as developed by T. Meyrath and F. Schreck (a detailed description and manuals can be found online: [Mey02]). We did not entirely reproduce their system and did not include analogue inputs and radio-frequency synthesizers.

Our control includes at the moment 80 digital and 40 analogue outputs and an interface to DDS evaluation boards. The digital outputs are compatible with TTL and can drive 50 Ω loads. The analogue outputs can each drive a current up to 250 mA and are programmable between -10 and +10 V. A 32-bit National Instruments Digital I/O card (NI6533) interfaces between the output bus and the controlling computer. More details on the used hardware can be found in [Tie09a].

Apart from the outputs mentioned above, the main control computer also uses various protocols to address other devices used in the experiment. The cameras used mostly for the imaging (Sony X710 and SX90) are read out using FireWire. The fibre laser and the Danfysik power supply are programmed via RS232. USB is used for one of the DDS systems and the Apogee camera. An oscilloscope (Fluke, PM3394B) and a multimeter (Tulby Thandar, 1906) can be read out via GPIB.

3.9.2 Software

As mentioned in Sec. 3.9, the control software is based on the control system described in [Mey02]. The program uses Visual C++ functions which provide access to all outputs. In a graphical user interface (GUI) the defined variables can be set and measurement routines can be called. Whenever the measurement routine is called the program is executed twice. In the first run the system is prepared and external devices are pre-set. In the second run the digital outputs are switched, the analogue outputs are set to the programmed voltage and external devices such as the cameras and the optical transport are controlled in a synchronized manner. The time resolution between the different output commands is 3 µs. As mentioned above, we have not implemented any input channels; the cameras are read out using home-written software which is called by the control program. The programs are written in Visual C++ and make use of drivers for the cameras. All cameras get their triggers via digital outputs from the main control program. The same holds for the optical transport: the Maxon motor controller is steered by a separate program running on the laptop. The endpoint and the sinusoidal trajectory are controlled by the separate program but the triggers to start and end the transport are given by the main program.

With each experimental run images are taken. The images are acquired and saved in PGM (Portable Gray Map) format. First they are saved to a local hard drive and then transferred together with files containing the experimental parameters to a network drive. The analysis is then done using software written in GNU C++ running on the Linux computer. A dynamic library offers various routines to fit one- and two-dimensional distributions to the PGM images. The library can either be called from a GUI written in Python 2.5.1 or from command lines in a bash program or shell. For more details about the used software see [Tie09a].

3.10 Sources for radio and microwave frequency

To manipulate the ^{40}K atoms many different frequencies are necessary: for laser cooling and imaging the light has to be shifted by 50–250 MHz, the evaporation and the repump

laser require frequencies in the GHz range and the state manipulation described in Sec. 4.2 works at frequencies in both ranges.

The frequencies for the optical transitions require a frequency stability $< 1\,\mathrm{MHz}$, smaller than the linewidth ($\Gamma = 6.03\,\mathrm{MHz}$). This stability can easily be achieved with voltage controlled oscillators (VCOs). We use VCOs from the ZOS-series manufactured by Mini-Circuits for most of our AOMs. Voltage variable attenuators (Mini-Circuits, ZX73-2500+) regulate the power and Mini-Circuits amplifiers ZHL-3A-S (for $\nu < 150\,\mathrm{MHZ}$) and ZHL-2-S (for $\nu < 150\,\mathrm{MHZ}$) produce the power required, which is up to $\approx 1\,\mathrm{W}$.

The only AOM where we do not use a VCO is the Brimrose AOM that shifts the light to obtain repump light (see Sec. 3.3). The frequency needed there is 1.1 GHz. A VCO with the required frequency stability would have to have voltage drifts of the steering voltage lower than 1 mV, which is hard too achieve. For the repump AOM we employ a DDS (AD9956) as frequency source. The power is amplified by a 2 W amplifier (Hughes, 700-1400MHz).

3.10.1 DDS systems

There are two different types of direct digital synthesis (DDS) systems in use in our experiment. The first system consists of three AD9956 (Analog Devices) DDS chips mounted together with a VCO and a loop filter on evaluation boards. The boards are programmed via USB and updated and synchronized to the experiment with triggers from the digital output boards. Each VCO is phase-locked to a DDS chip. The available output frequencies are then 0.9–1.35 GHz from two of the boards and 200–300 MHz from the third board. The other DDS system is based on four AD9858 (Analog Devices) DDS chips mounted on evaluation boards. These chips can be programmed in parallel via the main bus system. The DDS frequency can then be changed every 15 µs with a 32-bit accuracy. Again VCOs are phase-locked to the DDS chips. The output frequencies of this system are 1–1.3 GHz from one output and 0-400 MHz from the three other outputs. Both DDS systems give out frequencies with a linewidth less than 100 Hz. More details on the used clocks, VCOs and more detailed circuitry of the DDS systems can be found in [Tie09a].

3.10.2 Amplification and switching

All the frequencies for the evaporation and state manipulation from the DDS require additional amplification. Figure 3.18 shows a schematic of amplification stages and the switching to the right antennas. All powers are regulated by voltage variable attenuators (Mini-Circuits, ZX73-2500+) and the signals from the DDS boards can be directed to one of the two outputs of a switch (Mini-Circuits, ZASWA-2-500R+).

The frequency for the hyperfine manipulation is derived from a AD9858 DDS chip. A switch is used to direct the frequency to the main chamber or the science cell. The frequency for evaporation on the hyperfine transition (1.2 GHz) in the main chamber is amplified with a 1 W (Mini-Circuits, ZHL-2-12) and then with a 15 W (RSE, PA15-23) amplifier. The power is sent via a bi-directional coupler and a triple-stub tuner to the antenna. The antenna is a single loop of unshielded BNC cable and has strong

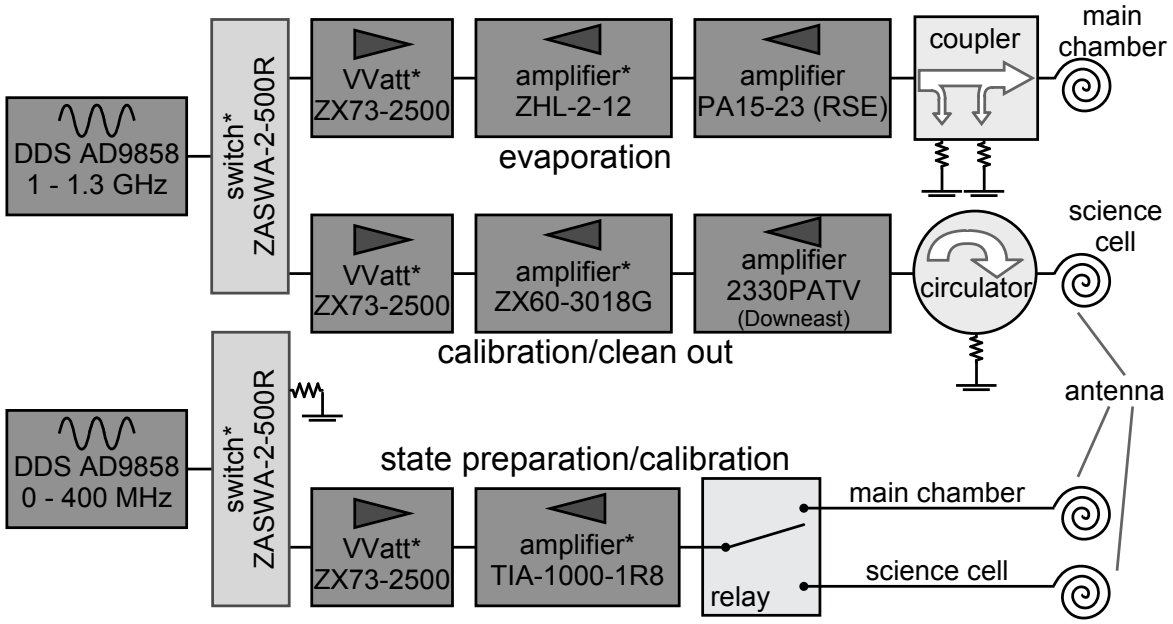

Figure 3.18: Schematic of the amplification stages for the radio and microwave frequencies used to manipulate the atoms. All components marked with * are manufactured by Mini-Circuits. The triple-stub tuner is omitted from the schematic.

resonances. The triple-stub tuner is tuned to achieve a flat frequency response in the range 1.1–1.3 GHz.

When the other output of the switch is in use, the microwave power is increased first by 12.8 dB (Mini-Circuits, ZX60-3018G) and then sent through a 30 W (Downeast, 2330PATV) amplifier and a circulator to the antenna. In the science cell this frequency range is used for the clean out of undesired Zeeman states and for the calibration of the magnetic field as described in Chapter 4. The bi-directional coupler and the circulator protect the amplifiers from the power being reflected back by the antenna.

The lower frequency range from 0–400 MHz is used for the preparation of the proper Zeeman states and for field calibration in the science cell. Here the output from the AD9858 DDS chip can be switched to a 50 Ω terminator to prevent noise. For both the use in the main chamber and the science cell the radio frequency is amplified by the same 4 W (Mini-Circuits,TIA-1000-R18) amplifier. The switching between the two antennas is done with a relay. There is no circulator or coupler in this path as the amplifier is protected against back-reflected power.

The antennas for the radio and microwave frequencies consist of simple wire loops. The antennas for the microwave have one winding and the ones for the radio frequency have seven. For more detailed specifications of the used antennas and the setup for the lithium antennas see Table 3.3 in [Tie09a].

Chapter 4

Experimental sequence

In this chapter a description is given of the preparation of ultracold atoms in the desired Zeeman states and the measurements of Feshbach resonances in collisions between atoms. Figure 4.1 shows an overview of the entire experimental sequence in the form of a timeline. The sequence displayed is used for most measurements of Feshbach resonances, the cases where the procedure is adapted are described in the text. The preparation of the cold atoms involves evaporation steps and a transport of the cold sample to the science cell, where the Zeeman states are prepared and the measurements are taken. Each experimental cycle takes up to 60 s, depending on the holding time at a specific magnetic field to determine magnetic field dependent losses. Furthermore the magnetic field calibration and selected measurements are presented.

A vital step in the experimental sequence is the reproducible preparation of binary mixtures of Zeeman states. This is required to be able to investigate a Feshbach resonance in a specific channel. Multi component mixtures of Zeeman states complicate the assignment of observed loss features.

In earlier experiments on the apparatus [Tie09a] a number of different state preparation procedures were implemented in the main chamber. The ^{40}K atoms were prepared in the fully stretched $|F = 9/2, m_F = 9/2\rangle$ state by forced evaporation of the undesired states in the magnetic trap or in a combination of optical and magnetic trap. Additionally optical transitions at low and high magnetic field and adiabatic sweeps to high-field seeking states were employed. All these experiments made use of Zeeman state sensitive detection by means of a Stern-Gerlach experiment in the main chamber. However, the Stern-Gerlach detection in the main chamber required very low dipole trap frequencies $\omega_r = 2\pi \times 560\,\mathrm{Hz}$ (corresponding to about 2% of the full ODT power) to resolve the individual states to confirm a succesful state preparation. At such low ODT powers a lossless optical transport of the cold clouds to the science cell can hardly be achieved, the ODT is best set to full power for this purpose. In the absence of state dependent detection the preparation of the states at a higher trap depth can leave atoms in undesired states undetected. In addition, without Stern-Gerlach experiment at the science cell, de-polarization of the states during the transport is difficult to detect.

In the course of this work we build a coil to perform Stern-Gerlach detection (see Sec. 3.7) at the science cell. We added switches and antennas (see Sec. 3.10.2) to have

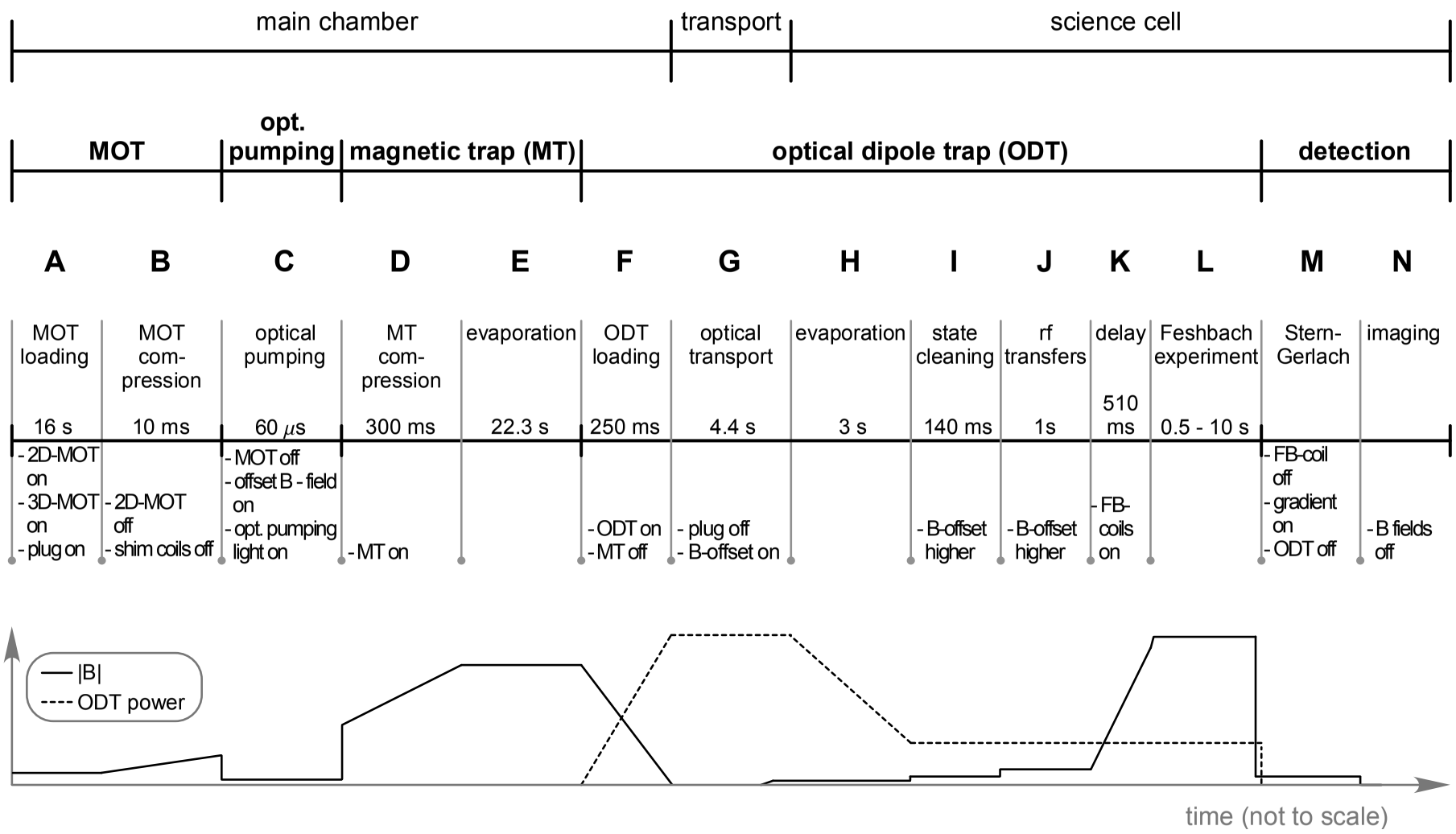

Figure 4.1: Simplified schematic of the experimental sequence. The lower graph shows the applied magnetic fields and the power of the ODT. In the text the experimental steps A to N are described in detail.

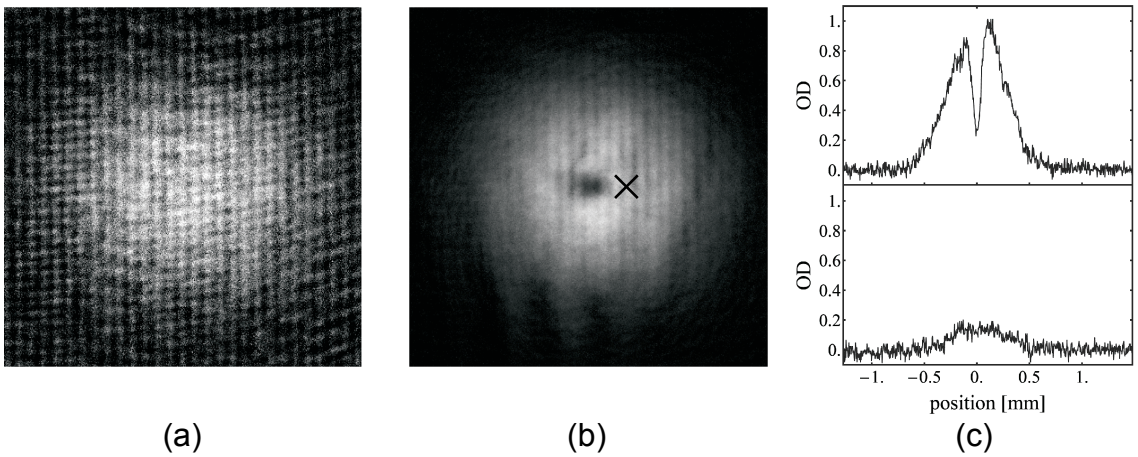

Figure 4.2: Scaled optical density (OD) images of the atoms taken 3 ms after release from the magnetic trap without (a) and with (b) the optical plug. The number of atoms in the cloud depicted in (a) is 1×10^6. Using the same fitting procedure for the cloud in image (b) yields 4×10^6. The cross in (b) indicates the approximate position of the ODT with respect to the plug beam. (c) Vertical cut trough the (unscaled) optical density distribution of the same atom clouds with (top) and without the plug (bottom).

all necessary radio and microwave frequencies for the state preparation available at the science cell as well. The states can now be prepared and detected at the same dipole trap depth. The Stern-Gerlach detection is possible to trap frequencies of up to $\omega_r = 2\pi \times 2.7\,\mathrm{kHz}$ (corresponding to $\approx 40\%$ of the full ODT power). This arrangement also allows for the state sensitive detection of Feshbach resonances.

4.1 Atom cooling and trapping

The experimental cycle starts with 16 s of *MOT loading* (step A in Fig. 4.1). The details of the MOT set-up are described in Sec. 3.4.2. The optical plug (see Sec. 3.5 for details) is switched on from the beginning of the MOT loading. At the end of the MOT loading the 2D-MOT beams are switched off with shutters; and the shim-coils, which create an offset field to move the MOT to a position favourable for loading, are ramped down to zero. The *MOT is compressed* in 10 ms by ramping the magnetic gradient from 14 G/cm to 44 G/cm (step B in Fig. 4.1).

After compression, the MOT field is switched off and an offset field of 3.6 G along the axis of the *optical pumping* beam is switched on (step C, for more details see Sec. 3.4.2). Repump light in all directions is also switched on. The optical pumping light and the repump light transfer the atoms into the magnetically trappable states $f, \ldots j$ in the lower hyperfine manifold of the ground state $|^2S_{1/2}, F = 9/2\rangle$ (see Fig. 2.2). For the forced evaporation step later in the sequence, it is crucial that more than one trappable state is populated, as identical fermions do not thermalize via s-wave collisions. The optical pumping step is optimized accordingly (see Sec. 3.4.2). Following the optical pumping light pulse of 60 µs, the *magnetic trap* is switched on to a vertical gradient of 88 G/cm and subsequently *compressed* by increasing the gradient to 176 G/cm in

300 ms (step D in Fig. 4.1). The offset field for the optical pumping is ramped down to zero during this compression. In this way we load up to 1×10^9 atoms into the magnetic trap.

In the magnetic trap the atom number and temperature are reduced by *forced evaporation* [Hes86, Lui96, Ket96] using microwave radiation driving the transitions from the lower to the upper hyperfine manifold of the ground state (step E). The microwave frequency is resonant with the transitions from the trapped Zeeman states $f, \ldots j$ to the untrapped states in the upper hyperfine manifold $|^2S_{1/2}, F = 7/2\rangle$. The frequency of the microwave radiation is swept from 1160 MHz to 1280 MHz in five sweeps in a total time of 22.3 s. The hyperfine splitting at zero magnetic field is $\Delta E_{\mathrm{hf}} = 1285.79\,\mathrm{MHz}$. The combination of the individual sweeps approximates an overall exponential sweep. Due to the Zeeman effect experienced by the atoms in the gradient of the magnetic trap, atoms which are further from the magnetic trap center have a higher total energy and are preferentially removed from the trap. Rethermalization of the remaining atoms via collisions lowers the temperature of the cloud. At the end of the evaporation stage there are typically 2.5×10^6 atoms in the plugged magnetic trap.

As shown in Fig. 4.2 the optical plug suppresses Majorana losses resulting in an increase of the atom number compared to the case without the optical plug. In the example shown, the cloud is evaporated in four sweeps to 1278 MHz and imaged after 3 ms time-of-flight. With the optical plug switched on, our imaging and fitting procedure does not yield accurate atom numbers as the Stark-shift and the non-Gaussian cloud shape are not taken into account. However, for alignment and optimization purposes the atom number obtained from the fit using a Gaussian profile provides a relative measure to compare to the atom number in the unplugged trap. The fit yields four times more atoms with the plug than without the plug.

For the *ODT loading* (step F in Fig. 4.1), the gradient of the magnetic trap is ramped down to zero in 250 ms while the power of the ODT (see Sec. 3.6) is ramped to full power. The cross in Fig. 4.2 (b) indicates how the ODT beam is aligned with respect to the plug beam. The two beams are co-propagating and the focus of the ODT beam is shifted away from the plug region. At full power the ODT is 345 µK deep and we transfer typically 1.2×10^6 atoms into the ODT, an efficiency of about 50% compared to the atom number in the optically plugged trap. The optical plug is switched off after the loading of the ODT.

The *optical transport* (step G, see Sec. 3.6) transfers the atoms in an approximate (half a period long) sinusoidal velocity profile in 4.4 s over 22 cm from the main chamber into the science cell. To prevent de-polarization of the atom cloud in the ODT during the transport, an offset field of about 2.5 G is ramped up in 50 ms using the fast sweep coil located at the science cell (see Sec. 3.7). We have optimized the switch-on point in time and the magnitude of the offset-field to minimize de-polarization. The field is ramped on after about 75% of the transfer-time has passed. The focus of the ODT is then within about 10% of its final position, which corresponds to a distance of less than a coil diameter away from the center of the fast sweep coils. The full-power ODT contains typically 1×10^6 atoms after the transfer to the science cell.

In the science cell the gas is *evaporatively cooled* by reducing the power of the ODT to 5 – 10% of the initial power (step H in Fig. 4.1). This evaporation takes a total of 3 s and is performed in several ramps approximating an overall exponential ramp [Ada95].

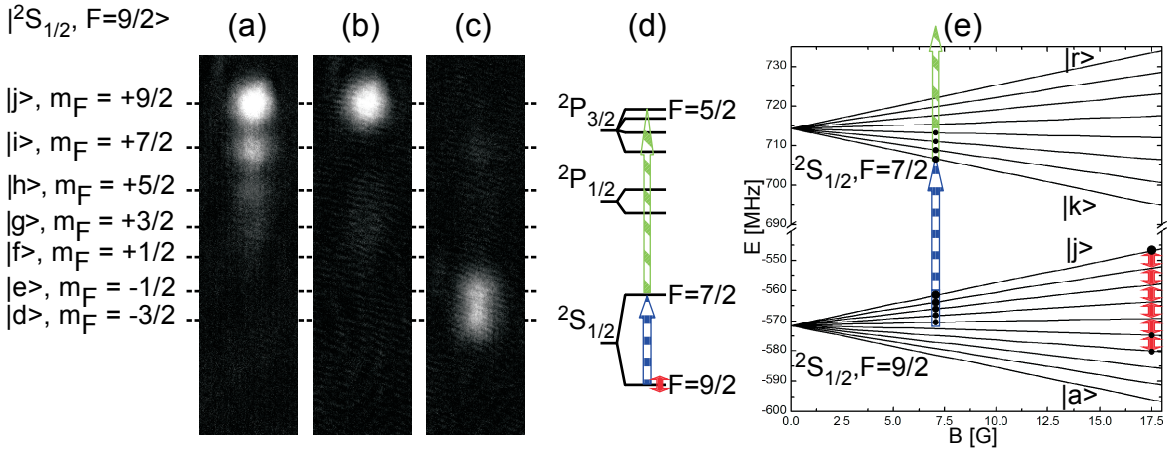

Figure 4.3: Schematics of the state preparation. Optical density images taken after applying a Stern-Gerlach pulse show: (a) state population before the preparation; (b) after clean out; (c) prepared states. As depicted in (d) and (e) the state preparation is done in two steps: With microwave (blue, horizontally striped arrows) atoms in undesired states are excited to the $F = 7/2$ state. Resonant (green, tilted striped arrows) light drives a transition to the $|^2P_{3/2}, F = 5/2\rangle$ state and removes the atoms from the trap. In the second step atoms are transferred to the desired spin states using radio frequency sweeps (red, filled arrows). The last step is done at a higher offset field (see text).

The final power of the ODT is chosen depending on the experiment to be performed. For most of the measurements presented in this chapter and Chapter 5 the final power of the ODT was 60 mW, corresponding to a trap depth of about 12 µK. In this trap there are typically $2 - 4 \times 10^5$ atoms at a temperature of about 1 µK.

4.2 State preparation

For a proper assignment of the various Feshbach resonances in the scattering channels of ^{40}K atoms a pure and balanced binary mixture of only the desired Zeeman states is beneficial. As shown in Fig. 4.3(a) only the low-field-seeking states of the lower hyperfine manifold $|^2S_{1/2}, F = 9/2\rangle$ are populated when the atoms are loaded in the ODT. The offset field applied during the transport preserves this population.

The preparation of a balanced binary mixture of states is done in two steps, first we apply a *state cleaning* procedure in which all atoms except those in the state j ($m_F = 9/2$) are removed (step I in Fig. 4.1). The result is shown in Fig. 4.3(b). Secondly the desired states are populated by means of a *radio-frequency transfer* procedure (step J), the result is shown in Fig. 4.3(c). The images shown were taken using Stern-Gerlach imaging, which will be described in Sec. 4.4. The microwave and radio frequencies employed for the state preparation are derived from the same DDS systems used in the main chamber and switched to the science cell as described in Sec. 3.10.2 and shown in Fig. 3.18. Within experimental error we have not observed any heating of the cloud due to the state preparation.

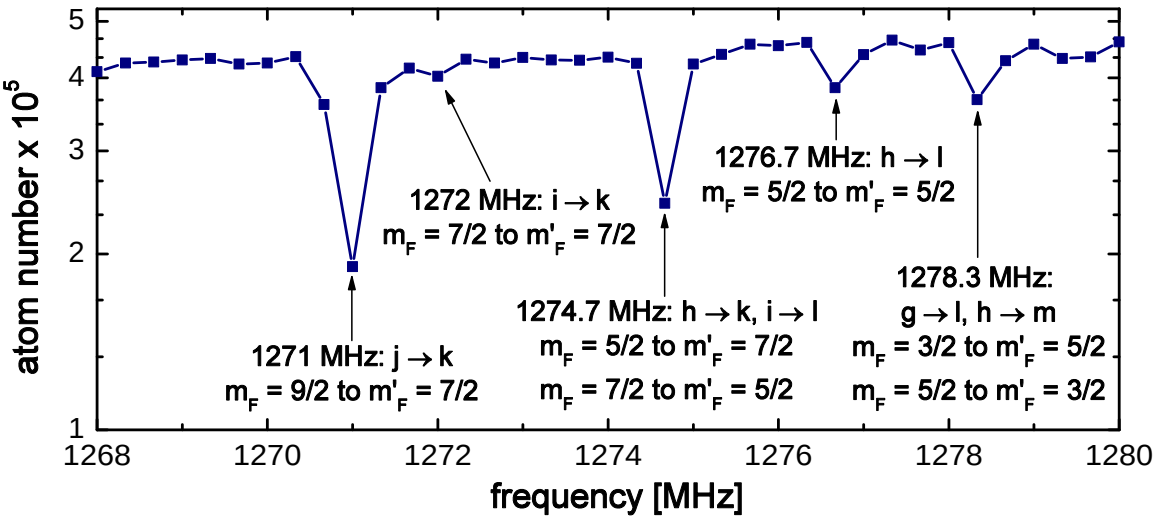

Figure 4.4: Loss features in the atom number when driving the labelled transitions without applying atom removal light. The offset field in this example is about 6 G and the frequency is scanned for each point over 300 kHz in 300 ms.

4.2.1 State cleaning

The state cleaning procedure is illustrated in Fig. 4.3(d) and (e). The atoms in the undesired Zeeman states f, g, h, i in the lower hyperfine manifold $|^2S_{1/2}, F = 9/2\rangle$ are excited with microwave radiation to the upper manifold $|^2S_{1/2}, F = 7/2\rangle$. From there the atoms are removed by resonant σ^--polarized light tuned to the $|^2S_{1/2}, F = 7/2\rangle \longrightarrow |^2P_{3/2}, F = 5/2\rangle$ electronic transition in the D2-line.

The atom removal light is necessary due to spin exchange. To illustrate the phenomenology, we show in Fig. 4.4 the effect of microwave sweeps in the range of 1268–1280 MHz. In this example the sweeps are done without atom removal light. For each point the frequency is swept over 300 kHz in 300 ms. Loss features appear when the frequency is resonant with transitions to the upper hyperfine manifold. The loss occurs because atoms excited to the upper hyperfine manifold undergo spin exchanging collisions [Hap72] with the atoms in the lower hyperfine manifold, resulting in atom loss. Contrary to spin exchange within the lower hyperfine manifold (see Sec. 2.4) this process is exothermic, releasing energy in the mK range, heating the atom clouds to temperatures higher than the trap depth of the ODT. As expected for this spin-exchange mechanism, the loss of the population also occurs in states which are not excited by the microwave radiation. This is shown in Fig. 4.5, where the atoms are detected with Stern-Gerlach imaging.

The state cleaning for the Feshbach measurements is done in the science cell at an offset field of 7.2 G produced by the fast sweep coils in the presence of atom removal light. The field is ramped up in 50 ms from the offset value used during the transport. With a series of four sweeps of microwave radiation the atoms from the undesired states f, g, h, i in the lower hyperfine manifold are excited to the states k, l, m, n in the upper hyperfine manifold. In each of the four sweeps, the microwave radiation is swept over a range of 50 kHz in 35 ms. These sweeps are done around the frequencies to drive

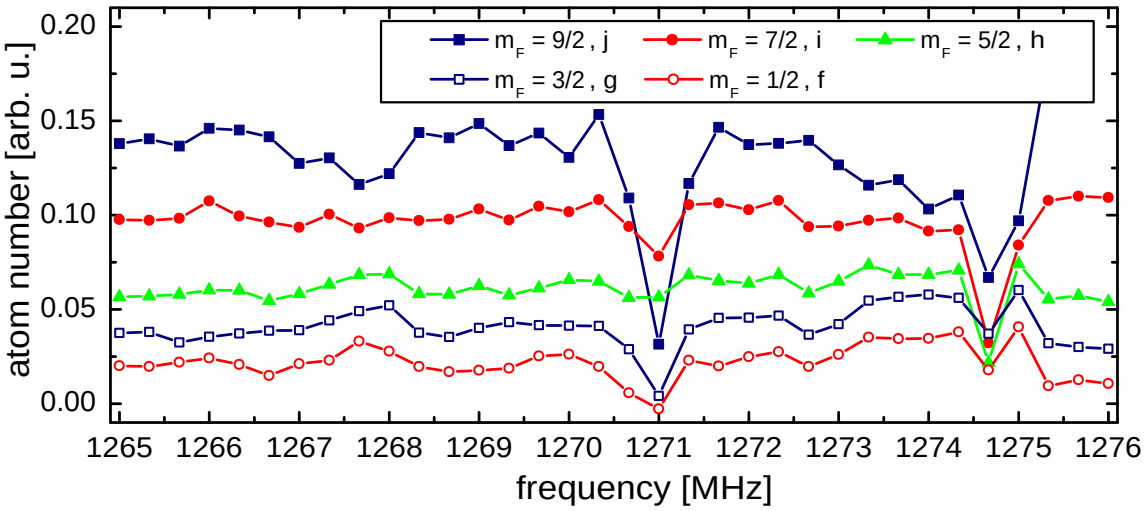

Figure 4.5: Loss in spin states due to spin exchanging collisions with states in the upper hyperfine manifold when not applying atom removal light. Around 1271 MHz only the $j \rightarrow k$ microwave transition is driven. At 1274.6 MHz only the transitions $i \rightarrow l$ and $h \rightarrow k$ are addressed. The offset field in this example is about 6 G.

the transitions $g \rightarrow n$ and $f \rightarrow m$ (first sweep); $h \rightarrow l$ (second sweep); $i \rightarrow l$ and $h \rightarrow k$ (third sweep); and $i \rightarrow k$ (fourth sweep). The atom removal light tuned to the $|^2S_{1/2}, F = 7/2\rangle \longrightarrow |^2P_{3/2}, F = 5/2\rangle$ transition prevents losses due to spin exchange between the microwave excited atoms and the remaining atoms in the states in the lower hyperfine manifold. At the offset field employed, the Zeeman splitting of the four populated states in the upper manifold is about 6 MHz, the same as the linewidth Γ of the D2 line. The Zeeman splitting of the electronically excited states in the $|^2P_{3/2}, F = 5/2\rangle$ manifold at the offset field is about 2Γ. With sufficient intensity, it is not necessary to sweep the frequency of the atom removal light, but adequate to tune the frequency within about 2Γ for optimal atom removal. The intensity and detuning of the atom removal light is optimized by exciting the population of one of the trapped states by microwave radiation to the upper hyperfine manifold, applying atom removal light and detecting the remaining atoms with Stern-Gerlach imaging. When the atoms are efficiently removed from the upper hyperfine manifold, no losses occur in the remaining trapped states. The population in the cleaned-out state is minimized, while the occupation in the other states is conserved. When the intensity of the atom removal light is too high, also atoms in the lower hyperfine manifold are optically excited to the $|^2P_{3/2}\rangle$ manifold and are lost from the sample. The optimal intensity was established experimentally.

4.2.2 State transfers

The state cleaning leaves atoms only in the $|2\,S_{1/2}\,F = 9/2, m_F = 9/2\rangle$ state. For a 70 mW deep trap, the atom number is typically 1.7×10^5. From there the atoms are transferred in two radio-frequency sweeps [Rub81] to the desired final states. To get a good resolution between the states, the offset field is increased from 7.2 G to about

17 G in 100 ms. The energy difference between the Zeeman states then differs by about 41–47 kHz, which we are able to resolve with radio frequency. A higher field would in principle enable the reduction of the sweep time, nevertheless it was chosen to keep the field as low as possible to be able to explore Feshbach resonances at a field as low as possible. The first sweep over 90 kHz in 500 ms transfers the atoms adiabatically into the state with the higher Zeeman energy of the two desired states. A second sweep over 30 kHz in 500 ms produces the mixture with the adjacent state. For this second sweep the radio frequency power is reduced to 1/3 of its initial value. The final states are each populated with typically 3×10^4 atoms. The temperature of the cold atoms is 1 µK, corresponding to $T/T_F \approx 1.5$.

The first radio-frequency transfer shows the best result when only one state is initially populated. Up to four final states are populated by the transfer if two states are initially populated. The combination of spin cleaning and radio-frequency transfers as described above is used to produce mixtures of adjacent states. However for the $m_F = 7/2$ and $m_f = 5/2$ mixture $(i + h)$, as well as for the $m_F = 9/2$ and $m_F = 5/2$ mixture $(j + h)$ the preparation procedure is adapted. For the $i + h$ mixture, first an adiabatic transfer is performed from the state $m_F = 9/2$ to to the state $m_F = 5/2$ and then atoms in the undesired states are removed as described above. Accordingly for the $j + h$ mixture the state $m_F = 7/2$ is transferred to the state $m_F = 5/2$ and the atoms in undesired states are cleaned out. This method results in higher atom numbers in the mixtures. It can also be adapted for mixtures of the states a, b and c. There the population in the states $j, i, h \ldots$ is first transferred adiabatically into the $a, b, c \ldots$ states, before employing further state cleaning and state transfers.

4.3 Field-dependent loss measurements

Following the spin preparation the offset field is decreased from 17 G to 6.45 G and the power supply of the main Feshbach coils is switched from the dummy load to the coils (see Sec. 3.7). The magnetic field reaches 95% of its final value within 10 ms. It takes in total 0.5 s to reach the set current to within 1 ‰. Once the final field is reached by the Feshbach coils the fast sweep coils are ramped up within 10 ms. The fast sweep coils produce fields up to 17 G and are used to scan the magnetic field around a Feshbach resonance to resolve details. The Feshbach coils produce the big magnetic field offset to reach field values below the resonance and the fast sweep coils are used to scan over the resonance. In this way we prevent that the field drifts slowly over the Feshbach resonance during the settling of the current.

After the *delay* (step K in Fig. 4.1) due to the settling of the current, the actual *Feshbach experiment* (step L) is performed. We determine the positions of the Feshbach resonances by an increase in the atomic loss rate [Reg03a]. The mixture of cold atoms in the prepared states is held at a magnetic field value for an adjustable holding time (0.5 – 10 s) and the remaining atoms are detected subsequently. For scans over magnetic field ranges larger than 17 G, only the current through the main Feshbach coils is scanned. To minimize in this case the effect of the settling of the current on the detected relative losses, the actual measuring time is chosen much longer (>3 s) than the settling time. Switching the Feshbach coils off takes about 600 µs; to prevent depolarization of the spin states due to the switching, a small offset field is applied.

4.4 Stern-Gerlach imaging

Once the Feshbach coils are switched off, the mixture is detected by absorption imaging after a time-of-flight. To distinguish the different spin states contained in the cold atom cloud a *Stern-Gerlach gradient field* (step M in Fig. 4.1) is applied before zero-field *imaging* (step N in Fig. 4.1). The magnetic gradient is pulsed on for the first 3.7 ms of the time-of-flight after the cold atoms are released from the optical dipole trap. A single coil, situated about 1 cm above the atom cloud, produces a gradient of 100 G/cm, which is sufficient to separate the spin states during the 4 ms total time-of-flight. The current is switched between a resistive dummy load and the coil using FETs. This ensures a fast switching of the Stern-Gerlach field. Again, to prevent depolarization of the states during the switching, an offset field of 6.45 G is applied.

After all the coils are switched off and the magnetic field has decayed, the imaging and repump light flashes are applied and the atoms in the separated clouds are detected. The switch-off of the offset field does not affect the state-dependent detection, as the initial population distribution in the states spin is now separated in space. Any depolarization at this stage is not relevant, the imaging itself is done without an applied field (see Sec. 3.8).

The Stern-Gerlach pulse is sufficient to separate the spin states in clouds at temperatures of around 12 µK, so it is necessary to evaporate from the ODT to a trap depth of at most 140 µK. This trap depth corresponds to 40% of the full power of the ODT and results in a trap frequency of $\omega_r = 2\pi \times 2.7\,\mathrm{kHz}$. Compared to the Stern-Gerlach detection previously implemented in the main chamber [Tie09a], this is a major improvement.

A separation of the spin states of clouds at even higher temperatures could be achieved with a higher magnetic field gradient. In the restricted available space this could be done by using two coils, but then the separation of the states is impeded as the atoms get partially trapped.

4.5 Magnetic field calibration

The magnetic field is calibrated by driving the transitions either between the two ground state hyperfine manifolds or between Zeeman states within the lower hyperfine manifold. For the frequencies required the corresponding magnetic field is calculated using the Breit-Rabi formula as described in Appendix B.1. We calibrate the field during the measurement part of the sequence (see Sec. 4.3).

The choice of the transition employed for the calibration depends on the frequency ranges available from the DDS system (see Sec. 3.10.1). The DDS system delivers either radio frequency radiation in the range 0 – 400 MHz or microwave frequency radiation in the range 1 – 1.3 GHz. In the case of high magnetic fields the transition between the Zeeman states $|^2S_{1/2}, F = 9/2, m_F = 9/2\rangle$ and $|^2S_{1/2}, F = 9/2, m_F = 7/2\rangle$ is driven with radio frequency. The calibration is done by detecting the population in the $m_F = 7/2$ state versus the frequency. An example for the calibration with radio frequency is shown in Fig. 4.6(b). For low field the hyperfine transition between $|^2S_{1/2}, F = 9/2, m_F = 9/2\rangle$ and $|^2S_{1/2}, F = 7/2, m_F = 7/2\rangle$ is driven and the loss in the $|F = 9/2, m_F = 9/2\rangle$ state is detected with changing frequency. In both cases the

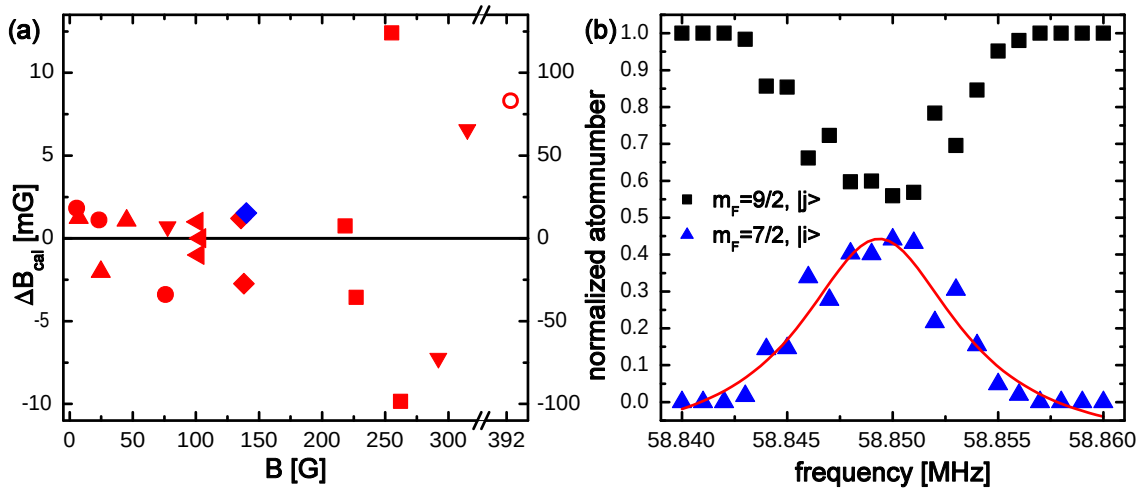

Figure 4.6: (a) Calibration error ΔB_{cal} of the magnetic field. The error given is the difference between the values obtained with the Breit-Rabi formula and the corresponding fitted linear calibration function. The different bullet shapes correspond each to one dataset for one calibration function. Note that the axis on the right hand side has a different scale. This scale is for the point at 392 G (empty circle) belonging to the calibration set marked with circles. (b) Data for the magnetic field calibration at 139.392 G (blue diamond in (a)). The atoms are transferred from state j to state i using radio frequency. The frequency dependent population in i is fitted with a Lorentz. The center frequency of the fit is used to calculate the magnetic field using the Breit-Rabi formula Eq. B.5. The width of the fitted Lorentz in this example corresponds to 10 mG.

radiation is applied for 50 ms at powers low enough to prevent power-broadening of the transition. The frequency is scanned in steps of 1 kHz.

The center frequency of the transition is determined by fitting a Lorentz function to the data. The position of the center frequency has an error of < 1 mG for all fitted data. The width of the fitted Lorentz is < 15 mG. The values of the magnetic field calculated using the Breit-Rabi formula are then fitted with a linear calibration function. This function is used to calculate the magnetic field in dependence of the voltage employed to control the power supply.

The magnetic field calibration was repeated at regular intervals, taking calibration points around the measured Feshbach resonances. Over time the offset field drifted, which might be due to a change of stray fields from power supplies and other apparatus which were added to the setup in the vicinity of the Feshbach coils.

A measure for the accuracy of the calibration is the difference ΔB_{cal} between the data points taken and the magnetic field calculated according to the linear calibration formula. In Fig. 4.6(a) this error is shown. For magnetic field values below 315 G the absolute error is less than 15 mG, below 230 G it is below 5 mG, corresponding to a relative error of $\Delta B/B = 2 \times 10^{-5}$. At 392 G the calibration is 80 mG away from the data point ($\Delta B/B = 2 \times 10^{-4}$).

Limits to the magnetic field precision

The stability of the power supply for the Feshbach coils (see Sec. 3.7) is specified to <1 ppm, so the precision of the measured magnetic field is likely to be limited by other factors. The current running through the coil gives rise to heating and thermal expansion, which lowers the magnetic field for a given current. For a linear thermal expansion of the coil, the relative change in magnetic field is $\Delta B/B = -1.7 \times 10^{-5}/\mathrm{K}$. At high currents (28.5 A corresponding to 500 G), the temperature of the coils rises only slowly by 3° C with a time-constant of 4 min as described in [Tie09a]. The maximum temperature of the coil is constant to within 0.1 K for a period of two hours. This is limited by the temperature drift of the cooling water which runs through the mount at a pressure of 2 bar. The temperature of the cooling water also shows day to day drifts of 0.5 K. During the experimental cycle, the coil is on for at most 11 s the temperature increases in this time by approximately 0.082 K, resulting in $\Delta B/B < -1.4 \times 10^{-6}$. When including the delay time due to the settling of the current and considering a typical measuring time of 4 s the relative change in magnetic field is at most -4.3×10^{-7}. This shows that in principal a very high accuracy can be achieved with the Feshbach coil and the employed power supply. The thermal stability of the Feshbach coil is not limiting the measured magnetic field precision.

The only part of the Feshbach coil circuit which was not optimized for thermal stability when taking the data presented in this thesis, is the MOSFET switch. The MOSFETs are likely to be responsible for the observed loss in magnetic field precision at large magnetic fields. The MOSFETs are mounted on heat sinks and are not actively cooled. Running a high current through the MOSFETs leads to considerable heating (up to 20° C) within the measuring time. The drain – source resistance of a MOSFET rises non-linearly with temperature and current. For a higher current the effect is more severe and can lead to a runaway behaviour which ultimately destroys the MOSFET. The 20° C rise in temperature increases the resistance by a factor 1.5, however the Danfysik power supply is not specified to regulate such big load changes. After the switch from the dummy load to the coil the current takes 0.5 s to settle within 1 ‰[†]. It is specified to regulate up to 10 % resistance changes within <0.05 ppm. Recently the MOSFET switch has been equipped with water-cooling, so the change in resistance of the MOSFETs should be below 10% and we should be able to eliminate the switch as a cause for the loss in accuracy.

A limiting factor for the magnetic field precision, which we could not test yet, can be short term fluctuations of the background magnetic field originating from the electrical equipment running at 50 Hz of the main power line. The background is not in phase with the experimental cycle and contributes to a varying offset. To improve the magnetic field stability in the future, the experimental cycle could be synchronized to the 50 Hz frequency of the main power line. This would suppress common noise in the offset magnetic field which can influence the precision of the state preparation and calibration. With the synchronization it would also be possible to test the long-term stability of the magnetic field.

Another cause for the lower limit of the measured magnetic field precision can

[†]To measure the current running through the Feshbach coils we use a Agilent (N2775A, 50MHz) current probe. The current is limited to 15 A, corresponding to a field of about 260 G. The resolution is about 20 mA corresponding to 350 mG (1 ‰).

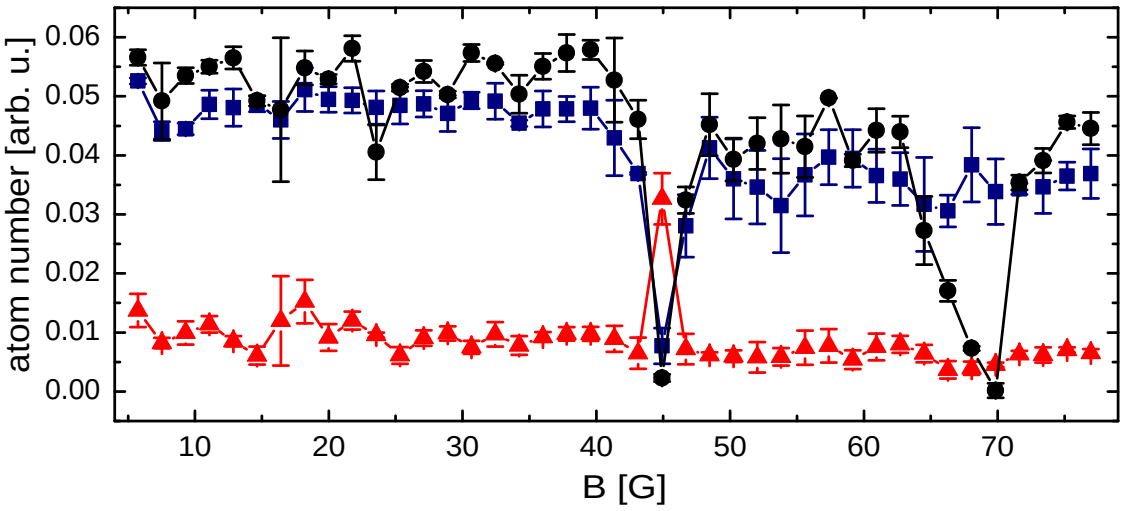

Figure 4.7: p-wave resonance between state h (black circles) and j (blue squares). On the resonance the atoms re-appear in the i channel (red triangles). At 68(1.8) G is a p-wave resonance in the $h + h$ mixture. The lines are guides to the eye.

be remaining field inhomogeneities over the volume where the cold atom sample is located. Power supplies and other apparatus located near the Feshbach coils contribute to the overall magnetic field and add gradients. The homogeneity of the magnetic field produced by the Feshbach coils was determined in a separate set-up (see Sec. 3.7). The implementation of a crossed dipole trap would reduce the sample volume, reducing the effect of inhomogeneities. The trim coils described in Sec. 3.7 could be put to use to correct for remaining curvatures.

4.6 Measured Feshbach resonances

The positions of Feshbach resonances measured in this work are presented in Tables 5.1 and 5.2. All Feshbach resonances were measured by observing the losses in dependence of the magnetic field. The loss features have varying profiles, the narrow and isolated s-wave resonances both show a symmetric profile which we fit with a Lorentz function to determine the position B_0 of the Feshbach resonance and the widths ΔB_{L} of the loss feature. The widths given in Table 5.1 are the widths of the loss features, which are not identical with the resonance width ΔB. The p-wave resonances and some of the s-wave resonances show an asymmetric profile. In this case we determine the position of the Feshbach resonance as the magnetic field where the biggest loss occurs. The widths stated are the full widths at half maximum (FWHM). For all measurements where we used Stern-Gerlach imaging, the analysis and determination of B_0 and ΔB_{L} is done for all involved spin states separately and the stated values are averages.

For some p-wave resonances we also resolve the doublet feature due to magnetic dipole-dipole interactions [Tic04]. The assignment of the observed loss features to s- or p-wave resonances is simplified by measuring spin-dependently: if only one spin state shows losses at a certain field, an s-wave resonance can be excluded due to the fermionic nature of the atoms.

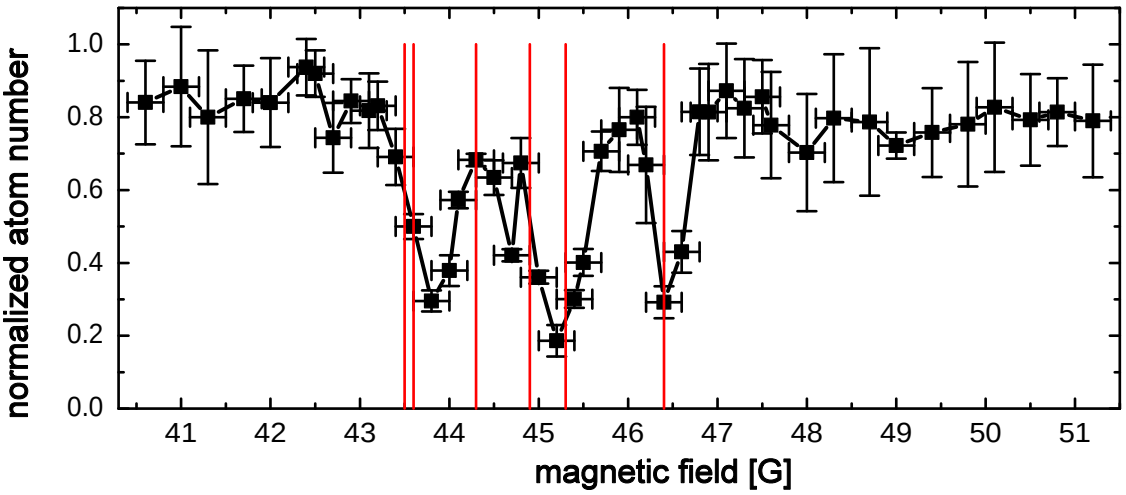

Figure 4.8: p-wave Feshbach resonance in the $i+i$ system. The black squares show the population in state i. The line is a guide to the eye. The values obtained with coupled channel calculations in (see Table 5.2) are shown with red vertical lines. The error bars represent the statistical error (y-values) and the step size of the scan (x-values).

4.6.1 p-wave resonances with special features

Figure 4.7 shows a p-wave resonance at 44(1.8) G in the $h+j$ mixture. The feature at 68(1.8) G is a p-wave resonance in the $h+h$ mixture. With the Stern-Gerlach imaging the loss in the h and j states is clear. However, on the resonance the state i is populated. The state i has a Feshbach resonance in the vicinity as displayed in Fig. 4.8. Spin exchanging collisions where $h+j \rightarrow i+i$ are normally suppressed. The final state consists of identical states, which for fermions is forbidden.

Analysis of the resonances in the two mixtures around this field shows, that both Feshbach resonances originate from the second least bound state in the triplet molecular potential. The difference in energy between the $h+j$ and the $i+i$ mixture at these low fields is less than 400 kHz, corresponding to a thermal energy of less than 20 µK. The depth of the optical trap in the measurement displayed in Fig. 4.7 is about 45 µK. The heating due to the energy difference between the two mixtures does therefore not lead to substantial atom loss from the trap. The relative magnetic moment $\mu_{\mathrm{rel}} = -\partial E/\partial B$ is negative, so the bound state approaches the free atom threshold from above with rising magnetic field. At 44(1.8) G the $h+j$ mixture is resonant with the bound state of the molecular potential; at the same magnetic field the same state can decay through the $i+i$ channel. This is because the energy of the asymptote of the $i+i$ channel is lower than the energy of the molecular state at this magnetic field. The atoms can enter the $i+i$ channel from the $h+j$ channel via the molecular level.

The double loss feature observed in some of the p-wave resonances in Table 5.2 has its origin in the p-wave scattering of different projections of the total angular momentum M_T of the pair onto the magnetic field direction. The magnetic dipole interaction of the atoms leads to a small energy difference of the projections, splitting the resonance into two. Accordingly, Feshbach resonances involving higher partial waves with $l > 0$ split into $l+1$ resonances corresponding to the projections $M_l =$

$0, |\pm 1|, |\pm 2|, \ldots |\pm l|$. This feature is thermally broadened and therefore only detectable when the temperature of the atoms is lower than the splitting [Tic04].

The multiplet structure in Fig. 4.8 in the $i + i$ mixture was measured at a temperature of about 3 µK. It is not only a double but a quadruple feature, which is caused by the coupling of channels due to dipole-dipole interaction. The $i + i$ channel couples to the $i + j$, $h + i$ and $h + h$ channel and depending on the projections of M_l on these channels Feshbach resonances occur at different magnetic fields. The values obtained with coupled channel calculations (see Sec. 5.3.1) are shown as vertical lines in Fig. 4.8.

When forming molecules at a p-wave resonance, the projections of the total angular momentum is visible in the angular distribution of the dissociated molecules as demonstrated by [Gae07]. P-wave resonances, where the magnetic dipole interaction splits the resonance into two distinct resonances, have been proposed to tune anisotropic interaction between atoms [Tic04, Bar02].

4.6.2 Width of a Feshbach resonance

Apart from the exact position of a Feshbach resonance it is also important to determine its width. The width has influence on the resonance strength (see Sec. 2.5) and on the requirements for the magnetic field stability. The width of the loss feature ΔB_L is affected by more parameters than the resonance width alone and gives therefore no quantitative information on the resonance width. To determine the width of a Feshbach resonance the effect of scattering properties of the cold cloud can be measured. We evaporate the cold atom cloud around the Feshbach resonance in the $c + d$ mixture at 178.3 G and detect the size of the cloud after evaporation in dependence of the magnetic field.

For the measurement described in this section the experimental sequence as described above is slightly altered. The evaporation in the optical dipole trap is done in two steps. At first the power of the ODT is ramped down exponentially from full power to 150 mW in 600 ms. At this trap depth the atoms are prepared in a $c + d$ mixture with the method described in Sec. 4.2. Then the Feshbach coils are switched on and once the final field is reached, a second evaporation step follows. In 5 s the power is reduced to 20 mW in an exponential ramp. After another 200 ms at the final field the cold atom cloud is imaged at zero field without the Stern-Gerlach pulse after 3.5 ms time-of-flight. The data points in Fig. 4.9 show the cloud size in the radial direction of the ODT.

When evaporating the cold atom cloud around a Feshbach resonance the scattering cross section σ changes with magnetic field. As a result the final atom number and temperature of the cloud differ, for small σ the evaporation is less efficient and the cloud is hotter and bigger and vice versa. Just below the resonance the cloud is heated by 3-body losses due to the molecular state present and the cloud size is increased. The two data points, where this occurs (shown as squares in Fig. 4.9) have been omitted in the fit described below.

We fit the data using an approximative model. The behaviour of the cloud size $S(B)$ with varying magnetic field is attributed to the behaviour of the scattering cross section σ over the resonance (see Sec. 2.3). The maximum cloud size S_0 is assumed to occur at the zero crossing of the scattering length $B_{a=0} = B_0 + \Delta B$ and the minimal value at the resonance position B_0. During the evaporation ramp, the depth of the

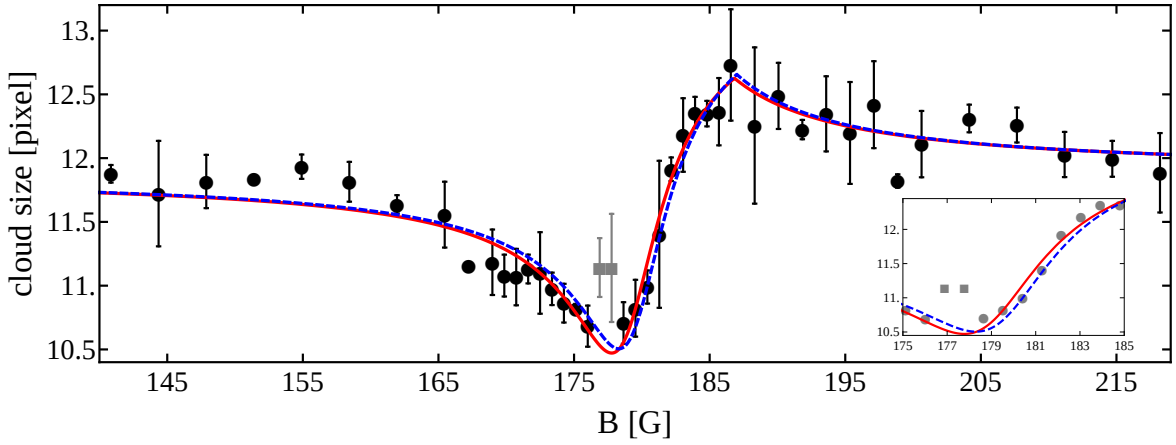

Figure 4.9: The size of the cold atom cloud after 3.5 ms expansion. The error bars display the statistical error. The data is fitted with the model described in the text (full line). As a comparison, the fit to the data using the values for ΔB and B_0 from CC calculations is shown (dashed line). The inset is a zoom into the region around the resonance. The data shown as squares is omitted from the fit.

trap $U_0(t)$ changes as

$$U_0(t) = U_0 e^{-t/\tau_R},$$

with a time constant τ_R which is much longer than the collision time τ_{Col} of the atoms and the oscillation time in the trap. The ramp corresponds to an adiabatic decompression and the temperature evolves in a harmonic trap as [Lui96, Wal10]:

$$\frac{\dot{T}}{T} \approx \frac{\dot{U}(t)}{U(t)} = -\frac{1}{\tau_R}. \tag{4.1}$$

When $\eta = U_0(t)/(k_B T)$ is large and spilling of atoms can be neglected [Wal96], the evaporation rate is:

$$\frac{\dot{N}}{N} = -n_0 \overline{v}_r \sigma e^{-\eta} = -\frac{1}{\tau_{Col}} e^{-\eta}, \tag{4.2}$$

with the density n_0, the relative velocity $\overline{v}_r$ and the scattering cross section

$$\sigma = \frac{4\pi a^2}{1 + k^2 a^2} = \frac{4\pi a_{bg}^2 \left(1 - \frac{\Delta B}{B - B_0}\right)^2}{1 + k^2 a_{bg}^2 \left(1 - \frac{\Delta B}{B - B_0}\right)^2}. \tag{4.3}$$

The temperature is related to the evaporation rate [Lui96, Wal10]:

$$\frac{\dot{T}}{T} = \frac{1}{3}(\eta - 2)\frac{\dot{N}}{N}. \tag{4.4}$$

Combining the equations 4.2,4.4 and 4.1, leads to an expression for η

$$e^{\eta} = \frac{1}{3}\tau_R n_0 \overline{v}_r \sigma (\eta - 2). \tag{4.5}$$

This equation can be solved with the Lambert $\mathcal{W}(x)$ function (product logarithm) [NIS11, Sco06, Wit11]. For equations of the form

$$e^{-cu} = a(u-b),$$

where $a, b, c \in \mathfrak{R}$, it is

$$u = b + \frac{1}{c}\mathcal{W}(\frac{ce^{-cb}}{a}).$$

Using this result we obtain:

$$\eta = 2 - \mathcal{W}\left(\frac{-3e^2}{\tau_{\mathrm{R}} n_0 \overline{v}_r \sigma}\right) = 2 - \mathcal{W}\left(\frac{-3e^2\tau_{\mathrm{Col}}}{\tau_{\mathrm{R}}}\right). \tag{4.6}$$

For $|x| < 1/e$ the Lambert $\mathcal{W}(x)$ function can be written as a power series

$$\mathcal{W}(x) = x - x^2 + \cdots .$$

For a ramping time constant $\tau_{\mathrm{R}} \gg \tau_{\mathrm{Col}}$ the condition is fulfilled and the expression for η takes the form:

$$\eta \approx 2 + \text{const.} \times \sigma^{-1}. \tag{4.7}$$

The cloud size after expansion is described in a harmonic approximation (see Eq. A.12 and [Gri00]) by:

$$S \propto \frac{1}{\sqrt{\eta}}. \tag{4.8}$$

The final size S_f of the cloud after evaporation is the initial size $S_i \propto \sqrt{k_{\mathrm{B}} T_i / U_i}$ reduced by a value depending on the field dependent behaviour of η during the evaporation:

$$S_f = S_i - \Delta S(\eta(B)).$$

At the zero crossing of the resonance, where $\sigma = 0$, the cloud will not thermalize. In the experiments the initial η is rather large (≈ 10), so we assume that spilling of atoms only plays a minor role [Wal96] and that the size of cloud S_0 for $\sigma = 0$ is determined by the initial temperature T_i and the final potential depth U_f as: $S_0 = \sqrt{U_i/U_f}\, S_i$. The field dependent size of the cloud can then be described as

$$S_f \propto S_0 \left(1 - \frac{1}{\sqrt{\eta(B)}}\right).$$

Replacing $\eta(B)$ with the expression for η in Eq. 4.7, and rearranging the expression we obtain as a fitting function for the measured cloud size:

$$S(B) = S_0 \left(1 - \left(\frac{P_1^2 \left(1 - \frac{\Delta B}{B - B_0}\right)^2}{1 + P_2^2 \left(1 - \frac{\Delta B}{B - B_0}\right)^2}\right)^{1/2}\right), \tag{4.9}$$

where the width ΔB and the position B_0 of the resonance and the maximum cloud size S_0 are fitting parameters. The fitting parameters P_1 and P_2 incorporate the effect of

Parameters	B_0[G]	ΔB[G]	S_0[pixel]	P_1	P_2	$B_{a=0}$[G]	S_{bg}[pixel]
Fit to Data	177.774	9.056	12.626	0.06313	0.36997	186.83	11.8784
CC and Data	*178.3*	*8.7*	12.657	0.06596	0.38801	187.00	11.8787

Table 4.1: Fit results for the fit to the cloud size in Fig. 4.9, where the full line is a full fit to the data and the dashed line is the fit using the CC values for B_0 and ΔB. The parameters $B_{a=0}$ and S_{bg} are calculated using the fit results.

the background scattering length a_{bg}, the atom impulse k on the cloud size and other constants. Away from the resonance the cloud size has the background value

$$S_{\mathrm{bg}} = S_0 \left(1 - \left(\frac{P_1^2}{1+P_2^2}\right)^{1/2}\right).$$

For comparison we also fit the data including results from CC calculations (see Table 5.1). The fitting function has then two fitting parameters less, $B_0^{\mathrm{CC}} = 178.3\,\mathrm{G}$ and $\Delta B^{\mathrm{CC}} = 8.7\,\mathrm{G}$. The fitting results for the fit to the data (depicted as a full line in Fig. 4.9) and the fit where only S_0, P_1 and P_2 are fitted (dashed line) are displayed in Table 4.1. In this measurement the magnetic field is varied around B_0 in steps of 0.88 G and around the zero crossing in steps of 1.76 G. We use the step size of the scan as a conservative estimate for the error in magnetic field. The Feshbach resonance position we determine by a loss measurement as described in Sec. 4.3 to be $B_0 = 178(1)\,\mathrm{G}$.

Another way to measure the width of a Feshbach resonance is via the cross - dimensional thermalization as shown in [Lof02]. However, this requires an aspect ratio of the two radial axes of the ODT, which we do not have. In [Joc02, O'H02] the zero crossing of the Feshbach resonance at 850 G of ^{6}Li was measured by observing the evaporation around the zero crossing at a fixed trap depth. This method works most satisfactorily when the background scattering length is very large. In ^{6}Li it is $a_{\mathrm{bg}}^{\mathrm{Li}} \approx -3000\,a_0$, whereas around the Feshbach resonance at 178.3 G in the $c+d$ state in ^{40}K the background scattering length is $a_{\mathrm{bg}}^{\mathrm{c+d}} \approx 186\,a_0$. The evaporation at a fixed trap depth can be also used for smaller background scattering lengths in two-species experiments. In the case of the ^{6}Li-^{40}K mixture [Tie10b], the ^{40}K serves as thermal bath and the loss over time of the ^{6}Li around a Feshbach resonance is used to determine ΔB. This is possible as the trapping potential for ^{40}K has more than double the depth than for ^{6}Li. When using an optical lattice, the dephasing of Bloch oscillations and ballistic expansion from the lattice can be used to determine the width of a Feshbach resonance (see Sec. 5.2).

Chapter 5

Feshbach resonances in ^{40}K

A. Ludewig[†], L. Cook, M.R. Goosen, T.M. Hanna, T.G. Tiecke,
U. Schneider, L. Tarruell, I. Bloch, T. Esslinger,
P.S. Julienne, S.J.J.M.F. Kokkelmans, and J.T.M. Walraven

This chapter is in preparation for submission.

We present a detailed study of magnetically tunable Feshbach resonances in ultracold ^{40}K binary collisions. We measured 26 not previously reported Feshbach resonances and compare these to the results of full coupled channel calculations (CC) as well as to two simplified theoretical models developed for the exploration of Feshbach spectra in binary mixtures: the three parameter multichannel quantum defect theory (MQDT) and the asymptotic bound-state model (ABM). Our results demonstrate the accuracy of simple theoretical models. The stability of the binary mixtures with respect to two-body losses is investigated theoretically.

5.1 Introduction

Since the first realization of a degenerate Fermi gas [DeM99a], experiments using ^{40}K have explored a wealth of ultracold physics. A crucial experimental achievement was the discovery of a magnetically tunable Feshbach resonance in ^{40}K [Lof02], which led to the formation of a molecular BEC [Gre03]. In optical lattices a Mott insulator of fermionic atoms was demonstrated [Jör08], which provides insights into the fermionic Hubbard Hamiltonian [Sch08]. A ^{40}K Feshbach resonance has been used to explore the physics of the BCS-BEC crossover [Ste08]. Further, ^{40}K was used to investigate resonant collisions and molecule formation near Feshbach resonances in mixtures with other

[†]The main contribution of this author to the paper presented here is the measurement and analysis of most of the experimental data.

atomic species such as ^{87}Rb [Sim03, Ino04, Fer06, Osp06a, Osp06c, Zir08a, Zir08b], and ^{6}Li [Wil08, Tie10b, Nai11, Wu11]. A gas of ultracold polar molecules was created by coherent transfer of Feshbach associated ^{40}K^{87}Rb molecules to the rovibrational ground state [Ni08, Osp10]. The studies on mixtures open up further promising avenues of research.

Magnetically tunable Feshbach resonances in ultracold gases of alkali metal atoms [Köh06, Chi10] are phenomena that facilitate many of the current experiments with quantum gases. They occur when colliding atoms with particular internal configurations are coupled to a near-degenerate state with a different internal configuration. The energy difference between the scattering threshold and the bare bound state can be adjusted by the application of a magnetic field. When the molecular state is degenerate with the threshold, the s-wave scattering length will diverge [Tay72]. However, identical fermions in the same internal state cannot undergo s-wave collisions due to the Pauli principle. In this case the p-wave scattering volume can be made to diverge due to the presence of a weakly-bound state. A crucial property of the Feshbach resonance is that the magnitude and sign of the scattering length can be adjusted at will. When a magnetic field B is present, we can define a collisional entrance channel in terms of the energy eigenstates of the asymptotically separated atoms.

For ^{40}K the single-atom energy levels of the electronic ground state are shown as a function of magnetic field in Fig. 5.1, with the states labeled $a, \ldots, r$ in order of increasing energy [Ari77]. A special feature of ^{40}K is the inverted hyperfine structure [Zac42]. This inversion has important consequences for spin-exchange relaxation in the presence of a magnetic field. Of the 45 different binary mixtures that can be created with atoms in the lowest hyperfine manifold 17 are stable against spin-exchange in the zero-temperature limit. These include all mixtures with atoms in adjacent hyperfine states as well as all binary mixtures with atoms in hyperfine states differing by two units of angular momentum because all exit channels are forbidden either energetically or by Pauli blocking. Consequently, all triple mixtures of ultracold atoms in three adjacent hyperfine states are stable against spin exchange in the presence of a magnetic field. Of these 17 mixtures stable against spin exchange only the $a + b$ mixture is fully stable. The lifetime of all other binary mixtures is limited by magnetic dipole-dipole relaxation. Feshbach resonances occur in all of these mixtures in collisions between atoms in different hyperfine states as well as in the same hyperfine state. Thus far, the observation of Feshbach resonances has been reported for the $a + b$ channel, the $b + b$ channel and the $a + c$ channel [Lof02, Reg03c, Tic04, Reg03a]. The large variety of mixtures stable against spin exchange stimulated us to make a broader exploration of Feshbach resonances in ^{40}K.

In this paper we explore Feshbach resonances in homonuclear mixtures of the fermionic quantum gas ^{40}K. Our results agree to within experimental error with coupled channels calculations using the best available potentials [Fal08]. We identify, both experimentally and theoretically, mixtures of different hyperfine states with special features in the properties of the Feshbach resonances. In Section 5.2 we discuss the experimental contributions and present the main results of this paper in Tables 5.1 and 5.2. We measured 26 not previously observed resonances, 12 s-wave and 14 p-wave resonances. In particular, we observed a 'well-isolated' s-wave resonance in the $c + d$ channel with a width of 8.7 G and separated by +55 G (attractive side) from the next resonance (p-wave) in the spectrum. In the $j + h$ channel we observed a

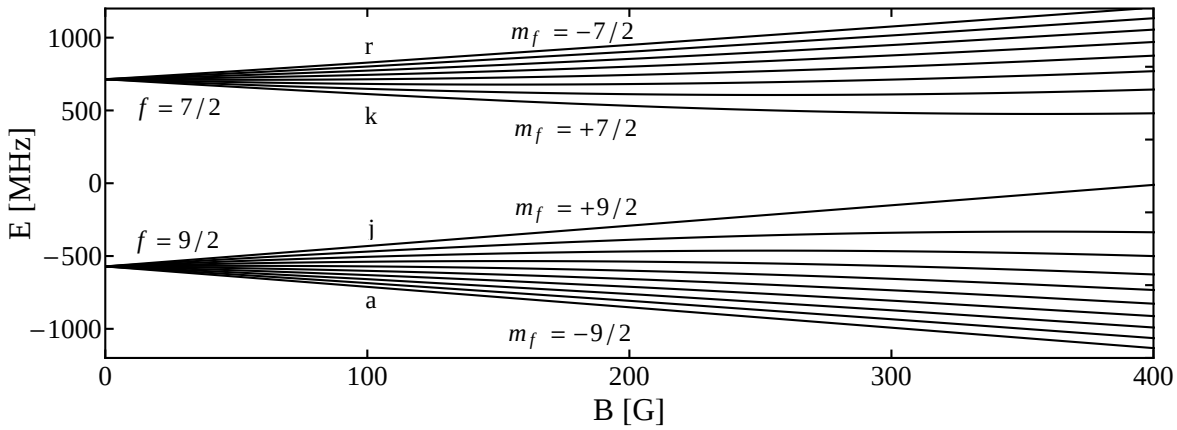

Figure 5.1: The energy eigenvalues of the single ^{40}K atom Zeeman and hyperfine Hamiltonian H_1 as a function of applied magnetic field (1 Gauss = 10^{-4} Tesla). We label the states from a to r in order of increasing energy. Also shown are the f and m_f quantum numbers that these states correspond to. An entrance channel labelled as $a + b$, for example, would correspond to a collision with the atoms initially in a state with appropriate symmetry, containing one atom in state a and one in state b [Chi10].

p-wave resonance with decay to the $i + i$ channel in which the atoms remain optically trapped. If this channel can be made elastic, for instance by rf dressing of the h level [Kau09, Pap10], it may be an interesting model system to study three fermion interactions. Further we observed four p-wave resonances where the magnetic dipole-dipole structure could be resolved [Tic04]. In Section 5.3 we discuss the theoretical side. We report on the performance of two simplified theoretical models developed for the exploration of Feshbach spectra in binary mixtures: in Section 5.3.2 we discuss the three parameter multichannel quantum defect theory (MQDT) [Han09] and in Section 5.3.3 the asymptotic bound-state model (ABM) [Tie10c]. The advantages and disadvantages of the simplified models are discussed in Section 5.3.4 and their performance is compared against the CC results. In Section 5.4 we present a summary and concluding remarks.

5.2 EXPERIMENTS

The experimental data in Tables 5.1 and 5.2 was obtained on different experimental setups in groups from Amsterdam [A], Munich [M] (previously in Mainz) and Zurich [Z], which all determined the resonance field locations B_0 via loss measurements. Data marked with [A] was measured in a three-dimensional optical dipole trap by observing the spin-dependent loss of atoms versus magnetic field, well-known since the pioneering experiment by the Ketterle group [Ino98]. Data marked with [M] and [Z] was taken in optical lattices. In Munich [M] the magnetic field width of the resonance, ΔB, was determined by investigating the crossover from ballistic to diffusive expansion in a blue-detuned optical lattice as a function of magnetic field [Sch10]. In Zurich ΔB was measured by observing the dephasing of Bloch oscillations in a red-detuned optical

Channel	M_T	Experiment B_0 [G]	ΔB [G]	ΔB_L [G]	Source	CC B_0 [G]	Δ [G]	$a_{\rm bg}/a_0$	$\delta\mu/h$ [MHz/G]	$a_{\rm res}/a_0$	γ_b [mG]
a + b	-8	202.10(7)[a]	7.0(2)[b]; 7.5(1)[c]		[a], M[b], Z[c]	202.1	6.9	167.0	0.2363	-	-
a + c	-7	224.21(5)[d]	9.7(6)[d]; 7.6(1)[e]		[d], Z[e]	224.2	7.2	167.3	0.2193	1.8×10^7	0.068
b + c	-6	174	7		[f]	174.3	7.9	183.5	0.0873	4.6×10^6	0.32
b + c	-6	228.8(4)		2.4(3)	A	228.7	8.2	137.6	0.1163	1.0×10^6	1.1
b + d	-5	168.5(4)			M	169.1	1.0	184.8	0.0810	9.5×10^4	2.0
b + d	-5	260.3(6)			M	260.5	11.2	164.9	0.1272	1.5×10^6	1.2
c + d	-4	22.1(3)		0.7(2)	A	22.44	0.065	166.3	1.0025	1.8×10^3	6.2
c + d	-4	178(1)		6(1)	A	178.3	8.7	185.6	0.0780	1.8×10^6	0.90
c + d	-4	254.8(9)		5(1)	A	255.1	15.7	139.8	0.0702	6.1×10^5	3.5
d + e	-2	37.2(3)		3.6(4)	A	38.07	0.37	157.8	0.5905	1.3×10^3	46
d + e	-2	102.1(1)		0.4(1)	A	102.24	0.0026	169.2	0.2455	2.8×10^1	16
d + e	-2	138.2(1)		1.1(1)	A	138.25	0.15	176.6	0.1620	1.3×10^3	2.0
d + e	-2	219.1(1)		3.5(5)	A	219.7	1.7	208.0	0.0885	7.3×10^4	4.8
d + e	-2	292.3(4)		11.5(2)	A	292.7	27.5	150.9	0.0613	9.4×10^5	4.4
i + h	6	312(1.8)		4(1.5)	A	312.4	6.6	129.9	0.4267	1.5×10^5	5.6

Table 5.1: Observed s-wave Feshbach resonances with accompanying coupled-channels (CC) — parameterization. The letters A, M, and Z indicate measurements performed in Amsterdam, Munich and Zurich, respectively. The widths ΔB_L reported from Amsterdam are the widths of the loss features. The CC parameterization were obtained by fitting to Eqs. (5.14a,5.14b), except for the $a + b$ channel where the scattering length is real and so the standard form $a_{\rm bg}[1 - \Delta B/(B - B_0)]$ is used. M_T is the total projection of angular momentum along the magnetic field axis, and is a conserved quantity during the collision. CC calculations were performed with an initial collision energy of $E/k_{\rm B} = 1$ nK. [a][Reg04], [b][Sch10], [c][Jör10b], [d][Reg03a], [e][Str10], [f][Reg06].

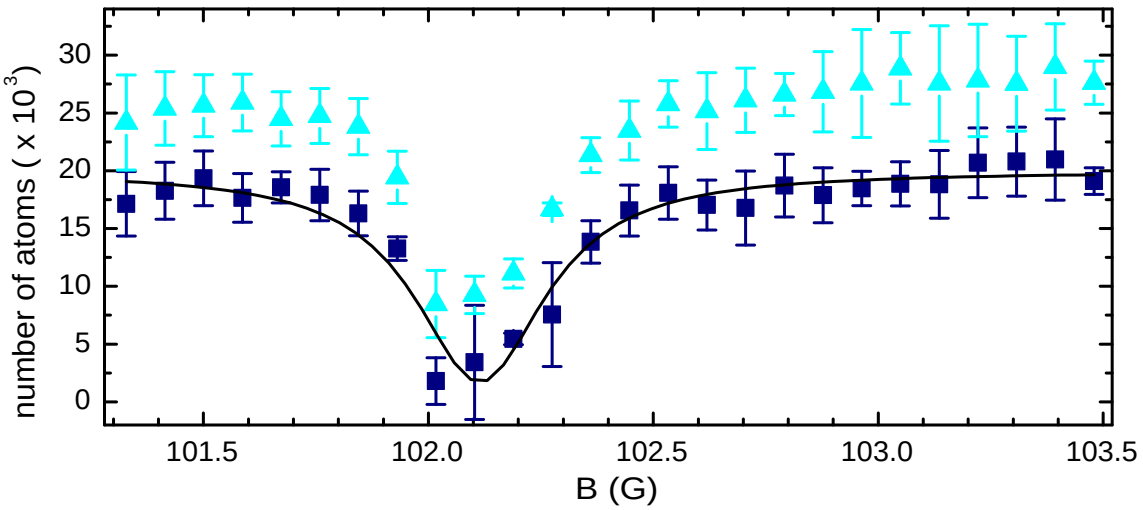

Figure 5.2: Determination of the field width of a loss feature around a s-wave resonance in ^{40}K. It is an expanded view of Fig. 5.4. The atom number in the two spin states (squares and triangles) is fitted with a Lorentz distribution (solid line). The center of the loss feature we take as B_0, the width as ΔB_L.

lattice, as was previously demonstrated for the bosonic case in Innsbruck [Gus08].

5.2.1 Experiments in Amsterdam

In Amsterdam the positions of the Feshbach resonances were determined as an increase in the atomic loss rate [Ino98]. To distinguish between losses in the different spin channels all measurements are done with state selective detection. We load about 10^6 atoms from a magnetic trap into a single pass optical dipole trap, created by focusing 1.9 W from a fiber laser ($\lambda = 1.07\,\mu$m) to a 19 µm waist acting as optical tweezers [Tie10b]. The transferred cloud consists of a mixture of atoms in the magnetically trappable spin states g, h, i, j in the notation of Fig. 5.1. Using the tweezers the cloud is moved into the center of a Feshbach coil producing the magnetic field for the measurements. As the cloud consists of fermions in different spin states it can be evaporatively cooled by reducing the intensity of the trapping light. The spin composition of the mixture is determined using the Stern-Gerlach method with typically 10^4 atoms at the final temperature of about 1 µK. We use for this purpose a magnetic field gradient of 100 G/cm, applied during the expansion after release from the optical trap. The gradient separates the different spin states, which are then detected at zero field using absorption imaging.

In view of the many states of the $f = 9/2$ ground state hyperfine manifold hundreds of Feshbach resonances can be observed. Therefore, to ensure a proper assignment of the Feshbach resonances, it is essential to prepare high purity binary mixtures of only the desired spin states. The spin state preparation is done in two steps: firstly, all atoms except those in the most populated state j are removed from the sample by a two photon cleaning process at an offset field of 7 G. With microwave sweeps the impurity states are

adiabatically transferred to the upper hyperfine manifold ($f = 7/2$) and subsequently removed by resonant light at the $^2S_{1/2}$, $f = 7/2 \rightarrow {}^2P_{3/2}$, $f = 5/2$ optical transition (D_2-line). Secondly, the desired states are populated by radio frequency transfers at an offset field of 18 G. We have not observed any heating of the cloud due to the spin preparation. The remaining density of the spin mixture is about $10^{12}\,\mathrm{cm}^{-3}$. After holding the atoms for $1-5$ s at a designated magnetic field, we switch off the Feshbach coil and apply a Stern-Gerlach pulse to determine the remaining fraction of atoms in each spin state using absorption imaging.

The positions B_0 and the widths ΔB_L of the measured loss features are listed in Tables 5.1 and 5.2. The loss feature of the 102.10 G $d+e$ resonance is shown in more detail in Fig. 5.2. This mixture is a good test bench for the approximate theories, which will be discussed in more detail in Section 5.3. We have observed symmetric as well as asymmetric loss profiles. The narrow and isolated s-wave resonances show a symmetric profile and are fitted with a Lorentz function to determine the position B_0 and the width ΔB_L of the loss feature caused by the Feshbach resonance.

The full width at half maximum (FWHM) of the loss features differs from the usual definition of the theoretical width [Chi10] and only serves as a qualitative indicator to characterize the observed feature. The actual loss rate as a function of magnetic field was not measured. The p-wave resonances and some of the broader s-wave resonances show an asymmetric profile. Here we report the position of the Feshbach resonance as the magnetic field where the biggest loss occurs. For the broader p-wave resonances we also resolve the doublet feature due to magnetic dipole-dipole interactions [Tic04]. The assignment to s- or p-wave resonances is simplified by state dependent detection: if only one spin state shows losses at a certain field, an s-wave resonance can be excluded in view of the fermionic nature of the atoms.

The narrowest resonances studied experimentally were the s-wave resonances at 22.1(3) G in the $c+d$ channel and at 102.10(9) and 138.21(9) G in the $d+e$ channel. The centres of the loss features (B_0) of the latter two resonances were found to agree within experimental error (100 mG) with CC calculations based on the Born-Oppenheimer potentials of Ref. [Fal08] (see Section 5.3.1). Further, we observed a 'well-isolated' s-wave resonance at $B_0 = 178(1)$ G in the $c+d$ channel, with a p-wave resonance as the nearest resonance separated by +55 G on the attractive side of the s-wave resonance. This resonance may prove valuable in applications where one aims at minimizing the elastic cross section by tuning to the zero crossing of the s-wave resonance (see sections 5.2.2 and 5.2.3). Another interesting resonance is the p-wave resonance at 44(2) G in the $j+h$ channel, where the $j+h \rightarrow i+i$ decay channel is close to elastic and the atoms in the i states remain trapped. If this channel can be made elastic, for instance by rf dressing of the h level [Pap10], it may be an interesting model system to study three-fermion interactions in the i, j, h mixture. The $i+i$ channel shows two p-wave resonances at small separation, each with the characteristic doublet structure due to magnetic dipole-dipole interactions [Tic04]. We obtain $B_0 = 43.8(2)$ G, $B_0 = 44.7(2)$ G and $B_0 = 45.2(2)$ G, $B_0 = 46.4(2)$ G, both for $|m_l| = 1$ and $|m_l| = 0$ respectively. The dipolar structure was also observed in $c+c$ and $d+d$ resonances.

5.2.2 EXPERIMENTS IN MUNICH

In Munich the widths of the Feshbach resonances are measured by observing the expansion of an $a+b$ mixture in a flat-bottom two-dimensional (2D) optical lattice [Sch10]. First, the atoms are harmonically confined in a red-detuned crossed beam optical dipole trap, where typically $2\times10^5-3\times10^5$ atoms are evaporatively cooled to temperatures of $T/T_F=0.13(2)$, where T_F is the Fermi temperature. Subsequently, a band-isolating state is prepared by ramping up a three-dimensional (3D) simple-cubic blue-detuned optical lattice with a depth of $8E_R$, where $1E_R=h^2/(2m\lambda^2)$ is the recoil energy, with m the atomic mass and $\lambda=738\,\mathrm{nm}$ the wavelength of the lattice light corresponding to a $\lambda/2=369\,\mathrm{nm}$ lattice spacing. By lowering the power of the red-detuned trap to about 10% of its initial power, the dipole potential is adjusted to compensate for the anti-confinement of the lattice, thus flattening the bottom of the optical lattice potential and allowing the atom cloud to expand in 3D. By increasing the vertical lattice to a depth of $20E_R$ vertical tunneling of the atoms is suppressed and the expansion can be studied under quasi-2D confinement without the influence of gravity.

The loading procedure results in a well-known density distribution of the atoms with Gaussian core radius R_0 which is independent of the interactions between the atoms [Sch10]. The core expansion velocity v_c depends on the interaction between the atoms and is varied from noninteracting to strongly interacting by varying the scattering length from zero ($a=0$) to a very large value ($a\to\infty$) with the aid of the Feshbach resonance at 202 G. In the non-interacting limit the expansion shows the characteristic ballistic behavior of an ideal band insulator. In the presence of interactions the core expansion velocity v_c is reduced by diffusive motion under the influence of collisions. To determine v_c we measure the core radius versus time with phase-contrast imaging, using the scaling function

$$R_c(t)=\sqrt{R_0^2+v_c^2t^2}. \tag{5.1}$$

Within experimental error this function was found to describe the expansion for all interaction strengths investigated. Around the zero crossing of the Feshbach resonance ($a=0$) the expansion velocity $v_c(B)$ shows a pronounced peak as a function of magnetic field. From the position of the peak we determine the zero crossing of the $a+b$ resonance at $B(a=0)=209.1(2)$ G. The center of the resonance B_0 was determined by measuring the loss feature in a similar fashion as in Amsterdam (see Section 5.2.1). We obtained $B_0=202.1$ G, which implies that the width of the resonance equals $\Delta B=7.0(2)$ G. The accuracy of these measurements is limited by the magnetic field calibration. The uncertainties in determining the expansion velocities are much smaller. The vicinity of the p-wave resonance in the $b+b$ channel at 198.8 G can give rise to some broadening and shift of the function $v_c(B)$. Therefore, for measurements of the crossover from ballistic to diffusive expansion in an optical lattice an interesting alternative is offered by the s-wave resonance at $B_0=178$ G in the $c+d$ channel, well-separated by 55 G from the p-wave resonance in the $c+c$ channel at $B_0=233$ G.

5.2.3 EXPERIMENTS IN ZURICH

In Zurich we determined the zero-crossing of the scattering length $a(B)$ through the observation of Bloch oscillations in an optical lattice as a function of magnetic field. At

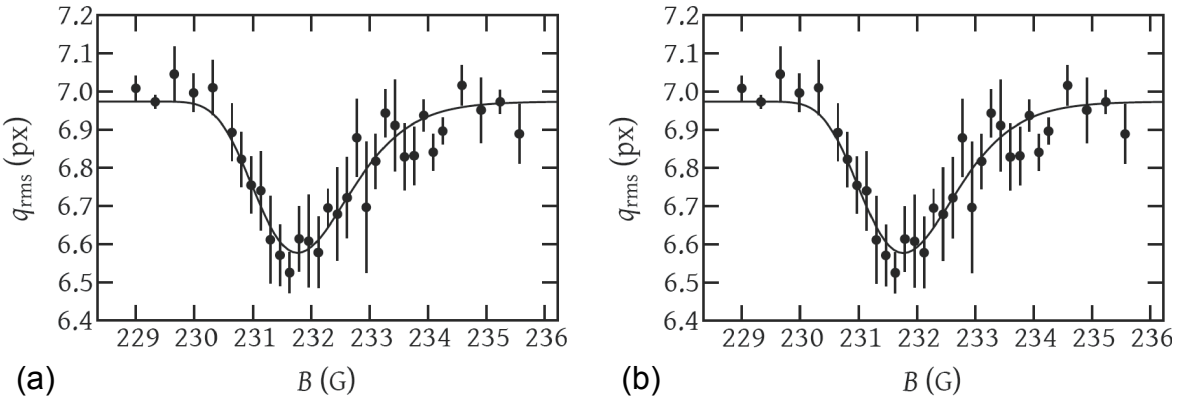

Figure 5.3: Suppressed dephasing of Bloch oscillations at the zero crossing of the scattering length. In the $a + c$ and $a + b$ mixtures ((a) and (b) respectively), the root mean square momentum width q_{rms} in units of camera pixels shows a characteristic dip when the interactions vanish at the zero crossing of the scattering length. Figure extracted from [Jör10a].

vanishing interactions these oscillations can be maintained for many thousand cycles. A small amount of interaction, however, already leads to collisions and to the dephasing of oscillations of different atoms. Thus, the dephasing of Bloch oscillations constitutes an excellent observable for locating the zero crossing, as demonstrated in [Gus08] for the bosonic case. Combined with an independent measurement of the resonance position, it can be used to determine the resonance width. The starting point of this experiment is a degenerate Fermi gas of typically 2×10^4 atoms loaded in a one-dimensional optical lattice of depth $5E_R$, where E_R is the recoil energy. We limit the filling in the band, since the fermionic nature of the atoms would otherwise lead to a complete occupation of the entire Brillouin zone (band-insulating state) and prevent the observation of the oscillations.

After excitation, the atoms are allowed to oscillate for up to 750 ms, and this for different values of the offset magnetic field. We then measure the quasi-momentum distribution after a time-of-flight expansion. A moment is chosen where the atoms are left at the band center after the oscillation. There, $a = 0$ corresponds to the smallest measured root mean square (rms) momentum spread. Fig. 5.3 shows the experimental results. Using the literature values for B_0 [Lof02, Reg04, Reg03a, Reg03b] and the background scattering length $a_{\mathrm{bg}} = 174a_0$, with $a_0 = 0.0529$ nm the Bohr radius, we fit a Gaussian dip to the rms momentum width:

$$q_{\mathrm{rms}}(B) = q_0 + \Delta q \exp\left[-\frac{1}{2}\left(\frac{a_{\mathrm{bg}}}{\Delta a}\right)^2\left(1 - \frac{\Delta B}{B - B_0}\right)^2\right]. \tag{5.2}$$

The four remaining parameters are determined by the fit: q_0, the rms momentum for dephased oscillations, Δq, the maximum change in rms momentum without interactions, Δa, the width of the low dephasing regions around $a = 0$. We obtain $\Delta B = 7.5(1)$ G for the $a + b$ resonance at 202.1 G and $\Delta B = 7.6(1)$ G for the $a + c$ resonance at 224.21(5) G. The accuracy is limited by the magnetic field calibration,

the uncertainty of the resonance position and the width of the dip. Compared to experimental values obtained at JILA [Reg03a], the width of the $a + c$ resonance differs. However, it is consistent with the value of the on-site-interaction U extracted from lattice modulation spectroscopy in a three-dimensional optical lattice [Jör10b]. Additionally we have observed a previously unreported p-wave Feshbach resonance in the $c + c$ channel which shows the characteristic doublet feature due to magnetic dipole-dipole interactions [Tic04]. We obtain $B_0 = 232.8(2)$ G and $B_0 = 233.4(2)$ G for $|m_l| = 1$ and $|m_l| = 0$ respectively. Here m_l is projection of the orbital angular momentum on the magnetic field axis. The assignment of the loss features to a p-wave resonance is confirmed by the suppression of either the $|m_l| = 0$ or the $|m_l| = 1$ resonance when the experiments are realized in a one-dimensional geometry, depending on the relative orientation of the magnetic field axis and the extension of the gas [Gün05].

		Experiment		CC
Channel	M_T	B_0 [G]	Source	B_0 [G]
a + c	-7	215(5)	M	215.0
b + b	-6, -8	198.30(2)	[Gae07]	198.4
b + b	-7	198.80(5)	[Gae07]	198.9
c + c	-4,-6	232.8(2) [Z]; 232.8(2) [A]	Z/A	233.0
c + c	-5	233.4(2) [Z]; 233.6(2) [A]	Z/A	233.6
c + c	-5	245.3(5) [M]; 245.4(4) [A]	M/A	245.0
c + d	-3,-5	262.2(2)	A	262.2
c + d	-4	262.6(2)	A	262.5
d + d	-3	287(1.8)	A	287.6
d + d	-3	311.8(4)	A	311.8
d + e	-2	338(1.8)	A	338.4
e + e	-1	373(1.8)	A	373.7
h + h	5	68(1.8)	A	67.6
h + h	5	102(1.8)	A	100.2
h + h	5	139(1.8)	A	138.0
h + h	5	324(1.8)	A	323.1
h + j	7	44(1.8)	A	44.6
i + i	6,8	43.8(2)	A	43.6
i + i	7	44.7(2)	A	44.9
i + i	6,8	45.2(2)	A	45.3
i + i	7	46.4(2)	A	46.4

Table 5.2: Observed p-wave Feshbach resonances with accompanying coupled-channels (CC) parameterizations. The letters A, M, and Z refer to measurements performed in Amsterdam, Munich and Zurich, respectively. M_T is the total projection of angular momentum along the magnetic field axis, for each collision channel it can take on three values corresponding to different projections of the orbital angular momentum quantum number $m_l = 0, \pm 1$. CC calculations were performed at an initial collision energy of $E/k_\mathrm{B} = 1$ μK. This accounts for the discrepancy between the calculated positions in the $b + b$ channel with Ref. [Gae07] where effort was made to account for the temperature dependence.

5.3 Theoretical models

In this Section we discuss the coupled-channels (CC) method which is used to accurately describe the two-body interactions of ultracold potassium atoms. The CC method allows for a precise characterization of all the measured Feshbach resonances. The results are included in Tables 5.1 and 5.2 for comparison with experiment. Additionally, the CC method is used to test the validity of two simplified models of resonance scattering: The asymptotic bound-state model (ABM) and multichannel quantum defect theory (MQDT). Each of these two approaches represents a different method of simplifying the problem of searching for and characterizing Feshbach resonances and molecular states. The corresponding features and limitations will be discussed.

5.3.1 Coupled channels calculations

Numerical solution of the CC equations and specifically their application to cold gases have been discussed widely [Joh73, Sto88, Hut94, Mie96]. Here we give an overview of what is involved to solve the CC equations. As input for the newly written CC code, which was implemented in the MATLAB programming language, we use the Born-Oppenheimer (BO) potentials of Ref.‘ [Fal08]. The combination of calculation and experiment showed that it was not necessary to fine-tune these BO potentials, i.e. the BO potentials are accurate enough to properly describe the scattering of ultracold potassium atoms. The obtained numerical results are used to characterize atomic two-body loss rates and resonance parameters, which are presented in Tables 5.1 and 5.2. The inelastic collision rate in the vicinity of a resonance is also of interest as it is related to the longevity of an experiment.

In the center of mass frame [Tay72] the Hamiltonian for two alkali metal atoms in the presence of a magnetic field $\mathbf{B}$, is given by

$$\mathcal{H} = \frac{\mathbf{p}^2}{2\mu} + \mathcal{H}^{\mathrm{int}} + V + V^{\mathrm{ss}}, \tag{5.3}$$

where the first term represents the relative kinetic energy with the reduced mass μ. The two-body internal energy $\mathcal{H}^{\mathrm{int}}$ is determined by the Zeeman and hyperfine interactions for each atom j

$$\mathcal{H}^{\mathrm{int}} = \sum_{j=1}^{2} \left(\frac{a_{\mathrm{hf}}}{\hbar^2} \mathbf{s}_j \cdot \mathbf{i}_j + \mu_{\mathrm{B}} (g_{\mathrm{e}} \mathbf{s}_j + g_{\mathrm{n}} \mathbf{i}_j) \cdot \mathbf{B} \right). \tag{5.4}$$

The hyperfine constant a_{hf} gives the magnitude of the hyperfine splitting as seen in Fig.‘ 5.1; $\mathbf{i}_j$, $\mathbf{s}_j$, μ_{B}, g_{n}, g_{e} are the nuclear spin of atom j, electronic spin of the valence electron of atom j, Bohr magneton, nuclear g-factor, and electronic g-factor respectively. The term $V = \mathcal{P}_{\mathrm{s}} V_{\mathrm{s}} + \mathcal{P}_{\mathrm{t}} V_{\mathrm{t}}$ includes the singlet V_{s} and triplet V_{t} BO potentials [Fal08] with the operators $\mathcal{P}_{\mathrm{s}}$ and $\mathcal{P}_{\mathrm{t}}$ projecting out the singlet and triplet components of the wave function respectively. The spin-spin dipole interaction is described by

$$V^{\mathrm{ss}} = \frac{\alpha^2 E_{\mathrm{h}} a_0^3}{\hbar^2 r^3} \left[\mathbf{s}_1 \cdot \mathbf{s}_2 - 3(\mathbf{s}_1 \cdot \hat{\mathbf{r}})(\mathbf{s}_2 \cdot \hat{\mathbf{r}}) \right], \tag{5.5}$$

which is the long range approximation to the interaction between the magnetic moments of the outer shell electrons belonging to each of the alkali metal atoms, as

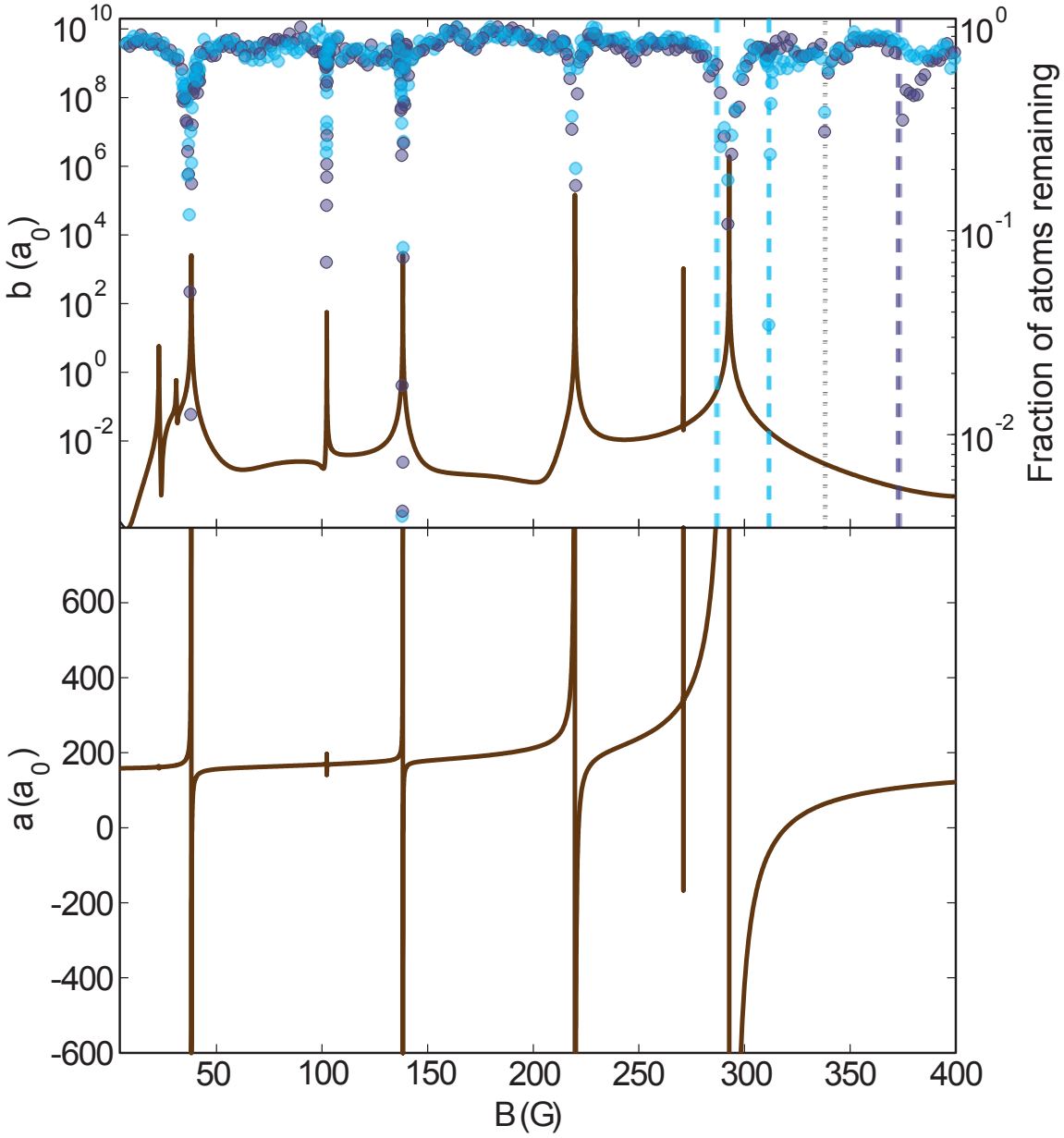

Figure 5.4: Observation of ^{40}K Feshbach resonances by loss spectroscopy of the $d + e$ mixture. Upper plot, right y-axis: Atoms remaining in the trap after the cloud had been held for 3 s at magnetic field B. Light blue circles denote atoms in the d state, dark blue circles denote atoms in the e state. Left y-axis: The solid line is the imaginary part of the scattering length and is proportional to the inelastic collision rate for two-atom collisions. The vertical lines indicate the positions of some p-wave resonances: light blue dashed being in the $d + d$ channel, black dotted the $d + e$ channel, and dark blue dashed the $e + e$ channel. Lower plot: The solid line is the real part of the scattering length a_s.

discussed in Ref.' [Sto88]. Here $\hat{\mathbf{r}}$, E_h, and α are the interatomic separation, Hartree energy, and fine structure constant respectively.

Starting from the rigorous multichannel scattering theory it is possible to derive the coupled-channels equations in the close-coupling approximation [Tay72, New66]. Hereby we express the wave function in terms of the N (channel) states $|\sigma_m\rangle$, that diagonalize the Hamiltonian $\mathcal{H}^\mathrm{int}$ and have the correct symmetry,

$$\frac{1}{r}\sum_{m=1}^{N}|\sigma_m\rangle\psi_m(r). \tag{5.6}$$

The radial Schrödinger equation can now be projected on the channel states which yields N equations

$$\frac{\partial^2\psi_m}{\partial r^2} = \frac{2\mu}{\hbar^2}\sum_{n=1}^{N}\left[W_{m,n}(r) + V^\mathrm{ss}_{m,n} - E\delta_{m,n}\right]\psi_n(r) \tag{5.7}$$

where $\delta_{m,n}$ is the Kronecker delta and

$$W_{m,n}(r) = \delta_{m,n}\left[E_n + \frac{\hbar^2}{2\mu}\frac{l_n(l_n+1)}{r^2}\right] + V_{m,n}. \tag{5.8}$$

Here E_n is the eigen-energy of the internal Hamiltonian $\mathcal{H}^\mathrm{int}$ and l_n is the relative orbital angular momentum quantum number of the state $|\sigma_n\rangle$. It is useful to rewrite this set of equations in the $N\times N$ matrix form

$$\mathbf{\Psi}''(r) = \left[\mathbf{Q}(r) + \mathbf{V}^{ss}(r)\right]\mathbf{\Psi}(r), \tag{5.9}$$

where the elements of the matrix $\mathbf{Q}(r)$ are given by $(2\mu/\hbar^2)[W_{m,n}(r) - E\delta_{m,n}]$. Considering the scattering boundary condition (i.e. $r\to\infty$), $[\mathbf{\Psi}]_{\{1,\ldots,N\},m}$ can be interpreted as being the scattering wave function with an incoming wave in channel m. In practice, rather than propagating the wave function and derivative matrices to large r, we instead propagate the log-derivative matrix $\mathbf{Y} = \mathbf{\Psi}'[\mathbf{\Psi}]^{-1}$ using the technique of Manolopoulos [Man86]. With this in mind a multichannel S matrix can be extracted via [Tay72]

$$\mathbf{S}(r) = \left[\mathbf{Y}(r)\mathbf{h}^{(1)}(r) - \mathbf{h}'^{(1)}(r)\right]^{-1}\times\left[\mathbf{h}'^{(2)}(r) - \mathbf{Y}(r)\mathbf{h}^{(2)}(r)\right], \tag{5.10}$$

where $[\mathbf{h}^{(1,2)}(r)]_{m,n} = -\delta_{m,n}\sqrt{k_n}ir h^{(1,2)}_{l_n}$ are diagonal matrices with $h^{(1)}_{l_n}$ and $h^{(2)}_{l_n}$ representing spherical Hankel functions of the first and second kind. The asymptotic magnitude of the momentum in channel $|\sigma_n\rangle$ equals $\hbar k_n = \sqrt{2\mu(E-E_n)}$. For non-$s$-wave entrance channels the numerical propagation becomes difficult at low collision energies. We find it necessary to use the long range approximate correction to the S matrix given by [Sto88]

$$\mathbf{S}(\infty)\approx\mathbf{S}(r_1) - i\frac{\mu}{\hbar^2}\int_{r_1}^{\infty}\left\{\left[\mathbf{h}^{(2)}(r) + \mathbf{S}(r_1)\mathbf{h}^{(1)}(r)\right]\times\mathbf{V}^\mathrm{ss}(r)\left[\mathbf{h}^{(2)}(r) + \mathbf{h}^{(1)}(r)\mathbf{S}(r_1)\right]\right\}\mathrm{d}r \tag{5.11}$$

in order to greatly increase the rate of convergence. This expression assumes that r_1 is large enough to neglect contributions from V, which fall off as r^{-6}. The integration

in this expression is performed analytically. We only include open channels in this correction.

Although we have thus far formulated the problem using $|\sigma_i\rangle$, it is also useful to employ an alternative set of angular momentum states. In the inner region, where the singlet and triplet potentials are dominant, we use a basis in which $\mathbf{i}_1$ and $\mathbf{i}_2$ are coupled to give $\mathbf{I}$, and $\mathbf{s}_1$ and $\mathbf{s}_2$ are coupled to give $\mathbf{S}$. This has the advantage of the BO contribution V being diagonal. We perform the basis transformation to the basis states $|\sigma_m\rangle$ at the internuclear distance where the energy difference $|V_\mathrm{t} - V_\mathrm{s}|$ is large compared to the atomic hyperfine coupling.

Once an S matrix has been evaluated one can extract the s-wave scattering length by defining the phase shift $\delta(E)$, related to the element of the S matrix $[\mathbf{S}]_{e,e} = \exp[2i\delta(E)]$, with e indicating the entrance channel. If the entrance channel is the only open channel the scattering length is given by the limiting process

$$a = \lim_{k\to 0} \frac{-\tan[\delta(E)]}{k}. \tag{5.12}$$

This can be generalized to the case where the scattering is not purely elastic; i.e., there is more than one open channel. Here the complex scattering length $\tilde{a}$ and complex phase shift $\delta(E)$ are now related by

$$\tilde{a} = a - bi = \lim_{k\to 0} \frac{-\tan[\delta(E)]}{k}. \tag{5.13}$$

It can be shown, see Refs. [Nai11, Hut07, Boh99, Fed96], that in the vicinity of a Feshbach resonance the following parameterization is valid

$$a(B) = a_\mathrm{bg}\left(1 - \frac{\Delta B(B-B_0)}{(B-B_0)^2 + (\gamma_B/2)^2}\right), \tag{5.14a}$$

$$b(B) = 2a_\mathrm{res}\frac{(\gamma_B/2)^2}{(B-B_0)^2 + (\gamma_B/2)^2}. \tag{5.14b}$$

In these expressions, a_bg is the background scattering length, representing the scattering length of the entrance channel in the absence of a resonance. We have expressed the decay rate of the bound state, γ [Köh05], in magnetic field units, $\gamma_B = \hbar\gamma/\mu_\mathrm{res}$, where μ_res is the difference in magnetic moment between the entrance channel and the bound state causing the resonance. The resonance length a_res is defined by $a_\mathrm{res} = a_\mathrm{bg}\Delta B/\gamma_B$ and characterizes the strength of a resonance. The width and the center of the resonance are given by ΔB and B_0, respectively. The real part of the complex scattering length $\tilde{a}$ is still the appropriate parameter to describe the elastic scattering process, while the imaginary part can be used to describe the inelastic collision rate coefficient for channels with two atoms in different spin states

$$K_2(B) = \frac{4\pi\hbar}{\mu} b(B). \tag{5.15}$$

In the limit of zero collisional energy this rate has its peak exactly on resonance where it equals $K_2(B_0) = 8\pi\hbar a_\mathrm{res}/\mu$. In a thermal gas at $k_\mathrm{B}T \gg \gamma_B$ the rate drops rapidly with temperature, $K_2(B_0) \propto T^{-2}$. For partial densities n_α and n_β the total decay rate of component α is given by $-\dot{n}_\alpha/n_\alpha = K_2 n_\beta + \tau_\mathrm{vac}^{-1}$, where τ_vac is the vacuum

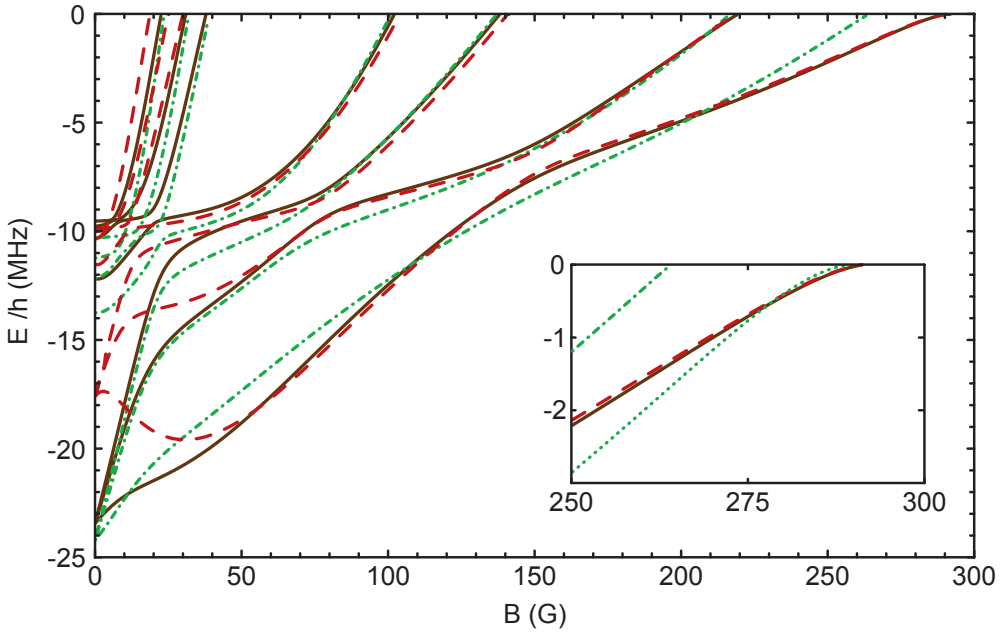

Figure 5.5: (Color online) Energy spectrum of s-wave molecular levels of ^{40}K in the $d+e$ channel. Energies are given relative to the $d+e$ threshold. The binding energies were obtained using: the CC method (black line), the MQDT (red dashed line), and the ABM (green dot-dashed line). The inset shows the binding energies near the broad resonance around $B \simeq 290$ G. For the MQDT and ABM the optimized parameters were used as input. The results for ABM are shown without the *dressing* of the bound state [Tie10c], except in the inset (green dotted line).

lifetime. Some results of the CC calculation for the real and imaginary parts $a(B)$ and $b(B)$ of the scattering length are shown for the $d+e$ mixture in Fig.‘ 5.4, where they can be compared to experimental findings. For all observed s-wave resonances the calculated values for B_0, ΔB, $a_{\rm bg}$, $a_{\rm res}$, γ_B and $\mu_{\rm res}$ were obtained for a collision energy $E/k_{\rm B} = 1$ μK and are tabulated in Table 5.1. For the p-wave resonances the collision energy was $E/k_{\rm B} = 1$ μK and only the position B_0 of the resonance center is tabulated.

The bound state calculations are performed as in Ref. [Hut94]. They involve numerical methods similar to those used for the scattering calculations. However the asymptotic $r \to \infty$ boundary condition on $\mathbf{\Psi}(r)$ now requires that all elements decay suitably to zero. The term $\mathbf{V}^{\rm ss}(r)$ is neglected in the bound state calculations because they are used for comparison to the MQDT and the ABM (see Fig.‘ 5.5), neither of which include this term. We propagate $\mathbf{Y}(r)$ from small r outwards to some matching point R, which we call $\mathbf{Y}_a$. We then propagate from large r inwards to R which we call $\mathbf{Y}_b$. It can be shown that a bound state exists if the matching matrix

$$\mathbf{M}(E) = \mathbf{Y}_a - \mathbf{Y}_b \tag{5.16}$$

has an eigenvalue equal to zero.

5.3.2 Multichannel quantum defect theory

The MQDT [Han09] is a scattering theory approach, incorporating two simplifying assumptions based on the separation of scale between the kinetic energy of the colliding atoms and the depth of the interatomic potential. Firstly, a pure van der Waals potential is used. We analytically solve the radial Schrödinger equation with this potential, using a powerful set of tools developed by Gao (see Ref.' [Gao05] and references therein). This saves the computational effort of propagating either the wave function or its log-derivative to large distances. Secondly, the physics occurring at small r is accounted for by an energy-independent boundary condition (a 'quantum defect') given in terms of the singlet and triplet scattering lengths [Gao05]. Matching the energy dependent solutions of the van der Waals potential to the short range boundary condition allows scattering and bound state properties to be predicted based on just three parameters describing the interactions: the scattering length of the singlet a_s and triplet a_t potential and the dispersion coefficient C_6 which describes the van der Waals tail of the interaction.

We have applied our model to calculations in the presence of a magnetic field [Han09] and RF radiation [Kau09, Han10]. We also note Gao's earlier work on collisions of alkali atoms at zero magnetic field [Gao05]. In the present work, an MQDT search over all possible collision channels was used as a guide for the CC calculations. The singlet and triplet scattering lengths were allowed to vary slightly from their actual values to optimize the fit to known resonances. This offsets the main error introduced by the above approximations: that deeper bound states are less accurately reproduced by the approximate potential.

We have calculated the Feshbach resonances using the most recent literature values given in Ref.' [Fal08] ($a_\mathrm{s} = 104.41\ a_0$, $a_\mathrm{t} = 169.67\ a_0$ and $C_6 = 3925.9\ E_h a_0^6$), which we will refer to as the physical parameters. The data, presented in Table 5.3, has an rms deviation for the resonance locations of 17.4 G, with a systematic offset towards the low field side. By using a_s and a_t as fit parameters, we reduce the rms deviation to 2.6 G, obtaining final fit parameters of $a_\mathrm{s}^\mathrm{fit} = 101.88\, a_0$ and $a_\mathrm{t}^\mathrm{fit} = 165.41\, a_0$. Data for the $d+e$ s-wave channel, optimized in this manner, is shown in Fig.' 5.5. The three lowest-field s-wave resonances in the $d + e$ channel arise from a deep bound state belonging to a higher collision threshold. Consequently, non-C_6 terms of the potential are more significant, and the MQDT calculation has a larger error than it does for the other resonances shown. Based on our s-wave fit, we calculate several p-wave resonances, listed in Table 5.4. With the exception of two outlying points in the $h + h$ channel, we reproduce the CC results well. We note that it is possible to obtain a much better fit when considering only resonances created by shallow bound states. This illustrates that the freedom given by the two fit parameters can only offset some of the errors introduced by making our approximations.

5.3.3 Asymptotic bound state model

The ABM [Tie10c] uses only bound states to calculate Feshbach resonance positions and widths. This approach allows accurate prediction of the resonances based on simple matrix operations, without solving the radial Schrödinger equation. As in the MQDT approach, it is sufficient to use as inputs a_s, a_t and C_6. From these, we use the accu-

mulated phase method [Ver09] to calculate binding energies ϵ_ν^S and overlap parameters $\langle\psi_{\nu'}^{S'}|\psi_\nu^S\rangle$, where ν, ν' range over all contributing bound states of the singlet and triplet potentials. Here ν is counted from the dissociation limit, i.e. $\nu = -1$ is the least bound state. Since the initial application of the ABM to the mixture of ^{6}Li-^{40}K [Wil08], it has been successfully applied in its original form by other groups on a variety of systems [Li08, Voi09, Deh10, Kno11], and extended to include dipole-dipole interactions [Goo10], overlapping resonances [Goo10], and RF-induced resonances [Tsc10]. Here, we describe an extension to the ABM which makes it applicable to systems with a large background scattering length.

Ultracold scattering in the entrance channel, in the absence of Feshbach resonances, is well described by $a_{\rm bg}$. This scattering length will depend on the energy $\epsilon_{\rm bg}$ of the least bound state of the background interaction potential. When the background scattering length is non-resonant, this least bound state is not energetically near the threshold of the channel. As in this case the effect of the scattering states on this bound state is small, the ABM accurately gives $\epsilon_{\rm bg}$. This changes when the background scattering length becomes resonant, i.e. the background scattering length is much larger than the range of the interaction potential ($a_{\rm bg} \gg r_0$), as occurs in relevant collision channels of ^{40}K. In such a system, the entrance channel supports a bound state close to threshold. The effect of these scattering states on the bound state (which cannot be neglected) can be incorporated into the ABM by effectively correcting the coupling of the least bound singlet and triplet states via their overlap parameter $\langle\psi_{-1}^0|\psi_{-1}^1\rangle$. To determine this correction we use the degenerate internal states (DIS) approximation [Sto88]. Within this approximation $a_{\rm bg}$ can be deduced from a simple decomposition of the entrance channel $|\sigma_e\rangle$ into singlet and triplet admixtures,

$$a_{\rm bg}^{\rm DIS} \simeq \langle\sigma_e|a_{\rm s}\ P_{\rm s} + a_{\rm t}\ P_{\rm t}|\sigma_e\rangle. \tag{5.17}$$

The energy of the least bound state of the entrance channel potential, which effectively includes the coupling to scattering states, can now be obtained from

$$\epsilon_{\rm bg}^{\rm DIS} \simeq -\frac{\hbar^2}{2\mu(a_{\rm bg}^{\rm DIS} - r_0)^2}\,. \tag{5.18}$$

where the range of the potential is taken to be the van der Waals length $r_0 = (\mu C_6/8\hbar^2)^{1/4}$. Equation (5.18) is only accurate when $a_{\rm bg}^{\rm DIS} \gg r_0$. By varying $\langle\psi_{-1}^0|\psi_{-1}^1\rangle$ with magnetic field such that $\epsilon_{\rm bg} = \epsilon_{\rm bg}^{\rm DIS}$, we effectively determine the correct singlet-triplet coupling of the least-bound states in the presence of nearby scattering states. The resulting magnetic field dependent overlap $\langle\psi_{-1}^0|\psi_{-1}^1\rangle(B)$ is used as input for the usual ABM calculations. Note that the range variation of the overlap parameter is a few percent, which corresponds to a shift of $\epsilon_{\rm bg}$ of a few MHz. The ABM can readily output quantum numbers of bound states and can be generalized to more accurate potentials.

We calculate the s-wave Feshbach resonances using the physical values of $a_{\rm s}$, $a_{\rm t}$ and C_6 as given in the previous section. The resonance values are shown in Table 5.3. Considering that the ABM uses only bound states and just three input parameters, the agreement with the coupled channels calculations is quite satisfactory. The initial fit has an rms deviation from the CC s-wave resonance positions of 16.4 G. Performing a least-squares fit by slightly varying the overlap parameters and the ϵ_{-2}^1 binding energy

gives better agreement, yielding an rms deviation for the resonance positions of $\sigma \simeq 6.9\,\mathrm{G}$. The bound states produced by this fitted calculation are shown in Fig.‘ 5.5.

For the p-wave resonances the background scattering is non-resonant. Therefore, we calculate the p-wave resonances using ABM in its original form, using magnetic field independent overlap parameters. We fit the resonance positions by varying only the $\langle\psi^0_{-2}|\psi^1_{-2}\rangle$ overlap parameter and the binding energy ϵ^0_{-2}. The other binding energies and overlap parameters are kept fixed to the values obtained from the accumulated phase method. The rms deviation on the fit is $\sigma \simeq 6.3\,\mathrm{G}$ and the resonances are shown in Table 5.4.

5.3.4 Comparison of MQDT and ABM

MQDT and the ABM have both previously been applied to the ^{6}Li-^{40}K [Wil08, Tie10b, Nai11] and ^{40}K-^{87}Rb [Han09, Tie10c] mixtures, which allow for some indirect comparison. Here we present an explicit comparison of the two models for the more complex case of ^{40}K-^{40}K. We compare the results of the two models to the results of the CC calculation which are summarized in Tables 5.3 and 5.4 and shown in Fig.‘ 5.5. The results obtained by using physical parameters (i.e. literature values) are shown in the middle columns of Table 5.3. MQDT has the slightly higher rms deviation from the CC results compared to the ABM, consistently producing B_0 values that are too low. As the qualitative agreement is good for both models, they can both be used for guiding more accurate coupled channels calculations, or providing quick feedback between theory and experiment. The fitted results of each model are also shown in Table 5.3. Here the MQDT approach produces a significantly lower rms deviation from the CC results compared to the ABM.

In optimizing the MQDT model to the CC data we varied only a_s and a_t, while keeping C_6 constant. For fitting the ABM we varied the binding energies and wave function overlaps, yielding effectively eight free parameters. However, in both the s- and p-wave cases one overlap parameter was dominant in obtaining a good fit. For the s- and p-wave fits the most relevant overlap parameters were $\langle\psi^0_{-1}|\psi^1_{-2}\rangle$ and $\langle\psi^0_{-2}|\psi^1_{-2}\rangle$, respectively. Both of these elements involve the $\nu = -2$ states. This indicates that either non-C_6 components of the potential are becoming significant, as is the main limiting factor for the MQDT approach, or that deeper bound states should be taken into account in the ABM. Despite the simplification of neglecting scattering states, good qualitative agreement is obtained for the resonance widths with the ABM. With the scattering approach of MQDT, we also obtain good qualitative agreement with the CC results. However, quantitatively we find that the MQDT and the ABM are limited in their accuracy for predicting the widths of Feshbach resonances. Resonance widths depend on the difference between the singlet and triplet potentials, which both theories only include crudely by assigning each potential the appropriate scattering length. Next we consider molecular bound-state manifolds obtained via MQDT and ABM and compare these to CC calculations. We consider the s-wave $d + e$ channel which, within the range of 300 Gauss, contains 7 resonances. Two of these resonances were too narrow to be observed experimentally. As this channel contains both wide and narrow resonances it very suitable for a comparison of the simplified models with respect to the CC results. The results of the comparison, where we used the optimized

Channel	CC		Physical parameters MQDT		Physical parameters ABM		Optimised parameters MQDT		Optimised parameters ABM	
	B_0 (G)	Δ (G)	B_0 (G)	Δ (G)	B_0 (G)	Δ (G)	B_0 (G)	Δ (G)	B_0 (G)	Δ (G)
a + b	202.1	6.9	187.1	7.3	205.8	4.7	201.2	7.1	207.1	6.8
a + c	224.2	7.2	208.2	7.6	227.9	5.1	223.3	7.4	229.1	7.1
b + c	174.3	7.9	157.0	8.8	197.7	2.2	173.8	8.4	177.8	3.0
b + d	169.1	1.0	156.9	1.5	181.3	0.3	171.9	1.3	169.3	0.6
b + d	260.5	11.2	242.8	11.6	261.7	9.2	260.1	11.2	260.5	13.9
c + d	22.44	0.065	2.7	0.001	26.4	8×10^{-6}	19.1	0.05	23.1	0.02
c + d	178.3	8.7	157.5	11.0	219.9	1.7	177.7	9.8	185.9	3.0
c + d	255.1	15.7	237.7	14.8	245.6	20.7	256.4	14.7	234.0	30.7
d + e	38.07	0.37	6.4	0.06	40.9	4×10^{-5}	32.9	0.3	39.5	0.1
d + e	102.2	0.0026	98.8	0.001	98.0	3×10^{-4}	105.45	0.003	101.0	2×10^{-4}
d + e	138.2	0.15	134.3	0.29	137.4	0.01	142.8	0.2	137.4	0.04
d + e	219.7	1.7	203.9	3.7	251.5	0.004	222.5	2.7	223.2	0.5
d + e	292.7	27.5	271.6	27	304.6	16.0	293.8	26.8	290.0	30.8
h + i	312.4	6.6	300.5	6.9	317.9	0.9	310.7	6.8	321.7	3.1
σ_{RMS} (G):			17.4		16.4		2.6		6.9	

Table 5.3: Positions and widths of s-wave resonance as obtained from the coupled channels calculations (CC), multichannel quantum defect theory (MQDT) and the asymptotic bound state model (ABM). For the two simple models, results are given using the physical values of a_{s}, a_{t} and C_6 obtained from Ref. [Fal08], and for an optimisation to the CC data. The bottom row of the table gives the RMS deviations from the CC results, showing the extent to which the free parameters of each model offset the limitations of the simplifying assumptions made.

Channel	CC B_0 (G)	MQDT B_0 (G)	ABM B_0 (G)
a + c	215.37	222.7	229.4
b + b	198.58	200.0	203.1
c + c	233.18	235.9	231.2
c + c	245.13	246.2	247.7
c + d	262.28	263.6	258.9
d + d	287.00	292.6	280.1
d + d	311.60	312.0	311.2
d + e	338.19	339.4	333.4
e + e	373.00	380.5	365.9
h + h	67.82	73.8	65.6
h + h	101.17	79.2	94.
h + h	136.46	119.7	136.5
h + h	323.37	320.1	336.5
h + j	44.57	48.1	43.3
i + i	44.80	48.4	43.5
	σ_{RMS} (G):	8.1	6.3

Table 5.4: Positions of several p-wave resonances, comparing MQDT and the ABM to CC results. The MQDT positions were calculated using the same fit derived for the s-wave resonances, while a separate ABM fit was performed. The value of σ_{RMS} is determined using the CC results without dipole-dipole interaction.

parameters as input, are shown in Fig. 5.5. For the MQDT it is difficult to reproduce the lower field (narrow) resonances as these result from a deeper bound state belonging to a (energetically) higher collision threshold. For the ABM it is hard to reproduce the highest field resonance as the threshold effects become strong for this (wide) resonance. These threshold effects can be incorporated [Tie10c] to produce better results for the wide resonance, as can be seen in the inset of Fig. 5.5. Both models have difficulties to reproduce the molecular bound-state manifolds at low magnetic fields around the 10 MHz. This can be attributed to the fact that the models were fit to resonance magnetic field positions, i.e. points at zero energy.

5.4 Summary and conclusions

We have presented a detailed study on the rich Feshbach resonance structure of ^{40}K. Excellent agreement is found for 29 resonances (both s-waves and p-waves) between the CC calculations and measurements, 26 of which were experimentally observed for the first time. Two of these resonances show features that deserve special attention: The 'well-isolated' s-wave resonance in the $c + d$ channel at 178(1) G with the nearest resonance at +55 G from the resonance center, which is of importance for applications relying on the zero crossing of the s-wave resonance. The other resonance is the p-wave resonance at 44(2) G in the $j + h$ channel, where the $j + h \rightarrow i + i$ decay

channel is close to elastic and might find an application in studies on three fermion interactions. Comparison of the CC calculations with the experimental observations shows that the currently available BO potentials [Fal08], which are used as input for the CC calculations, are sufficiently accurate to predict the position and width of all studied resonances within the experimental error of 100 mG. This provides confidence that, with these BO potentials, the CC method can be used to reliably model ultracold collisions of potassium atoms. A full characterization of the observed s-wave resonances is given in Table 5.1.

For the ABM, the large background scattering length for most scattering channels of ^{40}K made it necessary to account for the strong influence of scattering states via a magnetic field-dependent overlap parameter between the least-bound singlet and triplet states. This effectively accounts for the coupling between the bound and continuum states, and is provided by mapping the field-dependent background scattering length, a continuum parameter, onto the background binding energy, an ABM property that is sensitive to the overlap parameter. The mechanism is generic, and can be applied to other atomic systems with large positive background scattering lengths.

In addition we compared the performance of the MQDT and the ABM as two valuable simplified models complementary to the CC method. The MQDT is based on scattering states while the ABM is based on bound states. In essence, both models are based on three parameters. They are able to reproduce the scattering and bound state properties of ^{40}K atom pairs quite well. In particular the prediction of the resonance positions is fairly accurate. While MQDT gives the better optimized fit, the ABM performs slightly better with the physical input parameters and is the simpler approach. As both simplified methods do not account properly for the exchange energy, the predictions for the resonance width correspond only qualitatively to the CC results. As the ABM incorporates separate physical effects at separate levels, it provides a framework within which a system can be studied at various levels of complexity. This is not possible within the MQDT approach. The strengths and limitations of both models are illustrated by comparing the predicted resonance field positions and bound-state energy spectrum (for s- and p-wave resonances) with CC calculations. From a detailed study of the molecular bound-state manifolds of the s-wave $d + e$ channel we conclude that both models performed equally well, be it that ABM shows a difficulty in handling resonances were strong threshold effects are involved, whereas the MQDT has a handicap in cases when more deeply bound states are involved. Both the MQDT and the ABM proved to be very valuable for the exploration of the ^{40}K quantum gas as an example of a system with a rich structure of Feshbach resonances. For a full characterization the more demanding CC calculations remain indispensable.

Appendix A

Atoms in optical potentials

Neutral atoms can be trapped in an optical dipole potential due to the AC Stark effect. A far detuned intense laser beam induces an electric dipole moment in the atom. In the electric field of the laser beam, the induced dipole is subject to an optical potential. The electric field $\mathbf{E}$ of light induces a dipole $\mathbf{p}$ in an atom

$$\mathbf{p} = \alpha \mathbf{E}. \tag{A.1}$$

The complex atomic polarizability α is given by[Mil88]:

$$\alpha = 6\pi\varepsilon_0 c^3 \frac{\Gamma}{\omega_0^2} \left(\frac{1}{\omega_0^2 - \omega_L^2 - i(\omega_L^3/\omega_0^2)\Gamma} \right), \tag{A.2}$$

where ω_0 is the atomic resonance frequency, ω_L the (angular) frequency of the light, Γ the linewidth of the transition, c the speed of light and ε_0 the electric constant. The values for the D1 and D2 transitions of ^{40}K are given in Tables A.1 and A.2. The semi-classical approach in Eq. A.1 is valid as long as the light intensity I and detuning $\delta = \omega_L - \omega_0$ are such that the excited state is not substantially populated. The potential of the induced dipole $\mathbf{p}$ in the electric field $\mathbf{E}$ is given by

$$U_{\text{dip}}(\mathbf{r}) = -\frac{1}{2}\mathbf{p} \cdot \mathbf{E}(\mathbf{r}) = -\frac{1}{4\varepsilon_0 c} Re(\alpha) I(r), \tag{A.3}$$

with

$$I = \frac{\varepsilon_0 c}{2} |\mathbf{E}|^2.$$

A.1 Optical potential for ^{40}K

For a multilevel atom one has to consider in principle all optical dipole transitions with all their atomic polarizabilities. However, the linewidths of transitions to higher electronic states are an order of magnitude smaller than the transitions in the electronic ground state and add, in the case of ^{40}K, a correction of less than 1%. In [Gri00] the different detuning of the D1 and D2 line is also taken into account. In the case of ^{40}K, the detuning of both the dipole trap and the optical plug is much larger than the

Property	Symbol	Value	Ref.
Wavelength	$\lambda = c/\nu$	770.1081365(2) nm	
Frequency	$\omega = 2\pi\nu$	$2\pi \times$ 389.286184353(73) THz	[Fal06]
Wavenumber	$k = (2\pi)/\lambda$	$2\pi \times$ 12985.189385(3) cm^{-1}	
Lifetime	τ	26.72(5) ns	[Wan97]
Linewidth	$\Gamma = 1/\tau$	$2\pi \times$ 5.95(1) MHz	
Recoil velocity	$v_{rc} = (\hbar k)/m$	1.29654 cm/s	
Recoil temperature	$T_{rc} = (m v_{rc}^2)/(2k_B)$	404 nK	
Doppler temperature	$T_D = (\hbar\Gamma)/(2k_B)$	143 µK	
Saturation intensity	$I_s = (\pi hc)/(3\lambda^3\tau)$	1.70 mW/cm^2	

Table A.1: Optical properties of the D1 ($|^2S_{1/2}\rangle \rightarrow |^2P_{1/2}\rangle$) transition in ^{40}K. More data on properties of ^{40}K can be found in a concise form in [Tie10a]. Compilations of atomic data for other alkalis are available online from [Ste10] for rubidium, caesium and strontium; and from [Geh03] for lithium.

hyperfine splitting $\Delta E_{\mathrm{hf}} = 1.286\,\mathrm{GHz}$ so we use the average of the detunings of the D1 and D2 line and treat potassium as a two-level system.

If the detuning of the light is much smaller than the transition frequency of the atom ($|\delta| \ll \omega_0$) the potential A.3 can be written as [Gri00]:

$$U_{\mathrm{dip}}(\mathbf{r}) = -\frac{3\pi c^2}{2}\frac{\Gamma}{\omega_0^3}\left(\frac{1}{\omega_0 - \omega_L} + \frac{1}{\omega_0 + \omega_L}\right) I(\mathbf{r}). \tag{A.4}$$

A.2 Rotating wave approximation

The rotating wave approximation (RWA) can be used [Met99], if the following condition is fulfilled:

$$\omega_0 + \omega_L \gg \omega_0 - \omega_L. \tag{A.5}$$

The second term in the brackets can be neglected and A.4 simplifies to:

$$U_{\mathrm{RWA}}(\mathbf{r}) = \frac{3\pi c^2}{2\omega_0^3}\frac{\Gamma}{\delta} I(\mathbf{r}). \tag{A.6}$$

For $\delta < 0$, i.e. a red-detuned light field, the potential is attractive and the atom experiences a force towards regions of high light intensities. The atoms stay trapped in the focus of a red-detuned laser beam . A blue-detuned light field repels the atoms away from high intensities. We use this for the optical plug as described in Sec. 3.5.2. In the case of ^{40}K the condition A.5 is not entirely fulfilled. The potential is underestimated by about 10% when the RWA is used, so we do not apply this approximation.

Property	Symbol	Value	Ref.
Wavelength	$\lambda = c/\nu$	766.7006746(2) nm	
Frequency	$\omega = 2\pi\nu$	$2\pi \times$ 391.016296050(88) THz	[Fal06]
Wavenumber	$k = (2\pi)/\lambda$	$2\pi \times$ 13042.899699(2) cm^{-1}	
Lifetime	τ	26.37(5) ns	[Wan97]
Linewidth	$\Gamma = 1/\tau$	$2\pi \times$ 6.03(1) MHz	
Recoil velocity	$v_{rc} = (\hbar k)/m$	1.3023 cm/s	
Recoil temperature	$T_{rc} = (m v_{rc}^2)/(2k_B)$	408 nK	
Doppler temperature	$T_D = (\hbar\Gamma)/(2k_B)$	145 µK	
Saturation intensity	$I_s = (\pi hc)/(3\lambda^3\tau)$	1.75 mW/cm^2	

Table A.2: Optical properties of the D2 ($|^2S_{1/2}\rangle \rightarrow |^2P_{3/2}\rangle$) transition in ^{40}K.

A.3 Potential produced by a Gaussian beam

For a Gaussian laser beam with power P and beamwaist w_0, the intensity distribution $I(r,z)$ in axial z and radial direction r is described by

$$I(r,z) = \frac{2P}{\pi w(z)^2} \exp\left(\frac{-2r^2}{w(z)^2}\right). \tag{A.7}$$

The beam radius $w(z)$ at distance z from the beamwaist w_0 is given by

$$w(z) = w_0\sqrt{1 + (z/z_R)^2}, \tag{A.8}$$

with the Rayleigh range

$$z_R = \frac{\pi}{\lambda} w_0^2.$$

For linearly polarized light the potential is:

$$U_{\mathrm{dip}}(r,z) = \frac{U_0}{1 + (z/z_R)^2} \exp\left(\frac{-2r^2}{w(z)^2}\right), \tag{A.9}$$

with

$$U_0 = -\frac{3c^2\Gamma P}{\omega_0^3 w_0^2}\left(\frac{1}{\omega_0 - \omega_L} + \frac{1}{\omega_0 + \omega_L}\right). \tag{A.10}$$

The trap frequencies of the atom with mass m, in radial ω_r and axial ω_z trap directions are given by

$$\omega_i = \sqrt{\frac{1}{m}\left|\frac{\partial^2 U_{\mathrm{dip}}(r,z)}{\partial i^2}\right|}. \tag{A.11}$$

Around the focus of the beam ($z, r = 0$), where the trap can be assumed to be harmonic, the trap frequencies are

$$\omega_r = \sqrt{\frac{4U_0}{m w_0^2}} \qquad \text{and} \qquad \omega_z = \sqrt{\frac{2U_0}{m z_R^2}}. \tag{A.12}$$

A.4 Density distribution

The density distribution of the atoms in a potential $U(\mathbf{r})$ is determined by a distribution function. For temperatures larger than the Fermi temperature T_F this is the Maxwell-Boltzmann distribution:

$$f_{\mathrm{MB}}(\epsilon) = e^{-\epsilon/k_{\mathrm{B}}T}. \tag{A.13}$$

For non-interacting particles with the single particle Hamiltonian

$$\mathbf{H}(\mathbf{p},\mathbf{r}) = \frac{\mathbf{p}^2}{2m} + U(\mathbf{r}),$$

the density is obtained by integration over all possible momenta:

$$n_{\mathrm{MB}}(\mathbf{r}) = \int n_0 e^{-\mathbf{H}(\mathbf{p},\mathbf{r})/k_{\mathrm{B}}T}\, d\mathbf{p}. \tag{A.14}$$

A.4.1 Density in a harmonic potential

For a harmonic potential, which can be used as an approximation for the optical dipole trap at low atom temperatures, the integration results in a Gaussian density distribution

$$n_{\mathrm{MB}}(\mathbf{r}) = n_{0,\mathrm{MB}} e^{m\omega_r^2(x^2+y^2+A^2z^2)/2}, \tag{A.15}$$

with

$$n_{0,\mathrm{MB}} = NA\omega_r^3 \left(\frac{m}{2\pi k_{\mathrm{B}}T}\right)^{3/2}$$

and where $A = \omega_z/\omega_r$ is the aspect ratio of the optical dipole trap.

A.4.2 Density in a Gaussian potential

The density distribution of N atoms at a temperature T in the (Gaussian) optical dipole trap is:

$$n_{\mathrm{ODT}}(r,z,T) = n_0 \exp\left(\frac{U_{\mathrm{dip}}(r,z)}{k_B T}\right); \tag{A.16}$$

from this the $1/e$ radii $w_r(T)$ and $w_z(T)$ can be obtained numerically. The central density is then

$$n_0 = \frac{N}{V_e} \qquad \text{using the effective volume} \qquad V_e(T) = \pi^{3/2} w_r^2 w_z. \tag{A.17}$$

The effective volume is obtained by approximating the density with a Gaussian distribution:

$$\widetilde{n}_{\mathrm{ODT}}(r,z,T) = n_0 \exp\left(\frac{-r^2}{2w_r^2(T)}\right) \exp\left(\frac{-z^2}{2w_z^2(T)}\right). \tag{A.18}$$

With this approximation the integration for the effective volume

$$\frac{N}{n_0} = V_e = \int_V \exp\left(\frac{-x^2}{2w_r^2(T)}\right) \exp\left(\frac{-y^2}{2w_r^2(T)}\right) \exp\left(\frac{-z^2}{2w_z^2(T)}\right) dx\, dy\, dz \tag{A.19}$$

can be solved with the Gauss error function $\mathrm{erf}(x)$ and the Euler gamma function $\Gamma(x)$ [Bro96].

Appendix B

Hyperfine structure

The fine structure of an alkali atom is determined by the coupling of the outer electron's spin **S** with its orbital angular momentum **L** to the total angular momentum of the electron[†]

$$\mathbf{J} = \mathbf{S} + \mathbf{L}.$$

The **L**–**S** coupling leads in alkalis to the D1 and D2 line with $J = 1/2$ and $J = 3/2$ respectively. For ^{40}K the fine structure splitting is 1.7 THz (see Tables A.1 and A.2), all additional perturbations due to the hyperfine interaction and external magnetic fields can be treated separately for each **J** when they are small compared to the fine structure splitting. The interaction between the angular momentum of the nucleus **I** and the electron **J** couples to the total angular momentum of the atom

$$\mathbf{F} = \mathbf{I} + \mathbf{J}$$

and results in the hyperfine splitting. All the angular momentum operators $\mathbf{F}, \mathbf{I}, \mathbf{J}$ have corresponding quantum numbers F, I, J which obey the triangular relation

$$|I - J| \leq F \leq I + J,$$

[†]In atoms with more than one valence electron the coupling can differ from the described **L**–**S** coupling. In that case **j**–**j** coupling occurs or mixtures of both **j**–**j** and **L**–**S** coupling, depending on the energy scales.

Property	**Symbol**	**Value**	**Ref.**
Mass	m	39.96399848(21) u	[NIS10]
Nuclear spin	I	4	
Number of Neutrons	N	21	
Atomic number	Z	19	
Natural abundance		0.000117(1) %	[NIS10]
Isotope lifetime	$\tau_{40\mathrm{K}}$	1.248×10^9 y	[NND11]

Table B.1: Physical properties of ^{40}K. The mass is given in unified atomic mass units ($1\,\mathrm{u} = 1.660538921 \times 10^{-27}\,\mathrm{kg}$).

State	Property	Symbol	Value [MHz]	Ref.
$^2S_{1/2}$	magnetic dipole constant	a_{hf}	$h\times -285.7308(24)$	[Ari77]
$^2P_{1/2}$	magnetic dipole constant	a_{hf}	$h\times -34.523(25)$	[Fal06]
$^2P_{3/2}$	magnetic dipole constant	a_{hf}	$h\times -7.585(10)$	[Fal06]
$^2P_{3/2}$	electric quadrupole constant	b_{hf}	$h\times -3.445(90)$	[Fal06]

Table B.2: Hyperfine structure coefficients for ^{40}K.

so there are $(2J+1)$ possible values for F when $J<I$. The angular momentum operators obey the relation

$$\mathbf{I}\cdot\mathbf{J}=\frac{1}{2}(\mathbf{F}^2-\mathbf{I}^2-\mathbf{J}^2).$$

The hyperfine interaction is described by the Hamiltonian

$$\mathbf{H}_{\mathrm{hf}}=\frac{1}{\hbar^2}\left(a_{\mathrm{hf}}\mathbf{I}\cdot\mathbf{J}+b_{\mathrm{hf}}\frac{3(\mathbf{I}\cdot\mathbf{J})^2+\frac{3}{2}\mathbf{I}\cdot\mathbf{J}-\mathbf{I}^2\mathbf{J}^2}{2I(2I-1)J(2J-1)}\right), \tag{B.1}$$

using the magnetic dipole constant a_{hf} and the electric quadrupole constant b_{hf}. The quadrupole term only exists for states with $J>1/2$, as derived in [MK85]. The values for a_{hf} and b_{hf} are shown in Table B.2.

B.1 Hyperfine splitting with an external magnetic field

The hyperfine interaction in presence of an external magnetic field B is described by

$$\mathbf{H}_{\mathrm{hf}}^{B}=\mathbf{H}_{\mathrm{hf}}+\mathbf{H}_{\mathrm{Z}}, \tag{B.2}$$

where $\mathbf{H}_{\mathrm{Z}}$ is the Zeeman interaction

$$\mathbf{H}_{\mathrm{Z}}=\frac{\mu_{\mathrm{B}}}{\hbar}(g_J\mathbf{J}+g_I\mathbf{I})\cdot\mathbf{B}, \tag{B.3}$$

with the Landé g-factor of the electron g_J, the gyromagnetic factor of the nucleus g_I and the Bohr magneton μ_{B}. Here the sign convention is[‡]:

$$\boldsymbol{\mu}_I=-g_I\mu_{\mathrm{B}}\frac{\mathbf{I}}{\hbar}\qquad\text{and}\qquad\boldsymbol{\mu}_J=-g_J\mu_{\mathrm{B}}\frac{\mathbf{J}}{\hbar}. \tag{B.4}$$

The values for the g-factors are in Table B.3. The level structure of the hyperfine states for ^{40}K is shown for the ground state $|^2S_{1/2}\rangle$ in Fig. B.1 and for the excited state $|^2P_{3/2}\rangle$ in Fig. B.2.

In practice we solve the field dependence and energy splitting of the hyperfine states numerically, however in the special case of $F=I\pm1/2$ ($J=1/2$) the Breit-Rabi formula [Bre31, Oh08] provides an analytical expression for the eigenvalues of $\mathbf{H}_{\mathrm{hf}}^{B}$ for the Zeeman states with quantum number m_F:

[‡]The sign convention for $\boldsymbol{\mu}_I$ is chosen as in [Ari77].

State	Property	Symbol	Value	Ref.
All states	total nuclear g-factor	g_I	0.000176490(34)	[Ari77]‡
$^2S_{1/2}$	total electronic g-factor	g_J	2.00229421 (24)	[Ari77]
$^2P_{1/2}$	total electronic g-factor	g_J	2/3	
$^2P_{3/2}$	total electronic g-factor	g_J	4/3	

Table B.3: Electronic and gyromagnetic factors for ^{40}K.

$$E(F = I \pm 1/2, m_F) = -\frac{a_{\rm hf}}{4} + m_F g_I \mu_{\rm B} B \pm \frac{\Delta E_{\rm hf}}{2}\sqrt{1 + \frac{4m_F}{2I+1}x + x^2} \tag{B.5}$$

using the abbreviation

$$x = \frac{(g_J - g_I)\mu_{\rm B}}{\Delta E_{\rm hf}} B$$

and the hyperfine splitting energy

$$\Delta E_{\rm hf} = a_{\rm hf}\left(I + \frac{1}{2}\right).$$

We employ this analytical expression for the calibration of the magnetic field described in Sec. 4.5.

B.2 Limit of high and low magnetic fields

For low magnetic fields B the **I**–**J** coupling is valid and the total angular momentum **F** precesses around the direction of the magnetic field. The hyperfine energy for states with $J = 1/2$ is then well described by the linear Zeeman effect:

$$E_{\rm hf}^{B,\rm low} = m_F g_F \mu_B B + \Delta E_{\rm hf}^0 \tag{B.6}$$

using the hyperfine splitting at zero field

$$\Delta E_{\rm hf}^0 = \frac{a_{\rm hf}}{2}[F(F+1) - I(I+1) - J(J+1)]$$

and

$$g_F = g_J \frac{F(F+1) + J(J+1) - I(I+1)}{2F(F+1)} + g_I \frac{F(F+1) + I(I+1) - J(J+1)}{2F(F+1)}.$$

The values for g_F for the different manifolds are shown in Table B.4. In high magnetic field the **I**–**J** coupling is lifted and both angular momenta precess independently around the direction of the magnetic field. In this so called Paschen-Back regime, the hyperfine energy of a state with quantum number m_I, m_J and $J = 1/2$ is approximated by:

$$\Delta E_{\rm hf}^{B,\rm high} = m_J g_J \mu_B B + a_{\rm hf} m_I m_J. \tag{B.7}$$

State	Value
$^2S_{1/2}, F = 9/2$	0.222634
$^2S_{1/2}, F = 7/2$	−0.222281
$^2P_{1/2}, F = 9/2$	0.074231
$^2P_{1/2}, F = 7/2$	−0.073878
$^2P_{3/2}, F = 11/2$	0.363765
$^2P_{3/2}, F = 9/2$	0.229102
$^2P_{3/2}, F = 7/2$	−0.020985
$^2P_{3/2}, F = 5/2$	−0.571176

Table B.4: Landé g_F factors for ^{40}K.

The hyperfine field B_{hf} is a characteristic crossover field. It is defined as the magnetic field where the energy of the states in the low-field approximation equals the energy in the high-field approximation. For $J = 1/2$ it is [Leg01]

$$B_{\mathrm{hf}} = \frac{a_{\mathrm{hf}}(I + 1/2)}{(g_J - g_I)\mu_{\mathrm{B}}} \approx \frac{a_{\mathrm{hf}}(I + 1/2)}{2\mu_{\mathrm{B}}}.$$

The hyperfine field for the ground state manifold $^2S_{1/2}$ of ^{40}K is $B_{\mathrm{hf}} = 459\,\mathrm{G}$. The low-field approximation is valid to describe the cold atoms in the MOT and the magnetic trap, as the magnetic fields used are much lower than B_{hf}.

B.3 Magnetic trapping potential

Neutral atoms are trapped magnetically due to the Zeeman effect: an applied magnetic field **B** shifts the eigenenergies of an atom proportionally to the magnetic field value $|B|$. The applied field results in a magnetic moment μ which is aligned with the external field. The magnetic potential is

$$U(B) = -\mu \cdot \mathbf{B} = m_F g_F \mu_B B, \tag{B.8}$$

States where $m_F g_F > 0$ are trapped, and states where $m_F g_F < 0$ are expelled from a magnetic gradient as described in Sec. 3.5.1. The exact trapping potential depends on the geometry of the magnetic field, a more detailed discussion about magnetic trapping and trap geometries can be found in [Ber87, Ket92, Met99, Ket99, For07].

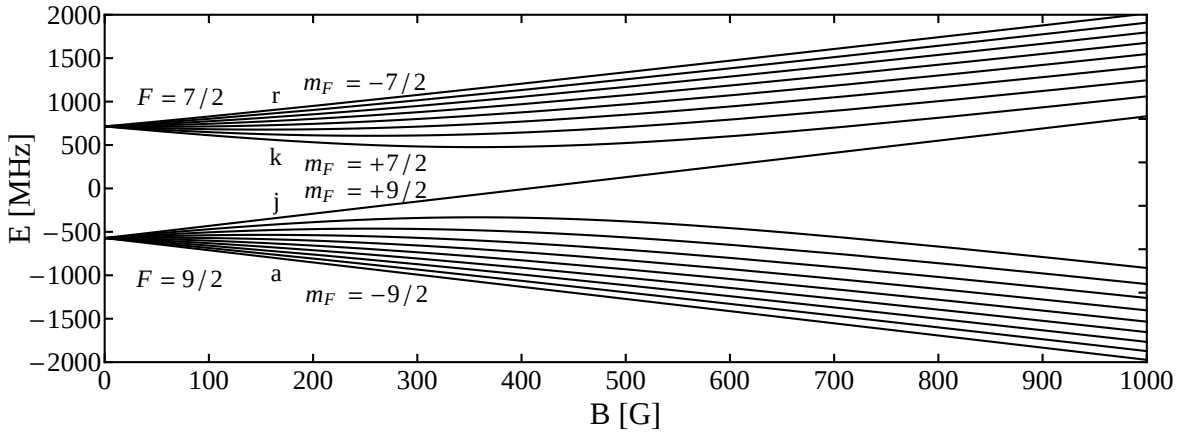

Figure B.1: The hyperfine structure of the ground state $|^2S_{1/2}\rangle$ of ^{40}K. The states are labelled with the low field quantum numbers $|F, m_F\rangle$ and with a to r with rising energy. In the lower hyperfine manifold (F = 9/2), the states f to j are low-field seeking at low magnetic field. In the upper hyperfine manifold (F = 7/2) the states o to r are low-field seeking. The hyperfine structure is inverted unlike in most other alkalis.

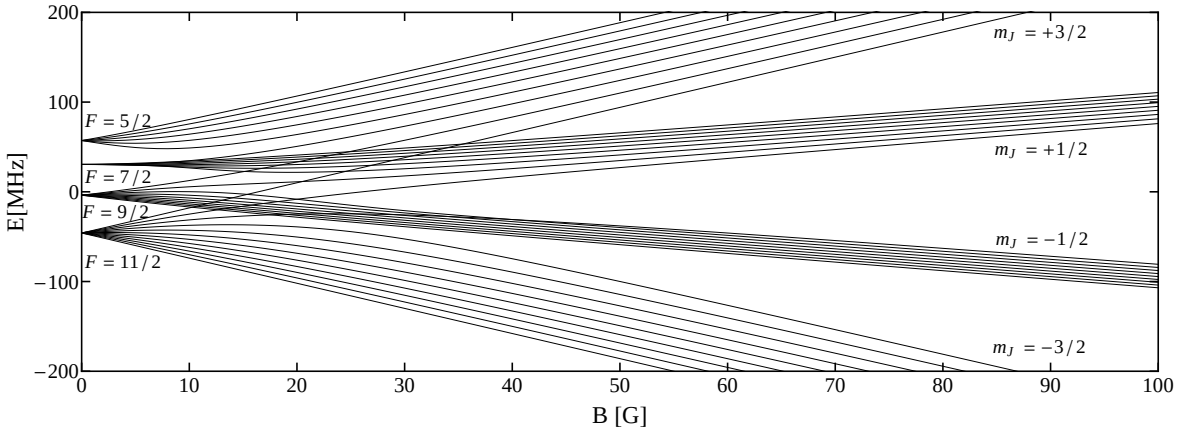

Figure B.2: The hyperfine splitting of the excited state $|^2P_{3/2}\rangle$. The states are labelled with the high-field quantum numbers.

Appendix C

Optical transition probabilities

When imaging cold atoms, the transition strength of the used imaging transition needs to be known to accurately fit the number of atoms. Additionally the frequency of the imaging light and – if necessary – of the repump light has to be chosen according to the possible transitions and decay channels. The transition matrix element μ_{eg} describes the coupling between a ground and an excited state by an electric dipole:

$$\mu_{\mathrm{eg}} = e \left\langle \mathrm{e}|\widehat{\epsilon} \cdot \mathbf{r}|\mathrm{g}\right\rangle ,$$

here $\widehat{\epsilon}$ is the unit vector of the light polarization and e the elementary charge. The states are described by a wavefunction which can be factorised into a radial part and an angular part. The transition matrix element can be expanded in terms of Clebsch-Gordan coefficients using the Wigner-Eckart theorem. A detailed derivation can be found for example in [Met99, Wal10, LeB11]. The transition strengths for other isotopes of potassium and other alkalis are in listed [Met99].

C.1 Transition probabilities at zero magnetic field

The transition matrix element μ_{eg} coupling a ground state with quantum numbers n, L, S, I, J, F, m_F to an excited state with quantum numbers $n, L', S, I, J', F', m'_F$ can be expressed as:

$$\mu_{\mathrm{eg}} = e\mathcal{R}\mathcal{A},$$

the radial part $\mathcal{R}$ only concerns the n, L quantum numbers and is the same for all transitions within one line. To compare the transition strengths of transitions in the D1 and in the D2 line, the radial part $\mathcal{R}$ has to be taken into account (see [Met99]). The angular part is described by:

$$\begin{aligned}\mathcal{A} = (-1)^{1+L'+S+J+J'+I-m'} &\sqrt{(2J+1)(2J'+1)(2F+1)(2F'+1)} \\ &\times \sqrt{\max(L,L')} \begin{pmatrix} F & 1 & F' \\ m & q & -m' \end{pmatrix} \begin{Bmatrix} J' & F' & I \\ F & J & 1 \end{Bmatrix} \begin{Bmatrix} L' & J' & S \\ J & L & 1 \end{Bmatrix}. \quad \text{(C.1)}\end{aligned}$$

The curly brackets denote 6j-symbols and the normal brackets 3j-symbols. The j-symbols enforce the correct coupling of angular momenta and obey the triangular relation and selection rules. The selection rules in this case are:

$$\begin{aligned}
&\Delta L = 0, \pm 1 \text{ with } L = 0 \nrightarrow L' = 0 \\
&\Delta S = 0 \\
&\Delta J = 0, \pm 1 \text{ with } J = 0 \nrightarrow J' = 0 \\
&\Delta I = 0 \\
&\Delta F = 0, \pm 1 \text{ with } F = 0 \nrightarrow F' = 0
\end{aligned} \qquad \text{(C.2)}$$

At low or zero magnetic field it is $m = m_F$ in Eq. C.1 and the selection rule

$$\Delta m_F = 0, \pm 1 \text{ for } \pi \text{ and } \sigma^{\pm} \text{ polarized light applies.} \qquad \text{(C.3)}$$

In Tables C.1 and C.2 the normalized (angular) transition strengths $\mathcal{A}^2$, for transitions from the states $|^2S_{1/2}, F = 9/2, 7/2\rangle$ are given.

C.2 Transition probabilities at non-zero magnetic field

With rising magnetic field the quantum numbers $|J, I, F, m_F\rangle$ cease to be good quantum numbers. The eigenvectors of the hyperfine Hamiltonian $\mathbf{H}^B_{\mathrm{hf}}$ in Eq. B.2 are no longer pure states of one set of $|J, I, F, m_F\rangle$, but a mixture. In the high field limit the quantum numbers $|J, I, m_J, m_I\rangle$ are good quantum numbers and form a basis for $\mathbf{H}^B_{\mathrm{hf}}$. To describe the absorption of imaging light by the atoms in high field, the transition matrix elements have to be adapted. When considering transitions from the $^2S_{1/2}$ manifold to the $^2P_{3/2}$ manifold, the hyperfine fields B_{hf} of the differ substantially. The hyperfine field in the ground state is $B_{\mathrm{hf}} = 459\,\mathrm{G}$, in the excited $^2P_{3/2}$ state it is about 35 G. As can be seen in Fig. B.2, there are no more level crossings at magnetic fields higher than the hyperfine field, so the labelling in the high-field quantum numbers is justified. Apart from the fully-stretched states $|m_J = -3/2, m_I = -4\rangle$ and $|m_J = 3/2, m_I = 4\rangle$, the eigenstates are mixtures of the high-field basis states.

As an example we consider the transition from $|J = 1/2, F = 9/2, m_F = -3/2\rangle$ to $|J' = 3/2, F' = 11/2, m'_F = -5/2\rangle$, at a field of 178 G close to the Feshbach resonance in the $c+d$ state. The states can be expressed in terms of the $|m_J, m_I\rangle$ basis by solving the Hamiltonian $\mathbf{H}^B_{\mathrm{hf}}$ numerically.

$$|F, m_F\rangle = \alpha\,|m_J = m_F - m_I, m_I\rangle + \beta\,|m_J = m_F - m_I, m_I\rangle + \cdots$$

For the ground state it is:

$$|9/2, -3/2\rangle = 0.897\,|-1/2, -1\rangle + 0.443\,|1/2, -2\rangle\,.$$

For the excited state it is:

$$|11/2, -5/2\rangle = -0.997\,|-3/2, -1\rangle - 0.083\,|-1/2, -2\rangle - 0.003\,|1/2, -3\rangle - 5\times10^{-5}\,|3/2, -4\rangle\,.$$

At $B = 178\,\mathrm{G}$ the excited consists of four $|m_J, m_I\rangle$ basis states, two of the basis states have coefficients which are smaller than 0.01. The contributions of these states only

	$\mathbf{F = 9/2, m_F =}$	$\mathbf{-9/2}$ a	$\mathbf{-7/2}$ b	$\mathbf{-5/2}$ c	$\mathbf{-3/2}$ d	$\mathbf{-1/2}$ e	$\mathbf{1/2}$ f	$\mathbf{3/2}$ g	$\mathbf{5/2}$ h	$\mathbf{7/2}$ i	$\mathbf{9/2}$ j
π	$F' = 9/2$	81	49	25	9	1	1	9	25	49	81
	$F' = 7/2$	0	32	56	72	80	80	72	56	32	
σ^+	$F' = 9/2$	18	32	42	48	50	48	42	32	18	
	$F' = 7/2$	144	112	84	60	40	24	12	4		
	$\mathbf{F = 7/2, m_F =}$		$\mathbf{-7/2}$ r	$\mathbf{-5/2}$ q	$\mathbf{-3/2}$ p	$\mathbf{-1/2}$ o	$\mathbf{1/2}$ n	$\mathbf{3/2}$ m	$\mathbf{5/2}$ l	$\mathbf{7/2}$ k	
π	$F' = 9/2$		32	56	72	80	80	72	56	32	
	$F' = 7/2$		49	25	9	1	1	9	25	49	
σ^+	$F' = 9/2$		4	12	24	40	60	84	112	144	
	$F' = 7/2$		14	24	30	32	30	24	14		

Table C.1: (Angular) transition strengths from $|F = 7/2, F = 9/2, m_F\rangle$ to the $^2P_{1/2}$ manifold (D1-line) in ^{40}K. The values are normalized to the weakest transition in the D1 line ($|F = 9/2, m_F = -1/2\rangle \rightarrow |F' = 9/2, m'_F = -1/2\rangle$). It is $m'_F = m_F + 1$ for σ^+ transitions and $m'_F = m_F$ for π transitions.

	$\mathbf{F = 9/2, m_F =}$	$\mathbf{-9/2}$ a	$\mathbf{-7/2}$ b	$\mathbf{-5/2}$ c	$\mathbf{-3/2}$ d	$\mathbf{-1/2}$ e	$\mathbf{1/2}$ f	$\mathbf{3/2}$ g	$\mathbf{5/2}$ h	$\mathbf{7/2}$ i	$\mathbf{9/2}$ j
	$F' = 11/2$	68040	122472	163296	190512	204120	204120	190512	163296	122472	68040
π	$F' = 9/2$	181440	109760	56000	20160	2240	2240	20160	56000	109760	181440
	$F' = 7/2$		17248	30184	38808	43120	43120	38808	30184	17248	
	$F' = 11/2$	6804	20412	40824	68040	102060	142884	190512	244944	306180	374220
σ^+	$F' = 9/2$	40320	71680	94080	107520	112000	107520	94080	71680	40320	
	$F' = 7/2$	77616	60368	45276	32340	21560	12936	6468	2156		
	$\mathbf{F = 7/2, m_F =}$		$\mathbf{-7/2}$ r	$\mathbf{-5/2}$ q	$\mathbf{-3/2}$ p	$\mathbf{-1/2}$ o	$\mathbf{1/2}$ n	$\mathbf{3/2}$ m	$\mathbf{5/2}$ l	$\mathbf{7/2}$ k	
	$F' = 9/2$		33880	59290	76230	84700	84700	76230	59290	33880	
π	$F' = 7/2$		215600	110000	39600	4400	4400	39600	110000	215600	
	$F' = 5/2$			80190	133650	160380	160380	133650	80190		
	$F' = 9/2$		4235	12705	25410	42350	63525	88935	118580	152460	
σ^+	$F' = 7/2$		61600	105600	132000	140800	132000	105600	61600		
	$F' = 5/2$		280665	200475	133650	80190	40095	13365			

Table C.2: (Angular) transition strengths from $|^2S_{1/2}, F = 7/2, F = 9/2, m_F\rangle$ to the $^2P_{3/2}$ manifold (D2-line) for ^{40}K. The values are normalized to the weakest transition in the D2 line ($|F = 9/2, m_F = -1/2\rangle \rightarrow |F' = 9/2, m'_F = -1/2\rangle$) and multiplied with the greatest common denominator to obtain integer values as it is done in [Met99]. It is $m'_F = m_F + 1$ for σ^+ transitions and $m'_F = m_F$ for π transitions.

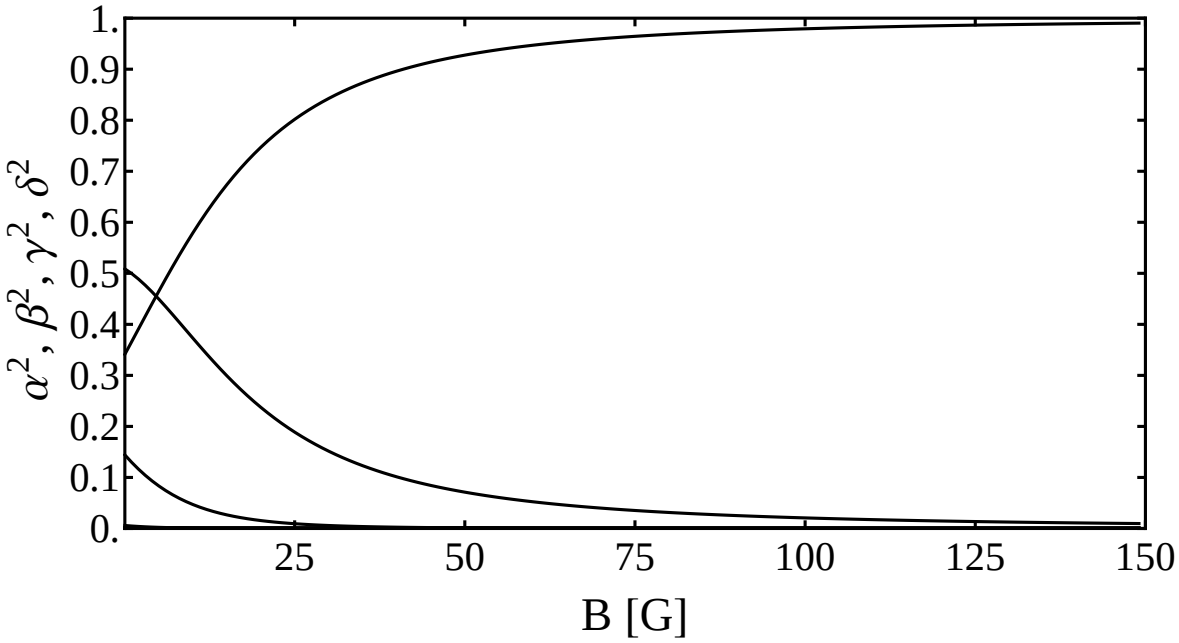

Figure C.1: Coefficients α^2, β^2, γ^2 and δ^2 of the decomposition of the $|J = 3/2, F = 11/2, -5/2\rangle$ state in the $|m_J, m_I\rangle$ basis.

play a role for fields up to the hyperfine field B_{hf} of the excited state (see Fig. C.1). The decomposition of the ground state is shown in Fig. C.2.

The transition matrix elements can now be calculated by calculating the coefficients in the $|m_J, m_I\rangle$ basis by replacing m by m_J and then summing over the m_J:

$$\mathcal{A}^B = \delta_{m_I m_I'} \sum_{m_J} \mathcal{A} \langle J, m_J, m_I | J, F, m_F \rangle \tag{C.4}$$

The decomposition of the lower state in terms of the $|m_J, m_I\rangle$ basis is included by the last term. In addition to the selection rules in Eq. C.2, the following selection rules apply:

$$\begin{aligned} &\Delta m_I = 0 \\ &\Delta m_J = 0, \pm 1 \text{ for } \pi \text{ and } \sigma^{\pm} \text{ polarized light.} \end{aligned} \tag{C.5}$$

The decomposition has to be calculated numerically and has a different field dependency for each state.

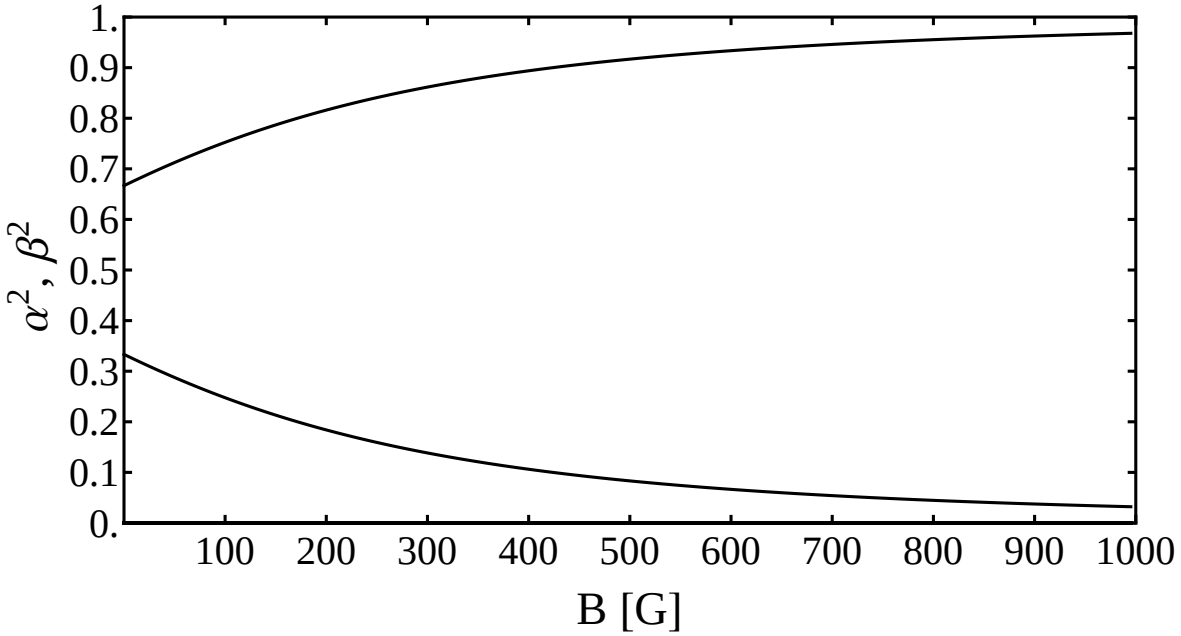

Figure C.2: Coefficients α^2 and β^2 of the decomposition of the $|J = 1/2, F = 9/2, -3/2\rangle$ state in the $|m_J, m_I\rangle$ basis.

Bibliography

[A] *All data from internet sources was retrieved in the year noted.*

[Ada95] C. S. Adams, H. J. Lee, N. Davidson, M. Kasevich and S. Chu, *Evaporative Cooling in a Crossed Dipole Trap*, Phys. Rev. Lett. **74**, 3577 (1995).

[And95] M. H. Anderson, J. R. Ensher, M. R. Matthews, C. E. Wieman and E. A. Cornell, *Observation of Bose-Einstein Condensation in a Dilute Atomic Vapor*, Science **269**, 198 (1995).

[Ari77] E. Arimondo, M. Inguscio and P. Violino, *Experimental determinations of the hyperfine structure in the alkali atoms*, Rev. Mod. Phys. **49**, 31 (1977).

[Ash70] A. Ashkin, *Acceleration and Trapping of Particles by Radiation Pressure*, Phys. Rev. Lett. **24**, 156 (1970).

[Aub05] S. Aubin, M. H. T. Extavour, S. Myrskog, L. J. LeBlanc, J. Estève, S. Singh, P. Scrutton, D. McKay, R. McKenzie, I. D. Leroux, A. Stummer and J. H. Thywissen, *Trapping Fermionic ^{40}K and Bosonic ^{87}Rb on a Chip*, Journal of Low Temperature Physics **140**, 377 (2005).

[Bag87] V. Bagnato, D. E. Pritchard and D. Kleppner, *Bose-Einstein condensation in an external potential*, Phys. Rev. A **35**, 4354 (1987).

[Bar02] M. Baranov, L. Dobrek, K. Góral, L. Santos and M. Lewenstein, *Ultracold Dipolar Gases - a Challenge for Experiments and Theory*, Physica Scripta **2002**, 74 (2002).

[Ber87] T. Bergeman, G. Erez and H. J. Metcalf, *Magnetostatic trapping fields for neutral atoms*, Phys. Rev. A **35**, 1535 (1987).

[Bil08] J. Billy, V. Josse, Z. Zuo, A. Bernard, B. Hambrecht, P. Lugan, D. Clement, L. Sanchez-Palencia, P. Bouyer and A. Aspect, *Direct observation of Anderson localization of matter waves in a controlled disorder*, Nature **453**, 891 (2008).

[Bir74] F. Biraben, B. Cagnac and G. Grynberg, *Experimental Evidence of Two-Photon Transition without Doppler Broadening*, Phys. Rev. Lett. **32**, 643 (1974).

[Blo08] I. Bloch, J. Dalibard and W. Zwerger, *Many-body physics with ultracold gases*, Rev. Mod. Phys. **80**, 885 (2008).

[Boh99] J. L. Bohn and P. S. Julienne, *Semianalytic theory of laser-assisted resonant cold collisions*, Phys. Rev. A **60**, 414 (1999).

[Bos24] S. N. Bose, *Plancks Gesetz und Lichtquantenhypothese*, Zeitschrift für Physik **26**, 178 (1924).

[Bre31] G. Breit and I. I. Rabi, *Measurement of Nuclear Spin*, Phys. Rev. **38**, 2082 (1931).

[Bro96] I. N. Bronstein, K. A. Semandjajew, W. Hackbusch, H. R. Schwarz and E. Zeidler, *Taschenbuch der Mathematik* (Teubner, Stuttgart, 1996).

[Bru00] G. M. Bruun and C. W. Clark, *Ideal gases in time-dependent traps*, Phys. Rev. A **61**, 061601 (2000).

[Bur97] J. P. Burke, J. L. Bohn, B. D. Esry and C. H. Greene, *Impact of the ^{87}Rb singlet scattering length on suppressing inelastic collisions*, Phys. Rev. A **55**, R2511 (1997).

[But97] D. A. Butts and D. S. Rokhsar, *Trapped Fermi gases*, Phys. Rev. A **55**, 4346 (1997).

[Cas96] Y. Castin and R. Dum, *Bose-Einstein Condensates in Time Dependent Traps*, Phys. Rev. Lett. **77**, 5315 (1996).

[Cat98] F. S. Cataliotti, E. A. Cornell, C. Fort, M. Inguscio, F. Marin, M. Prevedelli, L. Ricci and G. M. Tino, *Magneto-optical trapping of Fermionic potassium atoms*, Phys. Rev. A **57**, 1136 (1998).

[Cat06] J. Catani, P. Maioli, L. De Sarlo, F. Minardi and M. Inguscio, *Intense slow beams of bosonic potassium isotopes*, Phys. Rev. A **73**, 033415 (2006).

[Cha06] S. Chaudhuri, S. Roy and C. S. Unnikrishnan, *Realization of an intense cold Rb atomic beam based on a two-dimensional magneto-optical trap: Experiments and comparison with simulations*, Phys. Rev. A **74**, 023406 (2006).

[Che05] Q. Chen, J. Stajic, S. Tan and K. Levin, *BCS - BEC crossover: From high temperature superconductors to ultracold superfluids*, Physics Reports **412**, 1 (2005).

[Chi05] C. Chin, *A simple model of Feshbach molecules*, ArXiv e-prints **0506.313** (2005).

[Chi10] C. Chin, R. Grimm, P. Julienne and E. Tiesinga, *Feshbach resonances in ultracold gases*, Rev. Mod. Phys. **82**, 1225 (2010).

[Chu86] S. Chu, J. E. Bjorkholm, A. Ashkin and A. Cable, *Experimental Observation of Optically Trapped Atoms*, Phys. Rev. Lett. **57**, 314 (1986).

[Cou98] P. Courteille, R. S. Freeland, D. J. Heinzen, F. A. van Abeelen and B. J. Verhaar, *Observation of a Feshbach Resonance in Cold Atom Scattering*, Phys. Rev. Lett. **81**, 69 (1998).

[CT77] C. Cohen-Tannoudji, B. Diu and F. Laloe, *Quantum mechanics* (Wiley, New York, 1977).

[Dav95a] K. B. Davis, M. O. Mewes, M. R. Andrews, N. J. van Druten, D. S. Durfee, D. M. Kurn and W. Ketterle, *Bose-Einstein Condensation in a Gas of Sodium Atoms*, Phys. Rev. Lett. **75**, 3969 (1995).

[Dav95b] K. B. Davis, M. O. Mewes and W. Ketterle, *An analytical model for evaporative cooling of atoms*, Applied Physics B: Lasers and Optics **60**, 155 (1995).

[Deh10] B. Deh, W. Gunton, B. G. Klappauf, Z. Li, M. Semczuk, J. Van Dongen and K. W. Madison, *Giant Feshbach resonances in ^{6}Li-^{85}Rb mixtures*, Phys. Rev. A **82**, 020701 (2010).

[DeM99a] B. DeMarco and D. S. Jin, *Onset of Fermi Degeneracy in a Trapped Atomic Gas*, Science **285**, 1703 (1999).

[DeM99b] B. DeMarco, H. Rohner and D. S. Jin, *An enriched ^{40}K source for fermionic atom studies*, Review of Scientific Instruments **70**, 1967 (1999).

[DeM01] B. DeMarco, *Quantum Behavior of an Atomic Fermi Gas*, Ph.D. thesis, University of Colorado (2001).

[Deu98] I. H. Deutsch and P. S. Jessen, *Quantum-state control in optical lattices*, Phys. Rev. A **57**, 1972 (1998).

[Die98] K. Dieckmann, R. J. C. Spreeuw, M. Weidemüller and J. T. M. Walraven, *Two-dimensional magneto-optical trap as a source of slow atoms*, Phys. Rev. A **58**, 3891 (1998).

[Dir26] P. A. M. Dirac, *On the Theory of Quantum Mechanics*, Proceedings of the Royal Society of London. Series A, Containing Papers of a Mathematical and Physical Character **112**, pp. 661 (1926).

[Efi70] V. Efimov, *Energy levels arising from resonant two-body forces in a three-body system*, Physics Letters B **33**, 563 (1970).

[Ein25] A. Einstein, *Quantentheorie des einatomigen idealen Gases, 2. Abhandlung*, Sitzungsberichte der Preussischen Akademie der Wissenschaften zu Berlin pages 3–14 (1925).

[Ekl75] H. Eklund, A. Roos and S. T. Eng, *Rotation of laser beam polarization in acousto-optic devices*, Optical and Quantum Electronics **7**, 73 (1975).

[Fal06] S. Falke, E. Tiemann, C. Lisdat, H. Schnatz and G. Grosche, *Transition frequencies of the D lines of ^{39}K, ^{40}K, and ^{41}K measured with a femtosecond laser frequency comb*, Phys. Rev. A **74**, 032503 (2006).

[Fal08] S. Falke, H. Knöckel, J. Friebe, M. Riedmann, E. Tiemann and C. Lisdat, *Potassium ground-state scattering parameters and Born-Oppenheimer potentials from molecular spectroscopy*, Phys. Rev. A **78**, 012503 (2008).

[Fed96] P. O. Fedichev, Y. Kagan, G. V. Shlyapnikov and J. T. M. Walraven, *Influence of Nearly Resonant Light on the Scattering Length in Low-Temperature Atomic Gases*, Phys. Rev. Lett. **77**, 2913 (1996).

[Fer24] E. Fermi, *Über die Wahrscheinlichkeit der Quantenzustände*, Zeitschrift für Physik A Hadrons and Nuclei **26**, 54 (1924).

[Fer26] E. Fermi, *Zur Quantelung des idealen einatomigen Gases*, Zeitschrift für Physik A Hadrons and Nuclei **36**, 902 (1926), a translation into English of the original report by A. Zannoni: ArXiv e-prints **9912.229**(1999).

[Fer02] G. Ferrari, M. Inguscio, W. Jastrzebski, G. Modugno, G. Roati and A. Simoni, *Collisional Properties of Ultracold K-Rb Mixtures*, Phys. Rev. Lett. **89**, 053202 (2002).

[Fer06] F. Ferlaino, C. D'Errico, G. Roati, M. Zaccanti, M. Inguscio, G. Modugno and A. Simoni, *Feshbach spectroscopy of a $K-Rb$ atomic mixture*, Phys. Rev. A **73**, 040702 (2006).

[Fes58] H. Feshbach, *Unified theory of nuclear reactions*, Annals of Physics **5**, 357 (1958).

[Fes62] H. Feshbach, *A unified theory of nuclear reactions. II*, Annals of Physics **19**, 287 (1962).

[Fey82] R. Feynman, *Simulating physics with computers*, International Journal of Theoretical Physics **21**, 467 (1982).

[Fla99] V. V. Flambaum, G. F. Gribakin and C. Harabati, *Analytical calculation of cold-atom scattering*, Phys. Rev. A **59**, 1998 (1999).

[Fli91] T. Fließbach, *Quantenmechanik* (BI Wissenschaftlicher Verlag, Mannheim, 1991).

[For07] J. Fortágh and C. Zimmermann, *Magnetic microtraps for ultracold atoms*, Rev. Mod. Phys. **79**, 235 (2007).

[Gae07] J. P. Gaebler, J. T. Stewart, J. L. Bohn and D. S. Jin, *p-Wave Feshbach Molecules*, Phys. Rev. Lett. **98**, 200403 (2007).

[Gao05] B. Gao, E. Tiesinga, C. J. Williams and P. S. Julienne, *Multichannel quantum-defect theory for slow atomic collisions*, Phys. Rev. A **72**, 042719 (2005).

[Gau10] S. Gautam and D. Angom, *Scattering length for fermionic alkali atoms*, The European Physical Journal D - Atomic, Molecular, Optical and Plasma Physics **56**, 173 (2010).

[Geh98] M. E. Gehm, K. M. O'Hara, T. A. Savard and J. E. Thomas, *Dynamics of noise-induced heating in atom traps*, Phys. Rev. A **58**, 3914 (1998).

[Geh03] M. E. Gehm, *Properties of ^6Li* (2003), http://www.phy.duke.edu/research/photon/qoptics/techdocs/pdf/PropertiesOfLi.pdf.

[Gio08] S. Giorgini, L. P. Pitaevskii and S. Stringari, *Theory of ultracold atomic Fermi gases*, Rev. Mod. Phys. **80**, 1215 (2008).

[Gün05] K. Günter, T. Stöferle, H. Moritz, M. Köhl and T. Esslinger, *p-Wave Interactions in Low-Dimensional Fermionic Gases*, Phys. Rev. Lett. **95**, 230401 (2005).

[Goo10] M. R. Goosen, T. G. Tiecke, W. Vassen and S. J. J. M. F. Kokkelmans, *Feshbach resonances in $^3He^*$-$^4He^*$ mixtures*, Phys. Rev. A **82**, 042713 (2010).

[Goz93] A. Gozzini, F. Mango, J. Xu, G. Alzetta, F. Maccarrone and R. Bernheim, *Light-induced ejection of alkali atoms in polysiloxane coated cells*, Il Nuovo Cimento D **15**, 709 (1993).

[Gre01] M. Greiner, I. Bloch, T. W. Hänsch and T. Esslinger, *Magnetic transport of trapped cold atoms over a large distance*, Phys. Rev. A **63**, 031401 (2001).

[Gre02] M. Greiner, O. Mandel, T. Esslinger, T. W. Hänsch and I. Bloch, *Quantum phase transition from a superfluid to a Mott insulator in a gas of ultracold atoms*, Nature (London) **415**, 39 (2002).

[Gre03] M. Greiner, C. A. Regal and D. S. Jin, *Emergence of a molecular Bose-Einstein condensate from a Fermi gas*, Nature (London) **426**, 537 (2003).

[Gri93] G. F. Gribakin and V. V. Flambaum, *Calculation of the scattering length in atomic collisions using the semiclassical approximation*, Phys. Rev. A **48**, 546 (1993).

[Gri00] R. Grimm, M. Weidemüller and Y. Ovchinnikov, *Optical Dipole Traps for Neutral Atoms*, Adv. At. Mol. Opt. Phys. **42**, 42 (2000).

[Gri05] P. F. Griffin, K. J. Weatherill and C. S. Adams, *Fast switching of alkali atom dispensers using laser-induced heating*, Review of Scientific Instruments **76**, 093102 (2005).

[Gus01] T. L. Gustavson, A. P. Chikkatur, A. E. Leanhardt, A. Görlitz, S. Gupta, D. E. Pritchard and W. Ketterle, *Transport of Bose-Einstein Condensates with Optical Tweezers*, Phys. Rev. Lett. **88**, 020401 (2001).

[Gus08] M. Gustavsson, E. Haller, M. J. Mark, J. G. Danzl, G. Rojas-Kopeinig and H.-C. Nägerl, *Control of Interaction-Induced Dephasing of Bloch Oscillations*, Phys. Rev. Lett. **100**, 080404 (2008).

[Ham10] H.-W. Hammer and L. Platter, *Efimov States in Nuclear and Particle Physics*, Annual Review of Nuclear and Particle Science **60**, 207 (2010).

[Han09] T. M. Hanna, E. Tiesinga and P. S. Julienne, *Prediction of Feshbach resonances from three input parameters*, Phys. Rev. A **79**, 040701 (2009).

[Han10] T. M. Hanna, E. Tiesinga and P. S. Julienne, *Creation and manipulation of Feshbach resonances with radiofrequency radiation*, New Journal of Physics **12**, 083031 (2010).

[Hap72] W. Happer, *Optical Pumping*, Rev. Mod. Phys. **44**, 169 (1972).

[Hec90] E. Hecht, *Optics* (Addison-Wesley, 1990).

[Heo11] M.-S. Heo, J.-y. Choi and Y.-i. Shin, *Fast production of large ^{23}Na Bose-Einstein condensates in an optically plugged magnetic quadrupole trap*, Phys. Rev. A **83**, 013622 (2011).

[Hes86] H. F. Hess, *Evaporative cooling of magnetically trapped and compressed spin-polarized hydrogen*, Phys. Rev. B **34**, 3476 (1986).

[Hut94] J. M. Hutson, *Coupled channel methods for solving the bound-state Schrödinger equation*, Comput. Phys. Commun. **84**, 1 (1994).

[Hut07] J. M. Hutson, *Feshbach resonances in ultracold atomic and molecular collisions: threshold behaviour and suppression of poles in scattering lengths*, New Journal of Physics **9**, 152 (2007).

[Ing07] M. Inguscio, W. Ketterle and C. Salomon (Editors), *Proceedings of the International School of Physics "Enrico Fermi", Course CLXIV, Ultra-cold Fermi Gases* (Società Italiana di Fisica and IOS Press Amsterdam, 2007).

[Ino98] S. Inouye, M. R. Andrews, J. Stenger, H.-J. Miesner, D. M. Stamper-Kurn and W. Ketterle, *Observation of Feshbach resonances in a Bose – Einstein condensate*, Nature **392**, 151 (1998).

[Ino04] S. Inouye, J. Goldwin, M. L. Olsen, C. Ticknor, J. L. Bohn and D. S. Jin, *Observation of Heteronuclear Feshbach Resonances in a Mixture of Bosons and Fermions*, Phys. Rev. Lett. **93**, 183201 (2004).

[Joc02] S. Jochim, M. Bartenstein, G. Hendl, J. H. Denschlag, R. Grimm, A. Mosk and M. Weidemüller, *Magnetic Field Control of Elastic Scattering in a Cold Gas of Fermionic Lithium Atoms*, Phys. Rev. Lett. **89**, 273202 (2002).

[Jof93] M. A. Joffe, W. Ketterle, A. Martin and D. E. Pritchard, *Transverse cooling and deflection of an atomic beam inside a Zeeman slower*, J. Opt. Soc. Am. B **10**, 2257 (1993).

[Joh73] B. R. Johnson, *The multichannel log-derivative method for scattering calculations*, J. Comput. Phys. **13**, 445 (1973).

[Jör08] R. Jördens, N. Strohmaier, K. Günter, H. Moritz and T. Esslinger, *A Mott insulator of fermionic atoms in an optical lattice*, Nature (London) **455**, 204 (2008).

[Jör10a] R. Jördens, *Metallic and Mott-insulating phases in fermionic quantum gases*, Ph.D. thesis, ETH Zürich (2010).

[Jör10b] R. Jördens, L. Tarruell, D. Greif, T. Uehlinger, N. Strohmaier, H. Moritz, T. Esslinger, L. De Leo, C. Kollath, A. Georges, V. Scarola, L. Pollet, E. Burovski, E. Kozik and M. Troyer, *Quantitative Determination of Temperature in the Approach to Magnetic Order of Ultracold Fermions in an Optical Lattice*, Phys. Rev. Lett. **104**, 180401 (2010).

[Kag96] Y. Kagan, E. L. Surkov and G. V. Shlyapnikov, *Evolution of a Bose-condensed gas under variations of the confining potential*, Phys. Rev. A **54**, R1753 (1996).

[Kau09] A. M. Kaufman, R. P. Anderson, T. M. Hanna, E. Tiesinga, P. S. Julienne and D. S. Hall, *Radio-frequency dressing of multiple Feshbach resonances*, Phys. Rev. A **80**, 050701 (2009).

[Ket92] W. Ketterle and D. E. Pritchard, *Trapping and focusing ground state atoms with static fields*, Applied Physics B: Lasers and Optics **54**, 403 (1992).

[Ket93] W. Ketterle, K. B. Davis, M. A. Joffe, A. Martin and D. E. Pritchard, *High densities of cold atoms in a dark spontaneous-force optical trap*, Phys. Rev. Lett. **70**, 2253 (1993).

[Ket96] W. Ketterle and N. V. Druten, *Evaporative Cooling of Trapped Atoms*, Advances In Atomic, Molecular, and Optical Physics **37**, 181 (1996).

[Ket99] W. Ketterle, D. S. Durfee and D. M. Stamper-Kurn, *Making, probing and understanding Bose-Einstein condensates*, ArXiv e-prints **9904:034** (1999).

[Köh05] T. Köhler, E. Tiesinga and P. S. Julienne, *Spontaneous Dissociation of Long-Range Feshbach Molecules*, Phys. Rev. Lett. **94**, 020402 (2005).

[Köh06] T. Köhler, K. Góral and P. S. Julienne, *Production of cold molecules via magnetically tunable Feshbach resonances*, Rev. Mod. Phys. **78**, 1311 (2006).

[Kla10] J. Klaers, J. Schmitt, F. Vewinger and M. Weitz, *Bose-Einstein condensation of photons in an optical microcavity*, Nature **468**, 545 (2010).

[Kle06] C. Klempt, T. van Zoest, T. Henninger, O. Topic, E. Rasel, W. Ertmer and J. Arlt, *Ultraviolet light-induced atom desorption for large rubidium and potassium magneto-optical traps*, Phys. Rev. A **73**, 013410 (2006).

[Kno11] S. Knoop, T. Schuster, R. Scelle, A. Trautmann, J. Appmeier, M. K. Oberthaler, E. Tiesinga and E. Tiemann, *Feshbach spectroscopy and analysis of the interaction potentials of ultracold sodium*, Phys. Rev. A **83**, 042704 (2011).

[Kok97] S. J. J. M. F. Kokkelmans, H. M. J. M. Boesten and B. J. Verhaar, *Role of collisions in creation of overlapping Bose condensates*, Phys. Rev. A **55**, R1589 (1997).

[Koo07] M. Koot, *Het maken van een diodelasersysteem voor het maken van een magneto-optische val van rubidium-atomen*, Master's thesis, University of Amsterdam (2007).

[Kra06] T. Kraemer, M. Mark, P. Waldburger, J. G. Danzl, C. Chin, B. Engeser, A. D. Lange, K. Pilch, A. Jaakkola, H.-C. Nägerl and R. Grimm, *Evidence for Efimov quantum states in an ultracold gas of caesium atoms*, Nature **440**, 315 (2006).

[LeB11] L. J. LeBlanc, *Exploring many-body physics with ultracold atoms*, Ph.D. thesis, University of Toronto (2011).

[Leg01] A. J. Leggett, *Bose-Einstein condensation in the alkali gases: Some fundamental concepts*, Rev. Mod. Phys. **73**, 307 (2001).

[Lev74] M. D. Levenson and N. Bloembergen, *Observation of Two-Photon Absorption without Doppler Broadening on the $3S-5S$ Transition in Sodium Vapor*, Phys. Rev. Lett. **32**, 645 (1974).

[Li08] Z. Li, S. Singh, T. V. Tscherbul and K. W. Madison, *Feshbach resonances in ultracold ^{85}Rb-^{87}Rb and ^{6}Li-^{87}Rb mixtures*, Phys. Rev. A **78**, 022710 (2008).

[Lis99] F. Lison, P. Schuh, D. Haubrich and D. Meschede, *High-brilliance Zeeman-slowed cesium atomic beam*, Phys. Rev. A **61**, 013405 (1999).

[Lof02] T. Loftus, C. A. Regal, C. Ticknor, J. L. Bohn and D. S. Jin, *Resonant Control of Elastic Collisions in an Optically Trapped Fermi Gas of Atoms*, Phys. Rev. Lett. **88**, 173201 (2002).

[Lui96] O. J. Luiten, M. W. Reynolds and J. T. M. Walraven, *Kinetic theory of the evaporative cooling of a trapped gas*, Phys. Rev. A **53**, 381 (1996).

[Maj32] E. Majorana, *Atomi orientati in campo magnetico variabile*, Il Nuovo Cimento **9**, 43 (1932).

[Man86] D. E. Manolopoulos, *An improved log derivative method for inelastic scattering*, J. Chem. Phys. **85**, 6425 (1986).

[Met99] H. Metcalf and P. van der Straten, *Laser Cooling and Trapping* (Springer, 1999).

[Met07] H. J. Metcalf and P. van der Straten, *Laser Cooling and Trapping of Neutral Atoms*, in T. G. Brown, K. Creath, H. Kogelnik, M. Kriss, J. Schmit and M. J. Weber (Editors), *The Optics Encyclopedia* (Wiley-VCH, 2007).

[Mey02] T. Meyrath and F. Schreck, *A Laboratory Control System for Cold Atom Experiments: Hardware and Software* (2002), http://www.nintaka.com.

[Mie96] F. M. Mies, C. J. Williams, P. S. Julienne and M. Krauss, *Estimating Bounds on Collisional Relaxation Rates of Spin-Polarized* ^{87}*Rb Atoms at Ultracold Temperatures*, J. Res. Natl. Inst. Stand. Technol. **101**, 521 (1996).

[Mil88] P. W. Milonni and J. H. Eberly, *Lasers* (Wiley, 1988).

[MK85] T. Mayer-Kuckuk, *Atomphysik* (Teubner, 1985).

[Mod99] G. Modugno, C. Benkö, P. Hannaford, G. Roati and M. Inguscio, *Sub-Doppler laser cooling of fermionic* ^{40}K *atoms*, Phys. Rev. A **60**, R3373 (1999).

[Moe95] A. J. Moerdijk, B. J. Verhaar and A. Axelsson, *Resonances in ultracold collisions of* ^{6}Li*,* ^{7}Li*, and* ^{23}Na, Phys. Rev. A **51**, 4852 (1995).

[Moo05] K. L. Moore, T. P. Purdy, K. W. Murch, S. Leslie, S. Gupta and D. M. Stamper-Kurn, *Collimated, single-pass atom source from a pulsed alkali metal dispenser for laser-cooling experiments*, Review of Scientific Instruments **76**, 023106 (2005).

[Nai05] D. S. Naik and C. Raman, *Optically plugged quadrupole trap for Bose-Einstein condensates*, Phys. Rev. A **71**, 033617 (2005).

[Nai11] D. Naik, A. Trenkwalder, C. Kohstall, F. M. Spiegelhalder, M. Zaccanti, G. Hendl, F. Schreck, R. Grimm, T. M. Hanna and P. S. Julienne, *Feshbach resonances in the* ^{6}Li-^{40}K *Fermi-Fermi mixture: elastic versus inelastic interactions*, The European Physical Journal D pages 1–11 (2011).

[New66] R. G. Newton, *Scattering theory of waves and particles* (Dover, New York, 1966).

[Ni08] K.-K. Ni, S. Ospelkaus, M. H. G. de Miranda, A. Pe'er, B. Neyenhuis, J. J. Zirbel, S. Kotochigova, P. S. Julienne, D. S. Jin and J. Ye, *A High Phase-Space-Density Gas of Polar Molecules*, Science **322**, 231 (2008).

[NIS10] NIST (National Institute of Standards and Technology), *Physical Reference Data* (2010), http://physics.nist.gov/cuu/Constants/index.html.

[NIS11] NIST (National Institute of Standards and Technology), *Digital Library of Mathematical Functions* (2011), http://dlmf.nist.gov/4.13.

[NND11] NNDC (National Nuclear Data Center, Brookhaven National Laboratory), *Nuclear Structure and Decay Databases* (2011), http://www.nndc.bnl.gov.

[O'H02] K. M. O'Hara, S. L. Hemmer, S. R. Granade, M. E. Gehm, J. E. Thomas, V. Venturi, E. Tiesinga and C. J. Williams, *Measurement of the zero crossing in a Feshbach resonance of fermionic* $6Li$, Phys. Rev. A **66**, 041401 (2002).

[Oh08] S. Oh, Z. Huang, U. Peskin and S. Kais, *Entanglement, Berry phases, and level crossings for the atomic Breit-Rabi Hamiltonian*, Phys. Rev. A **78**, 062106 (2008).

[Ono00] R. Onofrio, D. S. Durfee, C. Raman, M. Köhl, C. E. Kuklewicz and W. Ketterle, *Surface Excitations of a Bose-Einstein Condensate*, Phys. Rev. Lett. **84**, 810 (2000).

[OS06] S. Ospelkaus-Schwarzer, *Quantum Degenerate Fermi-Bose Mixtures of* ^{40}K *and* ^{87}Rb *in 3D Optical Lattices*, Ph.D. thesis, University of Hamburg (2006).

[Osp06a] C. Ospelkaus, S. Ospelkaus, L. Humbert, P. Ernst, K. Sengstock and K. Bongs, *Ultracold Heteronuclear Molecules in a 3D Optical Lattice*, Phys. Rev. Lett. **97**, 120402 (2006).

[Osp06b] C. Ospelkaus, S. Ospelkaus, K. Sengstock and K. Bongs, *Interaction-Driven Dynamics of* $^{40}K - ^{87}$ *Rb Fermion-Boson Gas Mixtures in the Large-Particle-Number Limit*, Phys. Rev. Lett. **96**, 020401 (2006).

[Osp06c] S. Ospelkaus, C. Ospelkaus, L. Humbert, K. Sengstock and K. Bongs, *Tuning of Heteronuclear Interactions in a Degenerate Fermi-Bose Mixture*, Phys. Rev. Lett. **97**, 120403 (2006).

[Osp10] S. Ospelkaus, K.-K. Ni, D. Wang, M. H. G. de Miranda, B. Neyenhuis, G. Quemener, P. S. Julienne, J. L. Bohn, D. S. Jin and J. Ye, *Quantum-State Controlled Chemical Reactions of Ultracold Potassium-Rubidium Molecules*, Science **327**, 853 (2010).

[Pap10] D. J. Papoular, G. V. Shlyapnikov and J. Dalibard, *Microwave-induced Fano-Feshbach resonances*, Phys. Rev. A **81**, 041603 (2010).

[Pau25] W. Pauli, *Über den Zusammenhang des Abschlusses der Elektronengruppen im Atom mit der Komplexstruktur der Spektren*, Zeitschrift für Physik A Hadrons and Nuclei **31**, 765 (1925).

[Pet02] C. J. Pethick and H. Smith, *Bose-Einstein Condensation in Dilute Gases* (Cambridge University Press, 2002).

[Pet04] D. S. Petrov, *Three-Boson Problem near a Narrow Feshbach Resonance*, Phys. Rev. Lett. **93**, 143201 (2004).

[Pri83] D. E. Pritchard, *Cooling Neutral Atoms in a Magnetic Trap for Precision Spectroscopy*, Phys. Rev. Lett. **51**, 1336 (1983).

[Raa87] E. L. Raab, M. Prentiss, A. Cable, S. Chu and D. E. Pritchard, *Trapping of Neutral Sodium Atoms with Radiation Pressure*, Phys. Rev. Lett. **59**, 2631 (1987).

[Reg03a] C. A. Regal and D. S. Jin, *Measurement of Positive and Negative Scattering Lengths in a Fermi Gas of Atoms*, Phys. Rev. Lett. **90**, 230404 (2003).

[Reg03b] C. A. Regal, C. Ticknor, J. L. Bohn and D. S. Jin, *Creation of ultracold molecules from a Fermi gas of atoms*, Nature (London) **424**, 47 (2003).

[Reg03c] C. A. Regal, C. Ticknor, J. L. Bohn and D. S. Jin, *Tuning p-Wave Interactions in an Ultracold Fermi Gas of Atoms*, Phys. Rev. Lett. **90**, 053201 (2003).

[Reg04] C. A. Regal, M. Greiner and D. S. Jin, *Observation of Resonance Condensation of Fermionic Atom Pairs*, Phys. Rev. Lett. **92**, 040403 (2004).

[Reg06] C. A. Regal, *Experimental realization of BCS-BEC crossover physics with a Fermi gas of atoms*, Ph.D. thesis, University of Colorado (2006).

[Ric95] L. Ricci, M. Weidemüller, T. Esslinger, A. Hemmerich, C. Zimmermann, V. Vuletic, W. König and T. W. Hänsch, *A compact grating-stabilized diode laser system for atomic physics*, Optics Communications **117**, 541 (1995).

[Rid11a] A. Ridinger, *Towards quantum degenerate Fermi mixtures: Photoassociation of weakly bound ^6Li – ^{40}K molecules*, Ph.D. thesis, University Pierre and Marie Curie (Paris VI) (2011).

[Rid11b] A. Ridinger, S. Chaudhuri, T. Salez, U. Eismann, D. Rio Fernandes, D. Wilkowski, F. Chevy and C. Salomon, *Large atom number dual-species magneto-optical trap for fermionic ^6Li and ^{40}K atoms*, ArXiv e-prints **1103.0637** (2011).

[Roa02] G. Roati, F. Riboli, G. Modugno and M. Inguscio, *Fermi-Bose Quantum Degenerate ^{40}K-^{87}Rb Mixture with Attractive Interaction*, Phys. Rev. Lett. **89**, 150403 (2002).

[Roa08] G. Roati, C. D/'Errico, L. Fallani, M. Fattori, C. Fort, M. Zaccanti, G. Modugno, M. Modugno and M. Inguscio, *Anderson localization of a non-interacting Bose-Einstein condensate*, Nature **453**, 895 (2008).

[Rub81] J. R. Rubbmark, M. M. Kash, M. G. Littman and D. Kleppner, *Dynamical effects at avoided level crossings: A study of the Landau-Zener effect using Rydberg atoms*, Phys. Rev. A **23**, 3107 (1981).

[Sak94] J. J. Sakurai, *Modern Quantum Mechanics (Revised Edition)* (Addison-Wesley, 1994).

[Sav97] T. A. Savard, K. M. O'Hara and J. E. Thomas, *Laser-noise-induced heating in far-off resonance optical traps*, Phys. Rev. A **56**, R1095 (1997).

[Sch99] U. Schünemann, H. Engler, R. Grimm, M. Weidemüller and M. Zielonkowski, *Simple scheme for tunable frequency offset locking of two lasers*, Review of Scientific Instruments **70**, 242 (1999).

[Sch02] J. Schoser, A. Batär, R. Löw, V. Schweikhard, A. Grabowski, Y. B. Ovchinnikov and T. Pfau, *Intense source of cold Rb atoms from a pure two-dimensional magneto-optical trap*, Phys. Rev. A **66**, 023410 (2002).

[Sch08] U. Schneider, L. Hackermüller, S. Will, T. Best, I. Bloch, T. A. Costi, R. W. Helmes, D. Rasch and A. Rosch, *Metallic and Insulating Phases of Repulsively Interacting Fermions in a 3D Optical Lattice*, Science **322**, 1520 (2008).

[Sch10] U. Schneider, L. Hackermüller, J. P. Ronzheimer, S. Will, S. Braun, T. Best, I. Bloch, E. Demler, S. Mandt, D. Rasch and A. Rosch, *Breakdown of diffusion: From collisional hydrodynamics to a continuous quantum walk in a homogeneous Hubbard model*, ArXiv e-prints **1005.3545** (2010).

[Sco06] T. C. Scott, R. Mann and R. E. Martinez II, *General relativity and quantum mechanics: towards a generalization of the Lambert $\mathcal{W}$ function*, Applicable Algebra in Engineering, Communication and Computing **17**, 41 (2006), or ArXiv e-prints **0607011**(2006).

[Sil05] C. Silber, S. Günther, C. Marzok, B. Deh, P. W. Courteille and C. Zimmermann, *Quantum-Degenerate Mixture of Fermionic Lithium and Bosonic Rubidium Gases*, Phys. Rev. Lett. **95**, 170408 (2005).

[Sim03] A. Simoni, F. Ferlaino, G. Roati, G. Modugno and M. Inguscio, *Magnetic Control of the Interaction in Ultracold K-Rb Mixtures*, Phys. Rev. Lett. **90**, 163202 (2003).

[Slo05] C. Slowe, L. Vernac and L. V. Hau, *High flux source of cold rubidium atoms*, Review of Scientific Instruments **76**, 103101 (2005).

[Smi11] R. P. Smith, R. L. D. Campbell, N. Tammuz and Z. Hadzibabic, *Effects of Interactions on the Critical Temperature of a Trapped Bose Gas*, Phys. Rev. Lett. **106**, 250403 (2011).

[Spi09] F. M. Spiegelhalder, A. Trenkwalder, D. Naik, G. Hendl, F. Schreck and R. Grimm, *Collisional Stability of ^{40}K Immersed in a Strongly Interacting Fermi Gas of ^{6}Li*, Phys. Rev. Lett. **103**, 223203 (2009).

[Sta05] C. A. Stan and W. Ketterle, *Multiple species atom source for laser-cooling experiments*, Review of Scientific Instruments **76**, 063113 (2005).

[Sta07] K. M. R. van der Stam, E. D. van Ooijen, R. Meppelink, J. M. Vogels and P. van der Straten, *Large atom number Bose-Einstein condensate of sodium*, Review of Scientific Instruments **78**, 013102 (2007).

[Ste08] J. T. Stewart, J. P. Gaebler and D. S. Jin, *Using photoemission spectroscopy to probe a strongly interacting Fermi gas*, Nature (London) **454**, 744 (2008).

[Ste10] D. A. Steck, *Alkali D Line Data* (2010), http://steck.us/alkalidata/.

[Ste11] W. Steinbrecht, U. Köhler, H. Claude, M. Weber, J. P. Burrows and R. J. van der A, *Very high ozone columns at northern mid-latitudes in 2010*, Geophys. Res. Lett. **38**, L06803 (2011).

[Sto88] H. T. C. Stoof, J. M. V. A. Koelman and B. J. Verhaar, *Spin-exchange and dipole relaxation rates in atomic hydrogen: Rigorous and simplified calculations*, Phys. Rev. B **38**, 4688 (1988).

[Str10] N. Strohmaier, D. Greif, R. Jördens, L. Tarruell, H. Moritz, T. Esslinger, R. Sensarma, D. Pekker, E. Altman and E. Demler, *Observation of Elastic Doublon Decay in the Fermi-Hubbard Model*, Phys. Rev. Lett. **104**, 080401 (2010).

[Stu04] A. Stummer, *Mag-O-Matic – BEC/MT/MOT Coils* (2004), http://www.physics.utoronto.ca/~astummer/pub/mirror/Projects/Archives/2004%20BEC%20Coil%20Driver%20%27Mag-O-Matic%27/BEC_coils.html.

[Tag06] M. Taglieber, A.-C. Voigt, F. Henkel, S. Fray, T. W. Hänsch and K. Dieckmann, *Simultaneous magneto-optical trapping of three atomic species*, Phys. Rev. A **73**, 011402 (2006).

[Tay72] J. R. Taylor, *Scattering theory* (Dover, New York, 1972).

[Tic04] C. Ticknor, C. A. Regal, D. S. Jin and J. L. Bohn, *Multiplet structure of Feshbach resonances in nonzero partial waves*, Phys. Rev. A **69**, 042712 (2004).

[Tie92] E. Tiesinga, A. J. Moerdijk, B. J. Verhaar and H. T. C. Stoof, *Conditions for Bose-Einstein condensation in magnetically trapped atomic cesium*, Phys. Rev. A **46**, R1167 (1992).

[Tie93] E. Tiesinga, B. J. Verhaar and H. T. C. Stoof, *Threshold and resonance phenomena in ultracold ground-state collisions*, Phys. Rev. A **47**, 4114 (1993).

[Tie09a] T. G. Tiecke, *Feshbach resonances in ultracold mixtures of the fermionic quantum gases ^6Li and ^{40}K*, Ph.D. thesis, University of Amsterdam (2009).

[Tie09b] T. G. Tiecke, S. D. Gensemer, A. Ludewig and J. T. M. Walraven, *High-flux two-dimensional magneto-optical-trap source for cold lithium atoms*, Phys. Rev. A **80**, 013409 (2009).

[Tie10a] T. G. Tiecke, *Properties of Potassium* (2010), http://www.tobiastiecke.nl/archive/PotassiumProperties.pdf.

[Tie10b] T. G. Tiecke, M. R. Goosen, A. Ludewig, S. D. Gensemer, S. Kraft, S. J. J. M. F. Kokkelmans and J. T. M. Walraven, *Broad Feshbach Resonance in the ^6Li-^{40}K Mixture*, Phys. Rev. Lett. **104**, 053202 (2010).

[Tie10c] T. G. Tiecke, M. R. Goosen, J. T. M. Walraven and S. J. J. M. F. Kokkelmans, *Asymptotic-bound-state model for Feshbach resonances*, Phys. Rev. A **82**, 042712 (2010).

[Tsc10] T. V. Tscherbul, T. Calarco, I. Lesanovsky, R. V. Krems, A. Dalgarno and J. Schmiedmayer, *rf-field-induced Feshbach resonances*, Phys. Rev. A **81**, 050701 (2010).

[Ver09] B. J. Verhaar, E. G. M. van Kempen and S. J. J. M. F. Kokkelmans, *Predicting scattering properties of ultracold atoms: Adiabatic accumulated phase method and mass scaling*, Phys. Rev. A **79**, 032711 (2009).

[Voi09] A.-C. Voigt, M. Taglieber, L. Costa, T. Aoki, W. Wieser, T. W. Hänsch and K. Dieckmann, *Ultracold Heteronuclear Fermi-Fermi Molecules*, Phys. Rev. Lett. **102**, 020405 (2009).

[Wal96] J. T. M. Walraven, *Atomic Hydrogen in magnetostatic traps*, in G.-L. Oppo, S. Barnett, E. Riis and M. Wilkinson (Editors), *Quantum Dynamics of Simple Systems* (IOP, Bristol, 1996).

[Wal10] J. T. M. Walraven, *Elements of Quantum Gases: Thermodynamic and Collisional Properties of Trapped Atomic Gases*, Les Houches lectures, unpublished (2010).

[Wan97] H. Wang, P. L. Gould and W. C. Stwalley, *Long-range interaction of the $^{39}K(4s)+^{39}K(4p)$ asymptote by photoassociative spectroscopy. I. The 0_g^- pure long-range state and the long-range potential constants*, The Journal of Chemical Physics **106**, 7899 (1997).

[WI97] R. S. Williamson III, *Magneto-optical trapping of potassium isotopes*, Ph.D. thesis, University of Wisconsin (1997).

[Wil08] E. Wille, F. M. Spiegelhalder, G. Kerner, D. Naik, A. Trenkwalder, G. Hendl, F. Schreck, R. Grimm, T. G. Tiecke, J. T. M. Walraven, S. J. J. M. F. Kokkelmans, E. Tiesinga and P. S. Julienne, *Exploring an Ultracold Fermi-Fermi Mixture: Interspecies Feshbach Resonances and Scattering Properties of ^6Li and ^{40}K*, Phys. Rev. Lett. **100**, 053201 (2008).

[Wit11] J. de Wit, *personal communication* (2011).

[Wu11] C.-H. Wu, I. Santiago, J. W. Park, P. Ahmadi and M. W. Zwierlein, *Strongly interacting isotopic Bose-Fermi mixture immersed in a Fermi sea*, Phys. Rev. A **84**, 011601 (2011).

[Zac42] J. R. Zacharias, *The Nuclear Spin and Magnetic Moment of* 40^K, Phys. Rev. **61**, 270 (1942).

[Zir08a] J. J. Zirbel, K.-K. Ni, S. Ospelkaus, J. P. D'Incao, C. E. Wieman, J. Ye and D. S. Jin, *Collisional Stability of Fermionic Feshbach Molecules*, Phys. Rev. Lett. **100**, 143201 (2008).

[Zir08b] J. J. Zirbel, K.-K. Ni, S. Ospelkaus, T. L. Nicholson, M. L. Olsen, P. S. Julienne, C. E. Wieman, J. Ye and D. S. Jin, *Heteronuclear molecules in an optical dipole trap*, Phys. Rev. A **78**, 013416 (2008).

[Zwi05] M. W. Zwierlein, J. R. Abo-Shaeer, A. Schirotzek, C. H. Schunck and W. Ketterle, *Vortices and superfluidity in a strongly interacting Fermi gas*, Nature **435**, 1047 (2005).

Summary

This thesis presents the measurement of Feshbach resonances in various hyperfine state mixtures of ultracold ^{40}K. Feshbach resonances can be used to tune the strength and the sign of the interaction between atoms. With this tool ultracold atoms can be used as a model system for other problems in physics. For very strongly interacting atoms only a few universal parameters are required to describe the system. Systems with entirely different underlying processes, such as for example neutron stars or superconductors, might share the same parameters and can then be compared to the strongly interacting cold atoms.

Feshbach resonances in neutral atoms occur when the energy of two colliding unbound atoms is in resonance with the energy of a bound state of the two atoms. When the magnetic moment of the bound pair differs from the unbound pair, the energy difference can be tuned into resonance by applying a magnetic field. Around the resonance the scattering length, which is a measure for the interaction strength, diverges. By changing an applied magnetic field the interaction of the atoms can be tuned from attractive to repulsive and vice versa. Close to the resonance the interaction becomes so strong that the two-body mean field description breaks down and new theories are necessary.

The positions and widths of Feshbach resonances of an atomic species in a specific state depend on the interatomic potential which differs for different species and different states. Before Feshbach resonances can be used as a tool to tune the interaction, their positions and properties need to be determined. The theoretical description of Feshbach resonances is presented in Chapter 2.

To be able to make use of Feshbach resonances the temperature of the atoms needs to be close to the absolute zero (-273.15 °C), otherwise the kinetic energy of the atoms would smear out the effect. The experimental setup and the techniques to trap and cool the atoms to such low temperatures are described in Chapter 3. At those very low temperatures the behaviour of the atoms is governed by quantum statistics and the division of the particles in two distinct classes - bosons and fermions - manifests itself. Bosons can condense into a single state and form a macroscopic wavefunction extending over the inter-particle distance. Bosonic atoms can be made to display interference patterns; something which is at room temperature only possible for light.

For fermions, the behaviour at low temperatures is very different from bosons: instead of condensing into a single state they each occupy a state by themselves, keeping their distance. The quantum statistics of fermions plays an important role in many areas of physics. In condensed matter Fermi statistics determines electric and transport properties, neutron stars are prevented from collapsing by Fermi pressure and all

matter known to us is composed of quarks and electrons which are fermionic elementary particles. For the understanding of superconductivity the pairing of fermions with attractive interactions plays a major role.

We work with the fermionic potassium isotope ^{40}K in the experiments described in this thesis. ^{40}K has a rich hyperfine structure with many stable combinations of hyperfine states. Each binary combination of hyperfine states can show Feshbach resonances at various fields, sometimes close in magnetic field to or even overlapping with another Feshbach resonance in a different hyperfine state combination. It is therefore important to prepare mixtures of only the desired states as described in Chapter 4. Additionally there are also various kinds of resonances; relevant in our case are s-wave resonances which only occur between atoms in non-identical states and p-wave resonances which are allowed also between identical states. In addition, the shape and position of p-wave resonances depends on the temperature and the projection of the atoms' magnetic moment on the axis of the magnetic field.

Prior to the results presented in this thesis the position of four Feshbach resonances in mixtures of ^{40}K in the three lowest hyperfine states were known. In this thesis we present measurements on mixtures occupying states in the middle of the hyperfine manifold of ^{40}K. Overall we measured 10 s-wave resonances in 4 state mixtures and 13 p-wave resonances in 8 different binary mixtures. Among the s-wave resonances we identified in the $c + d$ mixture a resonance which is isolated from other resonances by about 55 G. For the same Feshbach resonance we determined the width by evaporating the cold cloud at different magnetic fields and measuring the magnetic field dependent cloud size.

In the $j+h$ mixture there is a p-wave resonance around the same magnetic field as a p-wave resonance in the $i+i$ mixture. On resonance the atoms in the $j+h$ channel are not entirely lost from the optical dipole trap, but appear in the i state. The resonance in the $i+i$ channel displays a multiplet feature caused by the dipole-dipole coupling to the $i+j$, $i+h$ and the $h+h$ channels. The results of those measurements are presented in Chapters 4 and 5.

The measured Feshbach resonances are useful for the development and improvement of simple theories. The experimental data was used by our collaborators as a test ground for two simple models, the asymptotic bound state model (ABM) and the multi quantum defect theory (MQDT). The values obtained with coupled channel calculations (CC) using the currently known potentials for ^{40}K were all within the experimental uncertainty of the measured values.

With the mapping out of the Feshbach resonances in ^{40}K it is now easier to chose the Feshbach resonances where side effects of other resonances can be neglected. This is of importance not only for experiments using ^{40}K alone, but also for experiments with mixtures with other atomic species. Depending on the requirements for an experiment, the most convenient Feshbach resonance can be located.

Samenvatting

Dit proefschrift presenteert de meting van Feshbach-resonanties in mengsels van verschillende hyperfijntoestanden van ultrakoud ^{40}K. Feshbach-resonanties kunnen worden gebruikt om de sterkte en het teken van de wisselwerking tussen atomen in te stellen. Met dit werktuig kunnen ultrakoude atomen worden gebruikt als een modelsysteem voor andere problemen in de natuurkunde. In het geval van zeer sterk wisselwerkende atomen zijn er slechts een paar universele parameters nodig om het systeem te beschrijven. Systemen met helemaal andere onderliggende processen, zoals bijvoorbeeld neutronensterren of supergeleiders, zouden dezelfde parameters kunnen delen en dan met de sterk wisselwerking koude atomen vergeleken kunnen worden.

In neutrale atomen komen Feshbach-resonanties voor wanneer de energie van twee botsende ongebonden atomen in resonantie is met de energie van een gebonden toestand van de twee atomen. Wanneer het magnetisch moment van het gebonden paar afwijkt van het ongebonden paar, kan het energieverschil in resonantie worden gebracht door het aanzetten van een magnetisch veld. Rondom de resonantie divergeert de strooilengte, een maat voor de wisselwerkingssterkte. Door het veranderen van het toegepast magnetisch veld kan de wisselwerking tussen de atomen van aantrekkend tot afstotend en vice versa ingesteld worden. Dicht bij de resonantie wordt de wisselwerking zó sterk, dat beschrijving door een theorie waar de deeltjes een veld ervaren, dat alleen van de twee-deeltjes wisselwerking afhangt, niet meer werkt en nieuwe theorieën nodig zijn. De posities en breedtes van Feshbach-resonanties zijn afhankelijk van het interatomaire potentiaal wat verschilt voor verschillende atoomsoorten en toestanden. Voordat Feshbach-resonanties kunnen worden gebruikt als een instrument om de wisselwerking in te stellen, moeten hun posities en eigenschappen worden bepaald. De theoretische beschrijving van Feshbach-resonanties is te vinden in hoofdstuk 2.

Om gebruik te kunnen maken van Feshbach resonanties moet de temperatuur van de atomen dicht bij het absolute nulpunt (-273.15 °C) zijn, anders zou de kinetische energie van de atomen het effect verbergen. De experimentele opstelling en de technieken om de atomen te vangen en tot zulke lage temperaturen te koelen worden in hoofdstuk 3 beschreven. Bij deze zeer lage temperaturen wordt het gedrag van de atomen beheerst door quantumstatistiek en de opdeling van de deeltjes in twee verschillende klassen - bosonen en fermionen - manifesteert zich. Bosonen kunnen in een enkele toestand condenseren en vormen een macroscopische golffunctie die groter is dan de afstand tussen de deeltjes. Bosonische atomen kunnen interferentiepatronen vormen, iets dat op kamertemperatuur alleen te doen is met licht.

Voor fermionen is het gedrag bij lage temperaturen heel anders dan voor bosonen: in plaats van condensatie in één toestand bezetten ze elk een aparte toestand en

houden ze afstand van elkaar. De quantumstatistiek van fermionen speelt een belangrijke rol in veel gebieden van de natuurkunde. In gecondenseerde materie bepaalt de Fermi-statistiek elektrische en transport-eigenschappen, neutronensterren storten niet in vanwege de Fermi-druk en alle materie die ons bekend is, bestaat uit quarks en elektronen - fermionische elementaire deeltjes. Voor het begrijpen van supergeleiding speelt de koppeling van fermionen met aantrekkende wisselwerking een belangrijke rol.

In de in dit proefschrift beschreven experimenten werken we met het fermionsich kalium isotoop ^{40}K, wat een rijke hyperfijnstructuur met veel stabiele combinaties van hyperfijntoestanden heeft. Elke binaire combinatie van hyperfijntoestanden kan bij diverse magneetvelden Feshbach-resonanties tonen, soms dicht bij elkaar in magnetisch veld of zelfs overlappend met een andere Feshbach-resonantie van een andere combinatie van hyperfijntoestanden. Daarnaast zijn er ook verschillende soorten resonanties; relevant in ons geval zijn s-golf resonanties die alleen optreden tussen atomen in niet-identieke toestanden en p-golf resonanties die ook zijn toegestaan tussen identieke toestanden. Daarnaast is de vorm en positie van p-golf resonanties afhankelijk van de temperatuur en de projectie van het magnetisch moment van de atomen op de as van het magnetisch veld.

Voorafgaand aan de resultaten gepresenteerd in dit proefschrift was de positie van vier Feshbach-resonanties in mengsels van ^{40}K in de drie laagste hyperfijnniveaus bekend. In dit proefschrift presenteren we metingen op mengsels van toestanden uit het midden van de hyperfijntoestands-"waaier" van ^{40}K. In totaal hebben we 10 s-golf resonanties gemeten in 4 verschillende mengsels en 13 p-golf resonanties in 8 verschillende binaire mengsels. Onder de s-golf resonanties hebben we er een gevonden in het $c + d$ mengsel, die op een afstand van circa 55 G van aangrenzende resonanties ligt. Voor dezelfde Feshbach-resonantie hebben we de breedte bepaald door het verdampen van de koude wolk bij verschillende magnetische velden en het meten van de veldafhankelijke wolkgrootte.

In het $j + h$ mengsel is er een p-golf resonantie rond hetzelfde magnetisch veld als bij een p-golf resonantie in het $i + i$ mengsel. Bij de resonantie vallen de atomen in het $j + h$ kanaal niet allemaal zoals verwacht uit de optische dipoolval, maar verschijnen ze in de i toestand. De resonantie in het $i + i$ kanaal toont een multipletstruktuur veroorzaakt door de dipool-dipool koppeling aan de $i + j$, $i + h$ en de $h + h$-kanalen. De resultaten van deze metingen worden gepresenteerd in hoofdstuk 4 en 5.

De gemeten Feshbach-resonanties zijn nuttig voor de ontwikkeling en verbetering van eenvoudige theorieën. De experimentele data is door samenwerkende theoretici als proeftuin voor twee eenvoudige modellen gebruikt, de asymptotische gebonden toestand model (ABM) en de multi quantum defect theorie (MQDT). De met gekoppelde kanaal theorie (CC) berekende waarden (met behulp van de op dat moment bekende potentialen voor ^{40}K) waren allemaal binnen de experimentele onzekerheid van de gemeten waarden.

Met het in kaart brengen van de Feshbach-resonanties in ^{40}K is het nu gemakkelijker om de Feshbach-resonanties uit te kiezen waar neveneffekten van andere resonanties kunnen worden verwaarloosd. Dit is niet alleen van belang voor experimenten met enkel ^{40}K, maar ook voor experimenten met mengsels met andere atomaire soorten. Afhankelijk van de vereisten voor een experiment, kan de best passende Feshbach-resonantie worden gelokaliseerd.

Acknowledgements

Over the past years a lot of people have contributed to my work, on a professional basis or by keeping my spirits up and showing me support. Out of pure forgetfulness I will certainly omit some in my acknowledgements - I am sorry about this and please feel deeply thanked nevertheless.

First of all, I would like to thank my supervisor Jook Walraven. It has been truly inspirational to work with you. There is something to be learned and understood from every problem - be it the thermalization in the lab due to severe weather conditions or some – at first – inexplicable observation during the measurements. You taught me that with perseverance, some reading up and hard thinking anything can be tackled eventually. Aside from the work in the lab and at the whiteboard, you were always very supportive and generous about allowing me to attend summer schools and conferences where I made many valuable new contacts and was able to stay in touch with researchers from my home country. In the lab you offered us great freedom to make decisions and choose our own direction of work, thank you for that.

When I first started my PhD-project, Steve Gensemer was the postdoc in the lab. Steve, you were a great teacher for me, especially in the art of electronics, where I had hardly any experience. You were helpful and accepted that a PhD is first of all a very steep learning curve. Outside the lab, you also allowed me to introduce you to the big variety of European (beer) culture and during the regular dinners at some Pizza place or the mensa we had great discussions and fun before going back to the lab. Thank you for all of this.

Sebastian Kraft, the second postdoc whom I worked with, you showed me that the slope of the learning curve is indeed positive and you were a great motivator for me. You showed great interest in what I was working on and gave new input when I got stuck with something. In discussions about physics you were never patronizing to me, but showed socratic teaching skills, thank you very much for that.

The person I probably spent the most time with in that dark cellar lab, was my co-worker Tobias Tiecke. Tobias, it was great to work with you, thanks a lot for everything. You were the driving force in the lab, keeping the overview and the bigger picture in sight. Without your knowledge and abilities the experiment and the work in the lab would not have been the same. You were generous in sharing your knowledge and I learned a lot from you. We celebrated successes, suffered setbacks together and kept each other motivated and positive. Once you had left for Harvard you continued your support and kept an interest in what was happening in Amsterdam.

I would like to thank all the people who are involved in the mammoth project of the ^{40}K Feshbach resonance paper, especially: Liam Cook, Maikel Goosen, Tom Hanna

and Servaas Kokkelmans. It was great to get input from the theoretical side and then be able to deliver the measurements which were of special interest. The meeting we had together was very productive and inspiring. I am also deeply grateful for your goal-oriented approach.

There is probably not a single person from the UvA-workshops who has not contributed to our experimental setup. Big projects like the coil-switch, the Feshbach coils, the heated spectroscopy cell, but also small things like quickly supplying the right screw or soldering a too-many-pins connector were always in good hands with the people at the workshops. In emergencies you went the extra mile and found me another power supply for the heart of our experiment or loaned me some equipment. Hartstikke bedankt Ron Manuputy, Mattijs Bakker, Hans Ellermeijer, Eric Hennes, Udo van Hes, Cees van den Biggelaar, Harry Beukers, Wim van Aartsen, Fred van Anrooij, Wietse Buster, Tjerk van Goudoever, Jan Kalwij, Farah Kuckulus, Diederick Kwakkestijn, Ben Klein-Meulekamp, Henk Luijten, Joost Overtoom, Jur Pluim, Johan Soede, Daan de Zwarte, Theo van Lieshout, Hans Agema, Herman Prins, Pieter Sannes, Johan te Winkel, Edwin Baay, Frans Pinkse, Alof Wassink, Ed de Water, Hans Gerritsen, Gerrit Hardeman, Ben Harrison, Taco Walstra en Bert Zwart. Thank you (and the people I might have forgotten) for all your hard work and the friendly and supportive atmosphere.

I would like to thank the quantum gases group: Tom Hijmans, thanks for the numerous times we took the world apart and put it back together and of course for sharing your intuitive views on physics. Ben van Linden van den Heuvell, you were a great help with Mathematica and all physics questions. Shannon Whitlock, you were a great postdoc for me even though you worked on a different project. I really enjoyed the evenings with you, Angie, Carolijn van Ditzhuijzen and René Gerritsma at the Wildeman. Paul Cleary, you were a very helpful and cheerful next-door neighbour. Phil Wicke, danke für all das gemeinsame Aufregen und Abkotzen und dann doch wieder über andere Dinge reden und was normales machen, wie zu 'nem Konzert gehen oder so. Richard Newell, thanks for the entertainment with your encyclopaedic knowledge and the good times spent together. Atreju Tauschinsky, Dir und Ela danke für viele schöne Gespräche. Thanks to all the other people who helped me with minor or major problems: Gora Shlyapnikov, Klaasjan van Druten, Robert Spreeuw, Vanessa Leung, Wojciech Lewoczko-Adamczyk, Micha Baranov, Piotr Deuar, Dima Petrov, Jan-Joris van Es, Aaldert van Amerongen, Thomas Fernholz, Vlad Ivanov and Iuliana Barb. Frederik Spiegelhalder and Slava Lebedev have been working on the experiment after I left the lab and had the difficult job of rebuilding everything after the move to the new building. All the best for your future endeavours! Thanks to all the people from the quantum gases group for the friendly and cooperative atmosphere and the many good discussions.

From the administration I would like to thank Rita Vinig, Ineke Baas and Luuk Lusink. Apart from showing interest in my progress, you also saved me twice from becoming homeless. Meinen ehemaligen Lehrern Dagmar Geyer, Gregor Milla und Werner Rall möchte ich danken für ihre Anregungen, Einsichten und den wissenschaftlichen Stil, den sie vermittelt haben. Meine Entscheidung für ein (Physik-)Studium war sicherlich mitgeprägt durch diese positiven Erlebnisse in meiner Schulzeit.

At the institute I also had tremendous fun organizing fun things for others with the social club of the WZI and later also the ITF social club. Thanks to Joost, Alessia,

Jan-Joris, Sanne, Bahar, Liza, Balt and others for that. A lot of my social life evolved around the fluctuating group of ex-pats at the WZI and the ITF. A drink at Kriterion, a barbecue in Oosterpark, a dinner party – there were always wonderful people to spend time with. Bedankt, Merci, Mamnoon, Gracias, Grazie to Rob (for my first Dutch lessons and your paranimfen choice), Jérémie, Sara (for all the nights at the movies), Pasquale (for all the Sundays in a museum and all the cooking), Alessia, Salima, Nacho, Kuba, Salvo, Bahar and Sanli (for the Farsi lessons), ...

Dank aan de 'Three imaginary boys' en entourage: Felix, Frank, Maurice, Richard en Christine, Miriam, ... - altijd gezellig samen met jullie gewoon kunst, kultuur en 'n borrel te genieten. Theo en Olga, jullie zijn zo 'n beetje mijn Nederlandse familie geworden, dank jullie voor alle steun.

Dank auch all jenen Freunden, die mich aus der Ferne so lieb unterstützt haben: Anne Müller und Kathrin Leßner, immer wieder bekomme ich Anrufe und Post von Euch, auch wenn ich mich selbst zwischendurch gar nicht mehr melde. Kai Freund, danke für Deine Postkarten und Maultaschenlieferungen. Katharina Schäfer, wie oft hast Du mir Mut gemacht, Dir über skype meine Sorgen angehört um mir am nächsten Tag gleich ein Wohlfühlpaket zu schicken. Vielen Dank Ihr Lieben! Baie dankie aan my 'bhuti' Hencharl, jy is 'n goeie vriend en sonder jou het ek nooit koue atoom fysika gekies nie. Meinen Geschwistern, Dagmar und Bodo, danke ich für die aufmunternden Gespräche, die nie nachlassende Anteilnahme und Solidarität und die schönen Besuche.

Beste Jan, waar moet ik beginnen? Wat ik Dir zu verdanken have, fills another book. Thank you for your unendliche patience, das offene Ohr, where I could bounce of ideas, your help with all kinds of software problems, proof reading enzofoort. Danke dafür und für alles andere.

Meinen Eltern danke ich für die immerwährende Geduld und Unterstützung, die ich in allen Anliegen von ihnen erfahre. Das Vertrauen im Notfall auf Euch zurückkommen zu können, hat mir die Ruhe gegeben weiterzumachen.

List of publications

- Ph. W. Courteille, C. von Cube, B. Deh, D. Kruse, A. Ludewig, S. Slama and C. Zimmermann,
  The Collective Atomic Recoil Laser,
  AIP Conference Proceedings(ICAP2004) **770**, 135 (2005).

- S. Slama, C. von Cube, B. Deh, A. Ludewig, C. Zimmermann and Ph.W. Courteille,
  Phase-sensitive detection of Bragg Scattering at 1D Optical Lattices,
  Phys. Rev. Lett.**94**, 193901 (2005).

- S. Slama, C. von Cube, A. Ludewig, M. Kohler, C. Zimmermann and Ph.W. Courteille,
  Dimensional crossover in Bragg scattering from an optical lattice,
  Phys. Rev. A **72**, 031402(R) (2005).

- T.G. Tiecke, S.D. Gensemer, A. Ludewig and J.T.M. Walraven,
  High-flux two-dimensional magneto-optical-trap source for cold lithium atoms,
  Phys. Rev. A **80**, 013409 (2009) [Tie09b].

- T.G. Tiecke, M.R. Goosen, A. Ludewig, S.D. Gensemer, S. Kraft, S.J.M.M.F. Kokkelmans and J.T.M. Walraven,
  Broad Feshbach resonance in the ^{6}*Li-*^{40}*K mixture*,
  Phys. Rev. Lett. **104**, 053202 (2010) [Tie10b].

- A. Ludewig, L. Cook, M.R. Goosen, T.M. Hanna, T.G. Tiecke, U. Schneider, L. Tarruell, I. Bloch, T. Esslinger, P.S. Julienne, S.J.J.M.F. Kokkelmans and J.T.M. Walraven,
  Feshbach resonances in ^{40}*K*
  in preparation